

論文 / 著書情報  
Article / Book Information

題目(和文)	
Title(English)	Nanoscale spatially resolved measurements of optical-field vector using near-field light
著者(和文)	岡本拓也
Author(English)	Takuya Okamoto
出典(和文)	学位:博士(工学), 学位授与機関:東京工業大学, 報告番号:甲第11930号, 授与年月日:2021年3月26日, 学位の種別:課程博士, 審査員:河野行雄,波多野睦子,間中孝彰,渡辺正裕,岩崎孝之,田邊匡生
Citation(English)	Degree:Doctor (Engineering), Conferring organization: Tokyo Institute of Technology, Report number:甲第11930号, Conferred date:2021/3/26, Degree Type:Course doctor, Examiner:Yukio Kawano,Mutsuko Hatano,Takaaki Manaka,Masahiro Watanabe,Takayuki Iwasaki,Tadao Tanabe
学位種別(和文)	博士論文
Type(English)	Doctoral Thesis

Doctoral Thesis

# **Spatially resolved nanoscale measurements of optical-field vector using near-field light**

18D10321

Takuya Okamoto

School of Engineering,  
Department of Electrical and Electronic Engineering

Supervisor: Prof. Yukio Kawano

March 2021





# Abstract

Experimental visualization of the optical field vector on optical devices provides direct evidence for a comprehensive understanding of their properties and for guiding precise designs. In general, since the optical field vector dramatically changes at the sub-wavelength scale, characterizing it with the highest possible spatial resolution is crucial. To overcome the diffraction limit, this thesis employs scattering-type scanning near-field optical microscopy (s-SNOM) with a phase-resolved function. However, since s-SNOM obtains results by locally illuminating the near field induced at the tip to a host material, it raises questions about whether the measurement results represent the realistic optical field vector or the physical background it corresponds to. Therefore, numerical simulations are typically relied upon for comparisons, but they cannot avoid imperfections such as the absence of a tip. Hence, experimental demonstrations are essentially preferable. This study provides experimental evidence through a multifaceted approach, including electrical and material approaches.

Using s-SNOM, I demonstrate the direct visualization of the optical field vector on a logarithmic spiral antenna (LSA). By employing tunable infrared lasers and rotating the LSA, I directly understand the characteristic optical properties of an LSA through s-SNOM images. Additional near-field phase images exhibit a phase jump of  $\pi$  at the center of the LSA. Through secondary experimental evidence from electrical measurements, I find that this phase jump corresponds to the direction of the bridged optical field vector. This result indicates that the reconstruction of the optical field vector, characterized by two physical values: amplitude and direction, is feasible.

Furthermore, simulation results suggest that s-SNOM selectively probes the out-of-plane optical responses of a host material, leading us to investigate the near-field polarization of s-SNOM itself. As a platform to access near-field polarization, I employ banded polyhydroxybutyrate spherulites. Experimental results show that s-SNOM predominantly probes the out-of-plane transition moment, demonstrating that the near-field polarization of s-SNOM is mainly out-of-plane relative to the surface of a host material. This finding raises the intriguing question of whether in-plane vectorial near-field measurements are possible.

In the last chapter, I propose in-plane near-field imaging. By actively using the optical setup flexibility of the Michelson interferometer, I achieve the extraction of in-plane-polarized near fields. Additionally, to enhance near fields with s-polarization, I propose an FIB-patterned AFM tip with a tapered transmission line in this study.

I believe that the systematic and comprehensive knowledge demonstrated in this thesis paves the way for novel optical techniques, such as future nanoscale three-dimensional vectorial imaging and multifaceted applications.

# Contents

	<b>Acknowledgements</b>	<b>11</b>
<b>1</b>	<b>Introduction</b>	<b>13</b>
1.1	Optical-field vector in optical devices . . . . .	13
1.2	Characterization of optical-field vector . . . . .	15
1.2.1	Classical far-field microscopy . . . . .	15
1.2.2	Electron microscopy . . . . .	17
1.2.3	Near-field optical microscopy . . . . .	18
1.3	Purpose of this dissertation . . . . .	19
1.4	Outline of this dissertation . . . . .	20
<b>2</b>	<b>s-SNOM setup and modeling</b>	<b>23</b>
2.1	Principle of s-SNOM . . . . .	23
2.2	optical setup . . . . .	25
2.2.1	optical components . . . . .	25
2.2.2	s-SNOM setup . . . . .	26
2.2.3	Evaluations of the developed setup . . . . .	29
2.3	s-SNOM Modeling . . . . .	31
2.3.1	FEM simulation . . . . .	31
2.3.2	FEM conditions . . . . .	34
2.4	Conclusion of Chapter 2 . . . . .	41
<b>3</b>	<b>Nanoscale visualization of optical-field vector on an LSA</b>	<b>43</b>
3.1	Introduction & Concept . . . . .	43
3.2	Logarithmic spiral antenna . . . . .	44
3.2.1	Theory . . . . .	44
3.2.2	Design . . . . .	46
3.3	Method . . . . .	47
3.3.1	Fabrication . . . . .	47
3.3.2	Setup . . . . .	47
3.4	Experimental results . . . . .	50
3.4.1	NF-amplitude imaging . . . . .	50
3.4.2	NF-phase imaging . . . . .	52

3.5	Discussion . . . . .	53
3.5.1	what NF phase shows? . . . . .	53
3.5.2	Status of the NF on the tip apex . . . . .	53
3.6	Conclusion of Chapter 3 . . . . .	55
<b>4</b>	<b>Electrical approach for local optical-field vector</b>	<b>57</b>
4.1	Introduction & Concept . . . . .	57
4.2	Method . . . . .	60
4.2.1	Device fabrication . . . . .	60
4.2.2	Experimental setup . . . . .	60
4.3	Experimental results and discussion . . . . .	61
4.3.1	FIR responses of the LSA-coupled QD . . . . .	61
4.3.2	theoretical analysis . . . . .	64
4.3.3	Control experiment for the effect of LSA . . . . .	67
4.3.4	contribution of the QD on the optical response of the LSA . . . . .	69
4.4	Conclusion of Chapter 4 . . . . .	70
<b>5</b>	<b>Vectorial nature of an s-SNOM</b>	<b>73</b>
5.1	Introduction & Concept . . . . .	73
5.2	PHB spherulites . . . . .	76
5.2.1	Properties . . . . .	76
5.3	Method . . . . .	77
5.3.1	s-SNOM . . . . .	77
5.3.2	Fabrication . . . . .	77
5.4	Experimental results . . . . .	80
5.4.1	Twisted structure . . . . .	80
5.4.2	Fibrillar structure . . . . .	84
5.5	Conclusion of Chapter 5 . . . . .	86
<b>6</b>	<b>Nanoscale visualization of in-plane optical-field vector</b>	<b>87</b>
6.1	Introduction & Concept . . . . .	87
6.2	Method . . . . .	88
6.3	Experimental results and discussion . . . . .	90
6.3.1	polarization dependence of scattering coefficient . . . . .	90
6.3.2	Optical setup for in-plane NF probing . . . . .	91
6.3.3	In-plane visualization of the optical field vector . . . . .	93
6.3.4	Plasmon nanofocusing . . . . .	96
6.4	Conclusion of Chapter 6 . . . . .	99
<b>7</b>	<b>Conclusions</b>	<b>101</b>
7.1	Conclusions of this thesis . . . . .	101

7.2	Future prospects . . . . .	102
7.3	Future Prospects . . . . .	102
7.3.1	Nanoscale 3D reconstruction of optical-field vector . . . . .	103
7.3.2	Nanoscale <i>Operand</i> optoelectronic measurements . . . . .	105
	<b>Publications and Presentations</b>	<b>107</b>



# Abbreviations

<b>s-SNOM</b>	: scattering-type <b>S</b> canning <b>N</b> ear-field <b>O</b> ptical <b>M</b> icroscopy
<b>a-SNOM</b>	: aperture-type <b>S</b> canning <b>N</b> ear-field <b>O</b> ptical <b>M</b> icroscopy
<b>NF</b>	: <b>N</b> ear <b>F</b> ield(s)
<b>FF</b>	: <b>F</b> ar <b>F</b> ield
<b>IR</b>	: <b>I</b> nfra <b>R</b> ed
<b>FIR</b>	: <b>F</b> ar <b>I</b> nfra <b>R</b> ed
<b>MIR</b>	: <b>M</b> id <b>I</b> nfra <b>R</b> ed
<b>NIR</b>	: <b>N</b> ear <b>I</b> nfra <b>R</b> ed
<b>FTIR</b>	: <b>F</b> ourier <b>T</b> ransform <b>I</b> nfrared <b>S</b> pectroscopy
<b>AFM</b>	: <b>A</b> tomical <b>F</b> orce <b>M</b> icroscope
<b>FEM</b>	: <b>F</b> inite <b>E</b> lement <b>M</b> ethod
<b>PML</b>	: <b>P</b> erfectly <b>M</b> atched <b>L</b> ayer
<b>SNR</b>	: <b>S</b> ignal <b>N</b> oise <b>R</b> atio
<b>MCT</b>	: <b>M</b> ercury- <b>C</b> admium- <b>T</b> elluride
<b>QCL</b>	: <b>Q</b> uantum <b>C</b> ascade <b>L</b> aser
<b>LSA</b>	: <b>L</b> ogarithm- <b>S</b> piral <b>A</b> ntenna
<b>QD</b>	: <b>Q</b> uantum <b>D</b> ot
<b>BOX</b>	: <b>B</b> uried <b>O</b> Xide
<b>TLS</b>	: <b>T</b> wo <b>L</b> evel <b>S</b> ystem
<b>PHB</b>	: <b>P</b> oly <b>H</b> ydroxy <b>B</b> utyrate convolutional





# Acknowledgements

This thesis is a compilation of research conducted by the author during the doctoral program at Tokyo Institute of Technology.

The doctoral program is one of my most memorable and precious life experiences. I am grateful that I could join the team and pursue my doctoral program at Kawano Laboratory. I was able to conduct research in my areas of interest and improve my research skills in various aspects. Here, I would like to express my deepest appreciation to the people who were involved in my doctoral course.

I would like to express my gratitude to Prof. Yukio Kawano for giving me a wonderful opportunity to study, for engaging in stimulating discussions, and for helping me become a better scientist. His invaluable advice, guidance, and insights have motivated me to work on this research. I deeply appreciate his generous support when I needed it the most and the opportunities to collaborate with other scientists to advance my studies.

I would also like to extend my gratitude to Dr. Takamasa Kawanago for his helpful discussions that propelled my research forward. His encouragement during my time at Tokyo Institute of Technology was instrumental.

Special thanks go to Prof. Mutsuko Hatano, Prof. Takaaki Manaka, Prof. Masahiro Watanabe, Prof. Takayuki Iwasaki, and Prof. Tanabe (Department of Engineering and Design, Shibaura Institute of Technology) for examining this thesis.

I extend my gratitude to Prof. Junko Morikawa and Dr. Meguya Ryu for providing the polyhydroxybutyrate spherulites, which were instrumental in investigating the vectorial nature of the near fields in s-SNOM. I would also like to thank Prof. Tetsuo Koderu for his constructive comments and insights regarding the photo responses of Si quantum dots.

I express my gratitude to secretaries, Mrs. Kaori Hashimoto and Mrs. Yukiko Hayashi, for their assistance with administrative affairs during my studies.

I am thankful to all the current and former students in (Oda-)Kawano Laboratory for their valuable assistance and productive discussions.

Finally, I would like to express my appreciation to my family for their unwavering love, unconditional support, and financial assistance throughout my doctoral program.



# Chapter 1

## Introduction

**This chapter presents an introduction to characterization techniques for investigating the optical-field vector in optical devices. The purposes of this study are also introduced.**

### 1.1 Optical-field vector in optical devices

The vectorial nature of light provides a third degree of freedom, besides frequency and linear momentum, for accessing the rich physical properties of materials. The phenomena of radiation and scattering of light field vectors can be designed by artificial structural engineering because of the interrelationship between the structure of the material and the optical properties. This concept has long been used in conventional classical antennas[1, 2]. In recent years, the development of microfabrication technology has made it possible to design artificial structures on the wavelength scale of light, and materials with unique optical properties, i.e., metamaterials [3, 4], that do not exist in nature have been realized [5, 6]. Specifically, by controlling the dispersion relation of light as well as electrons described by Bloch states in crystals, control/localization of group velocity and band gap of light have been realized [7]. Since these structure-derived phenomena are mathematically derived from the properties of waves, they can essentially be understood and predicted by analogy with other waves including electrons and photons. For example, topological photonics, which characterizes optical properties by the mathematical concept of topological numbers, originally originated in physics with the quantum Hall effect [8, 9] in electronic systems. Very recently, a method to generate and control optical topological insulators by electric current has been proposed[10], and many functionalities have been realized by combining them with other material waves. Among such structurally designed materials, those with strong structural anisotropy are of great interest. Examples are the giant birefringence in two-dimensional and polymeric materials [11] and the universal localization

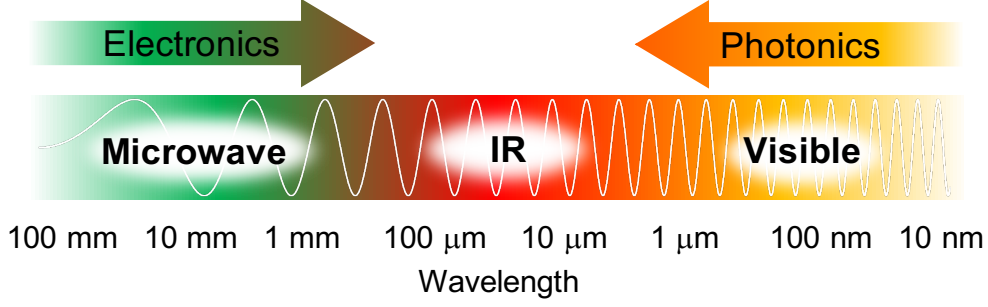


**Figure 1.1:** Electromagnetic spectrum.

of light, i.e. Anderson localization [12–14] in fibrillar systems[15] and random lasing[14].

Infrared light (IR) is an electromagnetic field region where they are strongly expected to be applied in diverse regions (Fig. 1.1) [16–19]. This is because the operating frequency of these optical elements can be easily controlled by their structures. Especially in the mid-to far-infrared light (MIR and FIR, respectively), they correspond to many important energy spectra of matter, such as vibrations and rotations of all molecules [16], lattice vibrations of solids, impurity levels[20, 21], energy gaps in superconductors[22], quantized levels of electrons in semiconductor microstructures[18, 23, 24], and Landau levels in strong magnetic fields [25, 26]. Therefore, it has been of particular importance in many fundamental physics such as solid-state physics, molecular spectroscopy, and IR/radio astronomy. However, contrary to the importance of such IR light technology, the basic elemental technology is still very unexplored compared to other electromagnetic fields. The reason for this is that the knowledge of both electronics and photonics, which have matured so far, cannot be easily applied; In the former, the electromagnetic field is characterized by frequency, which is in principle too fast for the operating frequency speed of electronic devices. In the latter, the electromagnetic field is characterized by photon energy, and its photon energy is much lower than the bandgap energy of common materials, making it difficult to handle IR waves with conventional semiconductor technology. These problems continue to be challenged by approaches that surpass these limits, including ultrafast electronics[27], quantum electronics[18, 23], and nanocarbon materials[25, 28]. Another solution is optically designed devices with the structures described above[29, 30]. These devices have the strong advantage that they are not subject to conventional constraints because their optical properties are scalable and controllable by the structure; which is promising to open a pathway to further developments of optical components in the IR region.

In addition to the wide range of optical frequencies provided by optical devices, optical confinement offers another significant advantage, enabling sub-diffraction-limited optical research and techniques that can effectively concentrate light. This capability is achieved

through the use of artificially manufactured micro-/nano-structures, such as metamaterials or plasmonic structures [30], which provide a valuable platform across various fields, including biosensing [31, 32], spectroscopy, and nanoscale optical probing techniques [33, 34].

Nano-optical devices play a pivotal role as the cornerstone of nano-optics development, underscoring the importance of accurately understanding their characteristics. In particular, experimental visualization of the distribution of the optical field vector serves as direct evidence for elucidating the properties of optical devices. Therefore, achieving the radiation/scattering phenomenon of an optical field vector with the highest possible spatial resolution is a critical objective. In the next section, I will introduce several types of characterizations for the optical field vector in optical devices.

## 1.2 Characterization of optical-field vector

### 1.2.1 Classical far-field microscopy

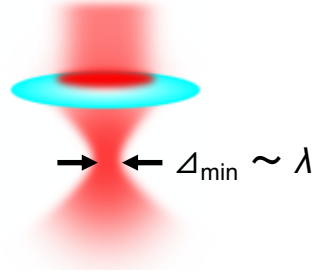
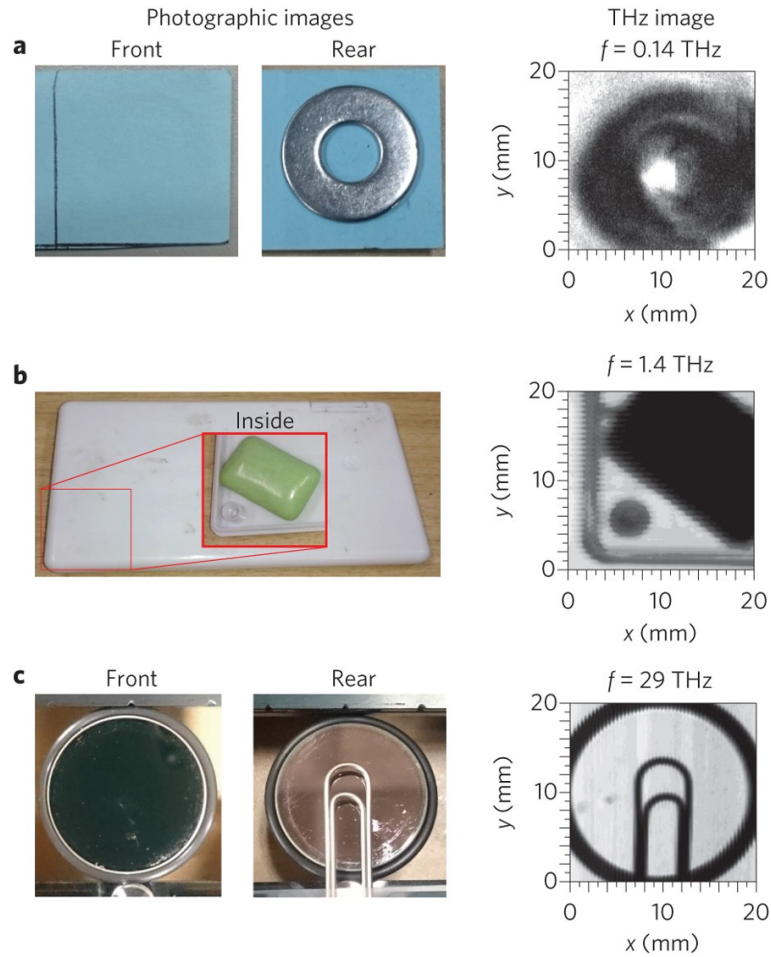
In a classical light microscope, an electromagnetic field is usually propagated to form an image of the object to be observed. An image uses a diffraction phenomenon to magnify or reduce an object with a lens, but there is a limit to how far it can be magnified with a conventional microscope that uses a distant field, i.e. spatial resolution, as shown in Fig. 1.2. However, a fatal drawback is the limitation of spatial resolution due to the diffraction phenomenon of the electromagnetic field. Spatial resolution is generally defined as the minimum distance  $\Delta_{\min}$  between two distinguishable points. E. Abbe and L. Rayleigh have formalized the value of  $\Delta_{\min}$  as [35],

$$\Delta_{\min} = \frac{0.61\lambda}{NA} = 1.22F\lambda \quad . \quad (1.1)$$

Here,  $\lambda$  is the wavelength of the electromagnetic field used for imaging,  $NA$  is the numerical aperture, and  $F$  is the F-number of the lens used for imaging. The largest value of  $NA = n \sin 2\theta_{\max}$  is  $\sim 1$ , leading  $\max\{\Delta\} \sim 2/\lambda$  (the diffraction limit), where  $n$  is the refractive index of the medium surrounding the imaged object and  $2\theta_{\max}$  is the maximum collection angle of the microscopy. The diffraction limit is the resolving power of an ideal lens that has no aberration in the optical system, or when the aberration is so small that it can be ignored with respect to the evaluation wavelength. Therefore, the  $\Delta_{\min}$  is typically deal as  $\Delta_{\min} \sim \lambda$ . This fact means that visible light does not provide spatial resolution below hundreds of nanometers. IR has a long wavelength, thus the spatial resolution becomes larger than several tens of micrometers (Fig. 1.3). This spatial resolution is insufficient for the visualization of optical vector fields on optical devices.

To gain the spatial resolution beyond the diffraction limit, there are mainly two ap-

The diffraction limit

**Figure 1.2:** Schematic diagram of the diffraction limit.**Figure 1.3:** Comparison of the spatial resolution using three wavelengths in the FIR region. The left pictures are visible light images, and the right ones are FIR images. Reprinted figures with permission from Ref. [28]. Copyright 2016 by Springer Nature.

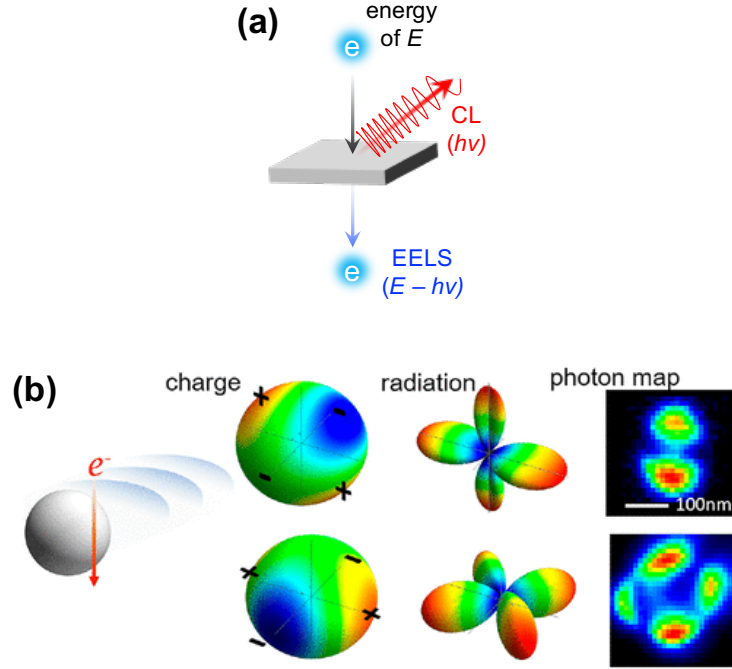


**Figure 1.4:** (a) schematic illustration of EELS and CL. (b) optical-field maps of an Ag nanoparticle. Reprinted figures with permission from Ref. [36]. Copyright 2018 American Chemical Society.

proaches; one is shorting wavelength as possible. Another is using not the FF field but NFs.

### 1.2.2 Electron microscopy

The spatial resolution of electron microscopy-based methods is determined by the de Broglie wavelength of the electrons, resulting in an exceptionally high spatial resolution, surpassing several tens of picometers.

These methods can be mainly categorized into two distinct spectroscopy techniques: Electron Energy Loss Spectroscopy (EELS) and Cathodoluminescence (CL). Schematic illustrations of their mechanisms are presented in Fig. 1.4(a). EELS involves scattering and absorption phenomena, displaying excitation and extinction phenomena when electrons are irradiated. Consequently, visualizing the optical-field vector using EELS is challenging.

On the other hand, CL encompasses scattering and radiation measurements during electron-beam irradiation. The advantage of visualizing the light vector field with CL is that, unlike EELS, it allows for angle-resolved and polarization-resolved measurements because it directly measures light. This feature enables selective visualization of degenerate modes, as demonstrated in Fig. 1.4(b) [36–38].



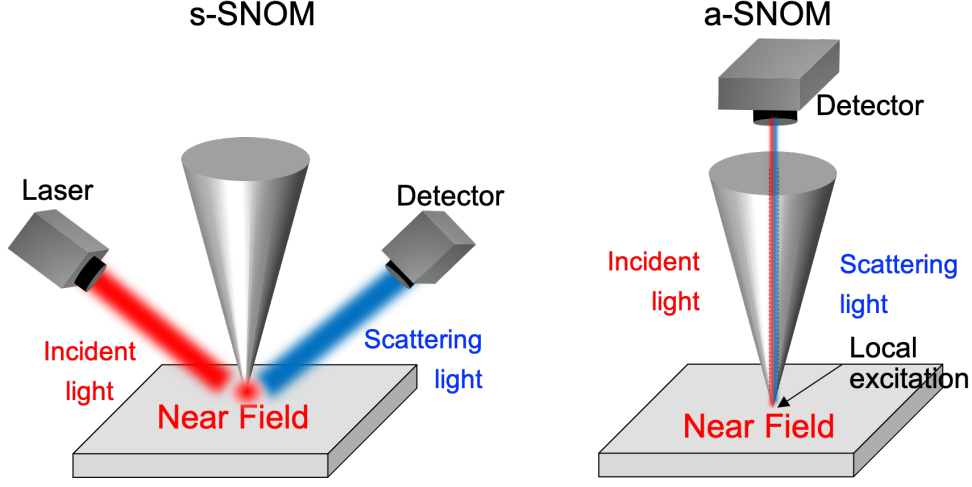


**Figure 1.5:** Illustration of an s-SNOM (left) and a-SNOM (right.)

### 1.2.3 Near-field optical microscopy

Although SEM-based microscopy is a nanoscale visualization technique using extremely short wavelengths of de Broglie waves, imaging by elastic scattering of light, rather than inelastic scattering via electrons, is preferable for observing the direct optical-field vector at the operating condition. Near-field (NF) microscopy is an optical microscope utilizing NFs. optically excited by electromagnetic fields on the nanostructures such as sharp tips. These NF microscopies can be mainly categorized into two different types as below.

#### a-SNOM

An aperture-type SNOM (a-SNOM) employs the NF radiated from a small aperture on a cantilever[39, 40]. The NF light interacts with the sample, and the NF image is obtained from the scattered light that passes through the cantilever.

#### s-SNOM

A scattering-type scanning optical microscope (s-SNOM) is an atomic-force-microscopy (AFM)-based technique that provides optical responses with a resolution similar to the size of an AFM-tip apex [41–43]. The mechanism involves the optical excitation of NFs by external electromagnetic waves. (An a-SNOM is a transmission-based NF microscopy.) The physical background of s-SNOM is characterized by localized surface plasmon polari-

	a-SNOM	s-SNOM
spatial resolution	$\sim 100$ nm	$\sim 10$ nm
signal	higher	lower
background	lower	higher <sup>1</sup>
excitation of host materials	local	entire

**Table 1.1:** Comparison of an a-SNOM and an s-SNOM.

tons on an AFM-tip apex, which is why it's sometimes referred to as "plasmonic-based SNOM."

One of the advantages of s-SNOM for visualizing the optical-field vector in optical devices is that the devices probed by s-SNOM are simultaneously optically excited by an external field. This differs from a-SNOM, which only radiates a local spot on the optical devices (Fig. 1.5). Another advantage of s-SNOM over a-SNOM is its higher spatial resolution. Generally, the spatial resolution of s-SNOM is known to depend solely on the radius of the AFM-tip apex[44]. This is an advantage over a-SNOM, which is limited by the process of creating apertures with sizes larger than several tens of nanometers.

Although not strictly s-SNOM, very recent reports [45] of tip-enhanced Raman spectroscopy have achieved atomic-scale imaging. This outcome suggests the exciting possibility that s-SNOM could enable optical access to phenomena with atomic-scale resolution, potentially opening the door to "atom photonics" in the future.

The comparison of properties of the two-type SNOMs is summarized in Table 1.1.

### 1.3 Purpose of this dissertation

#### Main purpose

- Nanoscale visualization of optical-field vector using an s-SNOM
- Proposing novel optical probing techniques

#### Problems

- Few experimental comparisons with s-SNOM results
- Poor understanding of s-SNOM properties (only calculation)

Using an s-SNOM, several studies have reported the distribution of the optical field vector on optical devices. However, as described earlier, the optical field vector is typically characterized by two physical variables: intensity and direction. Therefore, it is essential to obtain both of these observable factors.

Recent advancements in the design of optical setups for s-SNOM [46] have allowed not only amplitude but also phase information of the NF localized on the sample surface to be

acquired, offering the potential for restoring the complete optical field vector. However, the information presented in NF images has not been fully understood, even in theoretical descriptions [47]. This challenge arises from two main factors: a limited understanding of the NF properties in s-SNOM and the lack of secondary experimental evidence for validating NF phase information.

The first issue is rooted in the absence of suitable optical probing tools for accessing the optical field vector due to the diffraction limit. Therefore, numerical simulations have become the primary means of making comparisons, despite inherent imperfections such as the absence of the tip in simulations. In this study, our goal is to shed light on the physical significance of NF images through alternative approaches, particularly electrical measurements under radiation.

Regarding the second issue, s-SNOM is a relatively recent measurement technique compared to other optical microscopies. Consequently, a comprehensive understanding of s-SNOM properties will be achieved through a combination of simulations and experiments. Since direct experimental access to NF is challenging, I intend to gather experimental evidence through tip-sample optical interactions. Subsequently, I aim to construct quantitative theoretical models to explain the NF properties. In particular, a rigorous understanding of the vectorial nature of s-SNOM is crucial because the vectorial NF is coupled to the vector components of the host material.

Furthermore, based on the knowledge obtained, I will propose and demonstrate unique optical measurements that are specific to s-SNOM.

Strategies —

- Experimental demonstrations through multifaceted experiments

## 1.4 Outline of this dissertation

Figure 1.18 shows the contents of this thesis. This thesis consists of 7 parts.

### Chapter. 1

Background of optical characterization for nano-optical devices and the purpose of this study were introduced.

### Chapter. 2

The phase-resolved s-SNOM is presented. To evaluate the properties of this s-SNOM, I developed the theoretical s-SNOM model.

### Chapter. 3

Experimental demonstrations of NF imaging of the optical field vector are presented using a logarithmic spiral antenna.

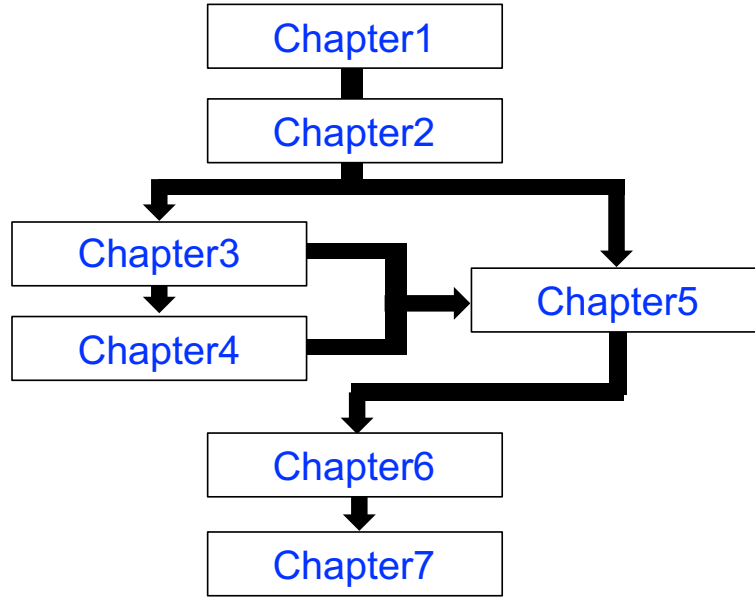


**Figure 1.6:** Outline of this dissertation.

#### **Chapter. 4**

To obtain secondary data for discussing the NF phase gained in the chapter 3, the local optical-field vector on the LSA has been investigated through electrical probing techniques.

#### **Chapter. 5**

For clarifying the physical meaning of the NF phase, the NF polarization, i.e. vectorial nature, of an s-SNOM itself is experimentally investigated through vibrational spectroscopic imaging. By using a polymer spherulite as a host material, I have clarified that the NF polarization of an s-SNOM is mainly polarized to out-of-plane.

#### **Chapter. 6**

For arbitrary vectorial probing, the s-SNOM in-plane visualization of the optical-field vector is discussed.

#### **Chapter. 7**

Conclusion of this dissertation. Future prospects of this study are also described.



## Chapter 2

# s-SNOM setup and modeling

In this chapter, I present the phase-resolved s-SNOM setup. Introducing a Michelson interferometer allows not only the acquisition of the NF phase but also the efficient extraction of pure NFs. To evaluate this setup, I have theoretically developed a quasi-static model of NFs, which includes the dynamics of an AFM tip. This developed model reconstructs experimental data on the distance dependence of the tip-sample optical interaction for s-SNOM measurements.

### 2.1 Principle of s-SNOM

For s-SNOM measurements, a metal-coated AFM tip is typically used. When irradiating the apex of an AFM tip, a strong electromagnetic field is excited at nanoscale spots, creating localized fields known as NFs, distinct from evanescent fields. These NFs on a tip can be modeled using point dipole models [48–51] and finite dipole modes [51, 52]. In our study, I precisely investigated NF behavior by numerically solving Maxwell’s equations.

Fig. 2.1 illustrates a simulation (described later) of a metal-coated AFM tip irradiated with MIR light ( $\nu = 1075 \text{ cm}^{-1}$ ). The color scale represents the ratio of the local electric field to the incident electric field  $|E|/|E_{\text{inc}}|$ , indicating electric field enhancement. It can be observed that the electric field is strongly confined to the apex of the AFM tip and is spatially confined to a much smaller scale than the illumination wavelength, exhibiting spatially exponential decay. These NFs provide access to the optical properties at the nanoscale, surpassing the diffraction limit.

Specifically, when the NFs on the AFM tip are closer to the surface of host materials than the spatial attenuation of the NF hotspot, the NFs interact with the host material’s surface. While the NF interaction is not fully understood due to mathematical complexities [53], this interaction generates scattering far-field (FF) light. For instance, metallic host

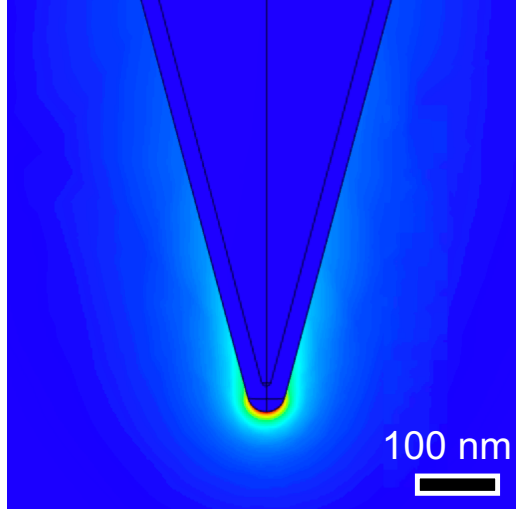


**Figure 2.1:** Numerically calculated distribution of electric field.

materials induce quadrupole effects due to mirror dipoles, resulting in modifications of the FF components. By detecting this FF scattered light, a nanoscale-resolved optical image of the sample surface can be obtained.

Considering this process, the optical properties of the host material, i.e., NF interactions, can be described by the complex scattering coefficient  $\eta_n = s_n \exp(\varphi_n)$  [47], where

$$E_{\text{sca}} = \eta_n E_{\text{inc}} \quad (2.1)$$

and  $E_{\text{sca}}$  is the scattered electric field, while  $n$  represents the order of modulation harmonic/order of demodulation (explained later).

Generally,  $E_{\text{NF}}$  associated with the NF interaction between the tip and the sample surface includes not only the pure NF signal but also background scattered light, such as light reflected from the surface of a host material or from an AFM tip. This background can be explained by the focal spot size of irradiation. As described in (1.1), the minimum spot size of light is limited to approximately its wavelength. Therefore, irradiating light solely onto an AFM-tip apex is, in principle, impossible. Consequently,  $E_{\text{sca}}$  essentially contains background electric field  $E_{\text{bak}}$ , which is given by

$$E_{\text{sca}} = E_{\text{NF}} + E_{\text{bak}} \quad . \quad (2.2)$$

This unavoidable  $E_{\text{bak}}$  leads to an effective decrease in SNR, necessitating the use of various approaches such as tapping AFM, indirect irradiation[54], and plasmon nano-focusing[55]. Among these methods, tapping AFM [41] is employed in our study.

As mentioned above, the s-SNOM used in this study employs tapping mode, thus  $E_{\text{sca}}$  is modulated by the tapping frequency  $\Omega$ . Thus,  $E_{\text{sca}}$  is written as time-dependent function;

$$E_{\text{sca}}(t) = E_{\text{NF}}(t) + E_{\text{bak}}(t) \quad (2.3)$$

$$= \sum_{n=0}^{\infty} \tilde{E}_{\text{NF}}^{(n)} \cos(n\Omega t) + \sum_{n=0}^{\infty} \tilde{E}_{\text{bak}}^{(n)} \cos(n\Omega t) \quad (2.4)$$

, where  $\tilde{E}_{\text{NF,bak}}^{(n)} = \eta_{\text{NF,bak}}^{(n)} E_{\text{in}}$  represent the  $n$ th-order complex-valued Fourier coefficient of  $E_{\text{NF,bak}}$ .

The MCT detector used in this study detects the scattered light as intensity described;

$$I_{\text{sca}} = |E_{\text{sca}}|^2 \quad (2.5)$$

$$= |E_{\text{NF}} + E_{\text{bak}}|^2 \quad (2.6)$$

Thus, the gaining  $\arg(\eta_{\text{NF}}^{(n)}) = \varphi_{\text{NF}}^{(n)}$  needs  $\arg(\eta_{\text{bak}}^{(n)}) = \varphi_{\text{bak}}^{(n)}$ , whereas the precise probing of  $\varphi_{\text{bak}}^{(n)}$  is very difficult because the backscatters occur with very many factors. For obtaining the NF phase  $\varphi_n$ , an alternative method of introducing reference light has been employed (described later).

## 2.2 optical setup

### 2.2.1 optical components

The typical optical components used in this study are summarized below:

#### **AFM operation ; tapping mode**

The s-SNOM was operated in the tapping mode with an amplitude of approximately 70 nm at a mechanical resonance frequency of  $\Omega_{\text{tip}} \approx 270$  kHz for the AFM tip.

#### **AFM tip a Pr/Ir-coated tip**

Unless otherwise noted, the AFM tip is a Pr/Ir-coated tip (ARROW-NCpt, Nanosensors) with a radius of approximately 20 nm. The SEM image is displayed in Fig. 2.2.

#### **detector MCT detector**

Such demodulated scattered IR light was detected by the photoconductive HgCdTe detector cooled at nitrogen-liquid temperature ( $\sim 77$  K).

#### **CO<sub>2</sub> gas laser**

To capture monochromatic images at various wavenumbers, I employed a discretely



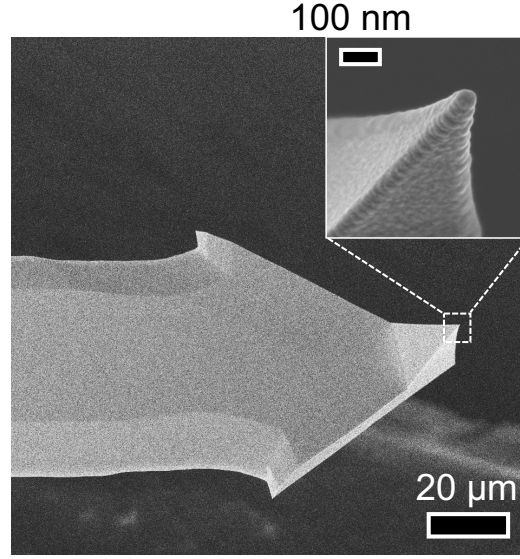


**Figure 2.2:** SEM image of a Pr/Ir-coated AFM tip typically used in this thesis.

tunable CO<sub>2</sub> gas laser (L4-GS-FCCL, Access Laser Co.,) that could be tuned between 930 cm<sup>-1</sup> and 1050 cm<sup>-1</sup>. The operable wavelength range is described in Table 2.1.

To enhance the quality of s-SNOM images, an active-feedback cooling system was installed. Additionally, to minimize vibrations, this cooling system uses water instead of air, resulting in a stable temperature change of less than 0.1 degrees Celsius. This stability contributes to maintaining laser power within a variation of less than 0.74%, leading to an improvement in the signal-to-noise ratio (SNR) of the raster scan.

### quantum cascade laser (QCL)

This QCL (customed, Hamamatsu Photonics K.K.) was water-cooled and operated at a wavenumber of 1294 cm<sup>-1</sup>.

### He-Ne laser

This laser is visible light and is used as a guide light. The wavelength is 633 nm.

Unless otherwise noted, the experimental conditions described in the other chapters are consistent with those specified here. All s-SNOM measurements conducted in this thesis were carried out at approximately 295 K in ambient atmospheric conditions.

### 2.2.2 s-SNOM setup

To introduce a reference light, a Michelson interferometer was incorporated into the optical setup. The schematic illustration of this optical configuration is depicted in Fig. 2.3.

Wavelength ( $\mu\text{m}$ )	Power (mW)	Wavelength ( $\mu\text{m}$ )	Power (mW)
10.764	160	10.260	500
10.741	130	10.247	430
10.719	240	10.233	430
10.696	310	10.220	440
10.675	400	10.207	310
10.653	490	10.195	350
10.632	480	10.182	240
10.611	390	10.170	170
10.591	540	9.657	110
10.571	490	9.639	130
10.551	430	9.621	190
10.532	530	9.604	140
10.513	430	9.588	290
10.494	410	9.569	190
10.476	350	9.552	330
10.458	180	9.536	330
10.349	90	9.520	330
10.334	350	9.504	350
10.318	320	9.488	250
10.303	440	9.473	310
10.289	480	9.458	160
10.274	450		

**Table 2.1:** Wavelength and power of the tunable CO<sub>2</sub> gas laser.

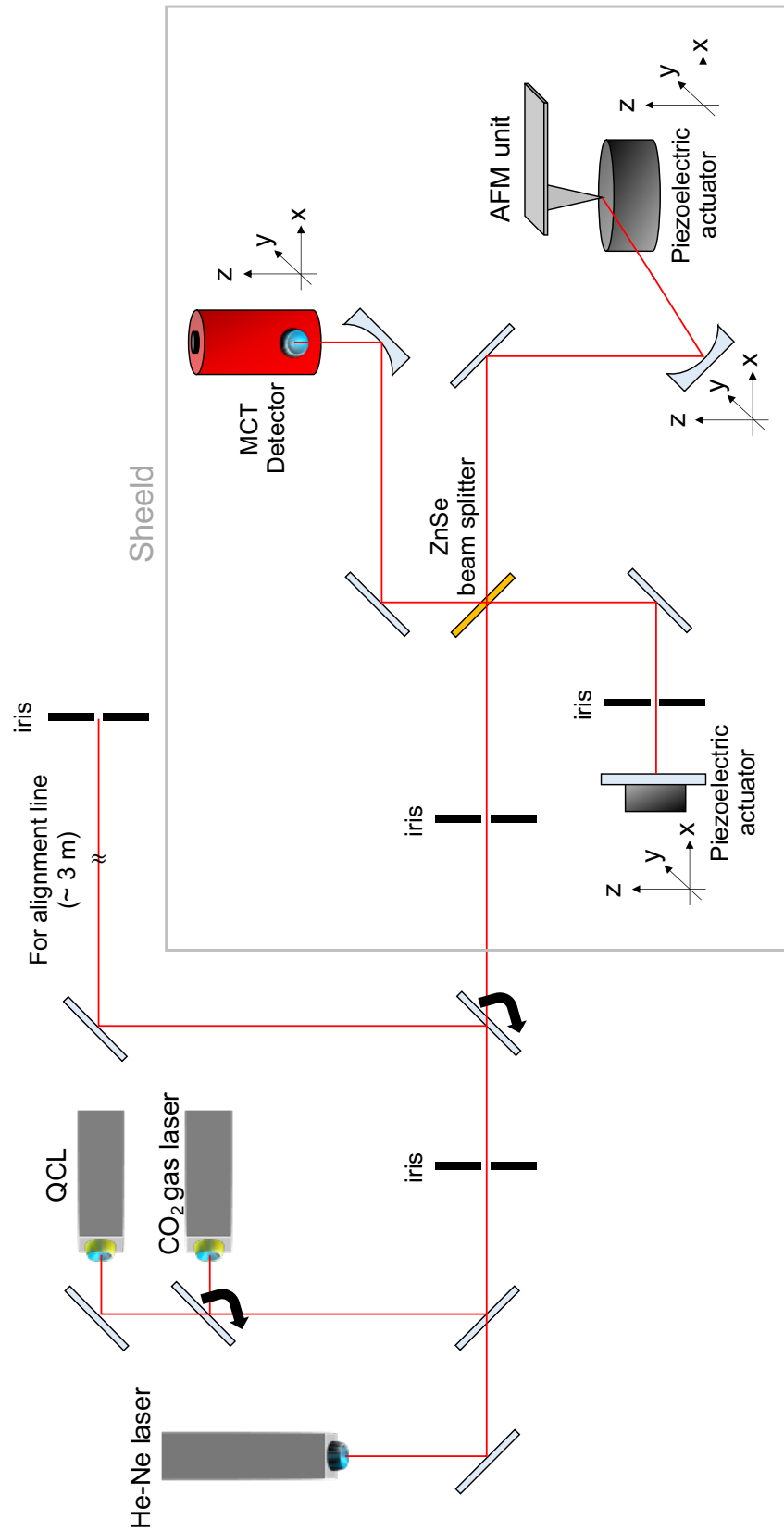


**Figure 2.3:** Optical setup of the s-SNOM.

The optical setup is schematically illustrated in Fig. 2.3. The procedure for aligning the laser beam emitted from the IR laser is carefully carried out using an alignment line for each experiment. This alignment line is accurately defined using a visible light laser emitted from a He-Ne laser.

To introduce a reference light, a ZnSe beam splitter Michelson interferometer has been integrated into the optical path. This Michelson interferometer divides the optical path into two: one for illumination and the other for the reference arm. The transmitted illumination is effectively focused both on the AFM tip and the surface of the sample by a  $45^\circ$  parabolic mirror. The scattered light, which carries information about the NFs, is focused using the same  $45^\circ$  parabolic mirror and then transformed into parallel light.

The ZnSe beam splitter combines this scattered light with the reference light, which is reflected by the reference mirror. The resulting interfered light is once again focused, this time by a  $45^\circ$  parabolic mirror, and is subsequently detected by an MCT detector.

To suppress the noise, I have made several improvements. The AFM-unit part is surrounded by a steel plate to suppress acoustic noise and external radiation such as black-body radiation. The cooling system of the CO<sub>2</sub> gas laser employs an active-feedback cooling system. The medium for cooling lasers is water (not air). The power supplies of the AFM unit and lasers are separated.

The intensity  $I_{\text{sca}}$  detected by this optical setup is expressed as;

$$I_{\text{sca}} = |E_{\text{sca}} + E_{\text{ref}}|^2 \quad (2.7)$$

$$= |E_{\text{NF}} + E_{\text{bak}} + E_{\text{ref}}|^2 \quad (2.8)$$

To gain the relative phase to the reference light, the reference mirror is vibrated at a frequency  $\sim 295$  Hz. Through the double lock-in signal, the double responsible factor in (2.8) can be extracted as;

$$I_{\text{sca}} \sim 2|E_{\text{NF}}||E_{\text{ref}}|\cos(\Delta\varphi) \quad (2.9)$$

, where  $\Delta\varphi = \varphi_{\text{NF}} - \varphi_{\text{ref}}$ . Through these signal modifications, the NF phase can be obtained.”

### 2.2.3 Evaluations of the developed setup

As a demonstration, I captured images of Si and SiO<sub>2</sub> with and without reference light using the QCL. Fig. 2.4 represents the phase images. The NF phase contrast can be seen by introducing the reference light.

From equation (2.9), i can anticipate an increase not only in NF phase but also in NF amplitude  $s_n$  when  $E_{\text{NF}}$  is multiplied by  $E_{\text{ref}}$ . Therefore, I also compared  $s_n$  with and

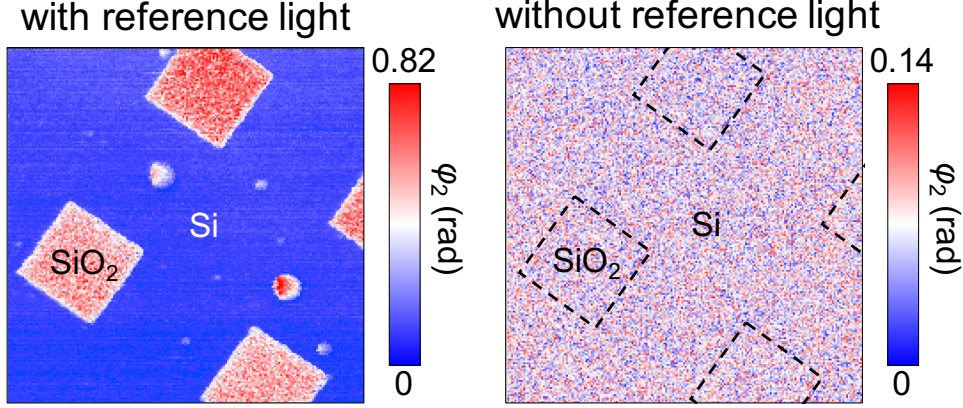


**Figure 2.4:** NF phase image of SiO<sub>2</sub> and Si.

	Topography (nm)	NF signal ( $\mu$ V)
unimproved (former)	3.99	4.47
improved (this work)	0.169	0.185

**Table 2.2:** Noise value of the topographic and NF signal

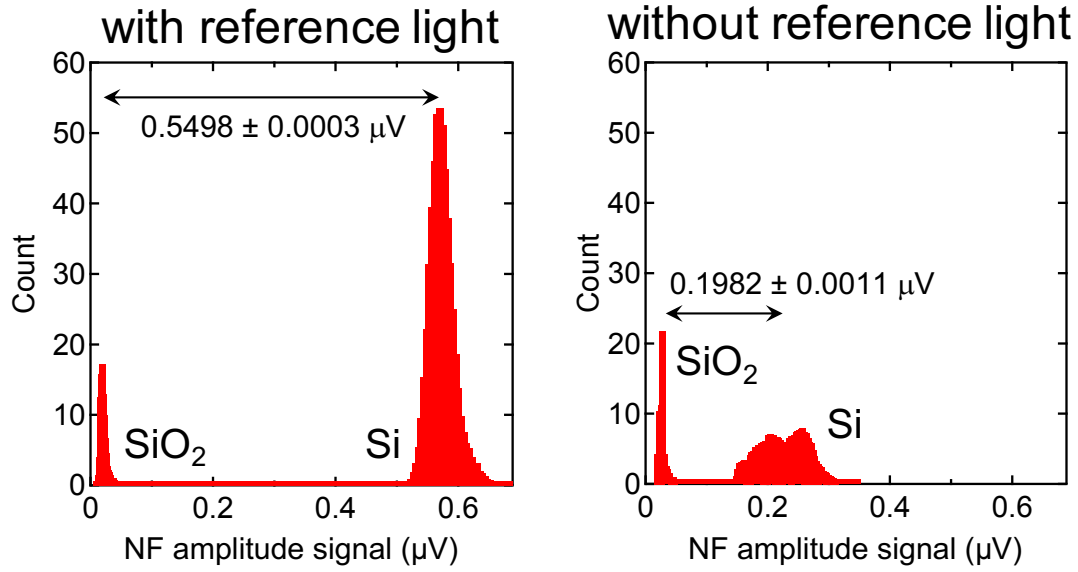
without reference light.

Fig. 2.5 displays the histogram of  $s_3$ . It is evident that introducing reference light enhances the contrast of  $s_3$ . Moreover, the shape of the histogram is Gaussian when using reference light, while it is distorted without reference light. This trend suggests that the introduction of reference light increases statistical reliability, which is a crucial factor in ultrasensitive measurements such as s-SNOM.

As described above, several improvements have been made to suppress noise. A comparison of the noise values obtained with the unimproved and improved s-SNOM system is summarized in Table 2.2. Both topographic and NF signals are significantly reduced, approximately by a factor of 1/24. The most notable improvement is in topographic noise, which is now on the order of angstroms. This reduced noise level enables NF investigations not only of optical field vectors but also of ultra-thin films such as graphene and transition metal dichalcogenides, which are currently hot topics in research.

Finally, one of the most important factors in s-SNOM, spatial resolution, has been investigated. To assess the NFs, the monitoring of changes in NF signals with tip-sample distance is often used, referred to as an "approach curve."

The approach curves with and without reference light are shown in Fig. 2.6. It can be roughly observed that the decay is more pronounced with the reference light. While the exact interpretation of the approach curve has not been proposed yet, I evaluated the decay factor at the tip-sample distance where the NF signal is  $1/e$ . This approach yields



**Figure 2.5:** Histogram of  $s_3$  for SiO<sub>2</sub> and Si.

decay factors of  $18.31 \pm 0.24$  nm with reference light and  $35.20 \pm 0.35$  nm without reference light. Therefore, the introduction of reference light also improves spatial resolution.

This difference can be understood through equations (2.6) and (2.9). The detected signal without reference light contains the contribution of the background  $E_{\text{bak}}$ , which reduces spatial resolution. With the reference light, the resulting spatial resolution of the developed s-SNOM is in the range of several tens of nanometers. However, it is unclear whether this value is superior or not. To further evaluate it, I will develop a theoretical s-SNOM model and then discuss spatial resolution. Furthermore, I will aim to gather other useful information to improve s-SNOM measurements.

## 2.3 s-SNOM Modeling

To model s-SNOM, the Finite Element Method (FEM) was primarily employed as a numerical tool (COMSOL Multiphysics, COMSOL Inc., U.S.).

### 2.3.1 FEM simulation

**FEM principles** The FEM was initially developed by Clough et al. [56] and has since been applied in various fields, including mathematical problem-solving, electronic state calculations, flow analysis, and electromagnetic field analysis.

One of the features of FEM is the division of objects into elements of finite size for solving field problems, such as the wave equation. Even objects with complex shapes are divided into elements with simple shapes such as squares and triangles, as shown in the

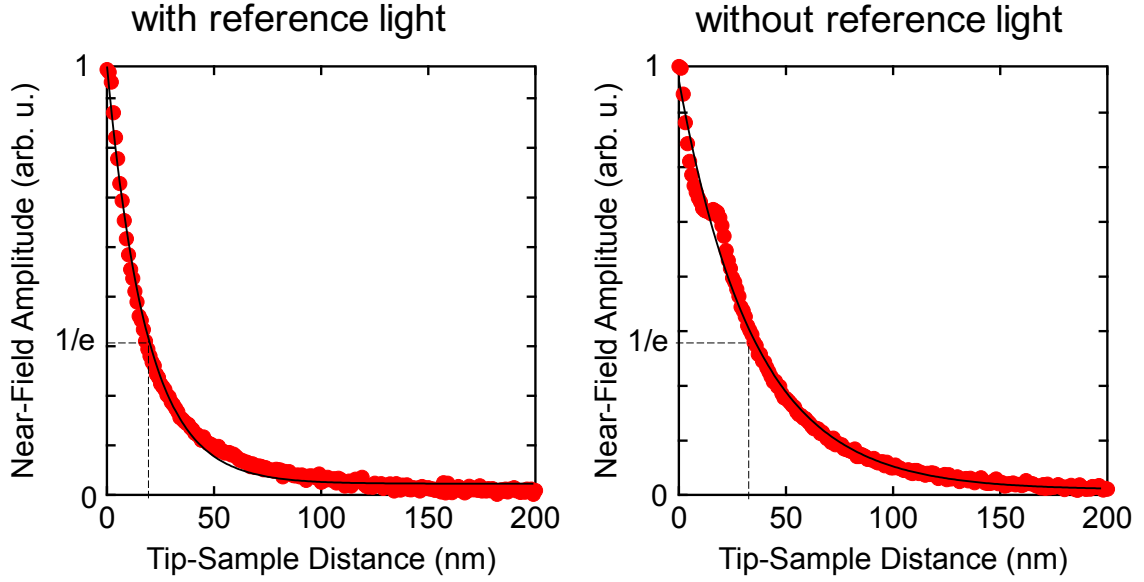


**Figure 2.6:** Approach curves with and without reference light.

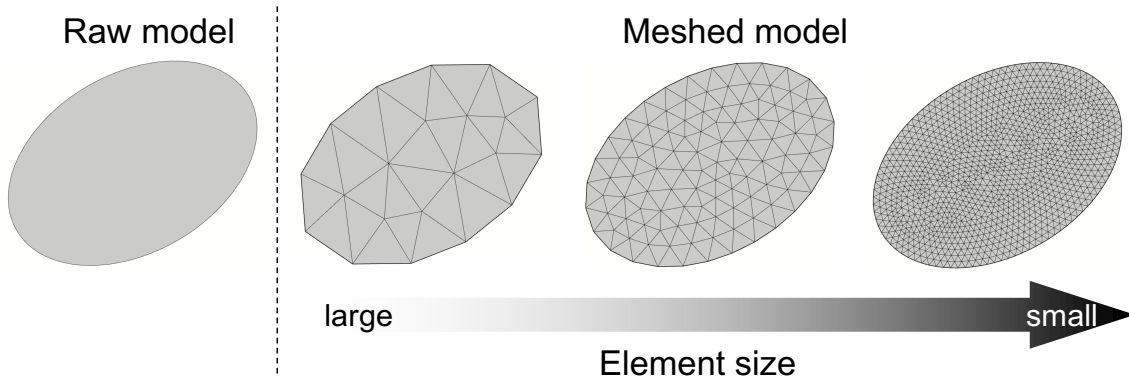


**Figure 2.7:** Comparison of the raw model and the discretized model meshed with three different element sizes.

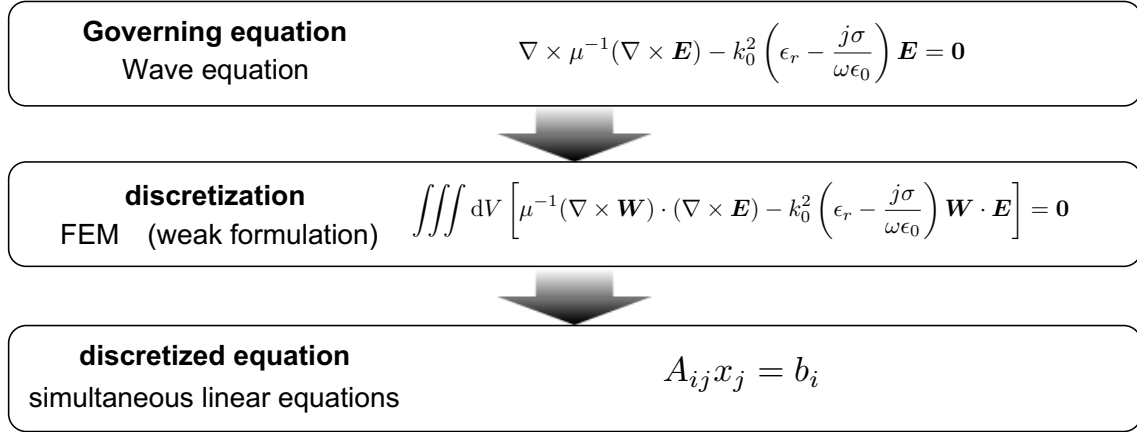


**Figure 2.8:** The process of discretizing the wavefunction.

Fig. 2.10. The object to be analyzed is considered a collection of these simple elements, and equations are formulated for each element. These equations are then combined into a simultaneous linear equation for the entire object and solved to predict the behavior of the object as a whole. The sub-domain generated by the decomposition of the object is referred to as a mesh, and the grid points within the mesh are called nodes.

When performing a calculation, a finer mesh can be generated for high-precision analysis. However, increasing the number of meshes also increases the number of calculations and, consequently, the computation time.

Another characteristic of FEM is the indirect solution of differential equations by converting them into weak formulations (integral forms). The weak form is derived from the wave equation using methods like the weighted residual method, as depicted in Fig. 2.8. Since this weak form represents a linear equation for the electric field vector  $\mathbf{E}$ , it can be transformed into a matrix equation for computation.

For a mathematical model to be analyzed, the process of applying discretization to obtain an approximate solution consists of three parts.

### Preprocess

This phase involves configuring the calculation conditions before numerical computation. Tasks in this phase include modeling target objects, specifying mesh conditions, defining the optical constants of materials, and establishing boundary conditions.

### Main Process

During this phase, an approximate solution is obtained through numerical computation using the discretization method, based on the conditions set in the preprocessing stage.

### Postprocess

In this phase, the results obtained in the main process are organized and displayed.



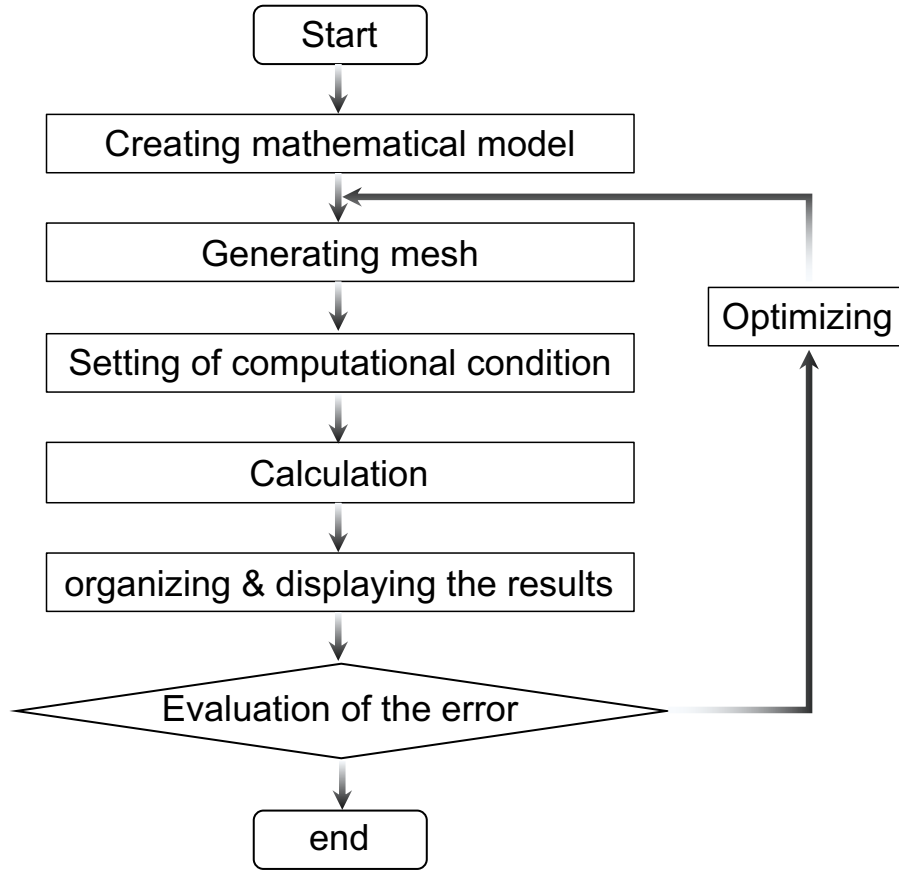


**Figure 2.9:** Calculation flow of the FEM simulation.

OS	Windows 7 Professional
CPU	Intel(R) Xeon(R) E5-2667 v3 @3.20GHz (2 processors)
RAM	128 GB

**Table 2.3:** The hardware condition for the FEM calculation.

Additionally, the error in the obtained results is evaluated, and if necessary, further calculations are performed iteratively.

### 2.3.2 FEM conditions

The hardware condition is described in Table 2.3.

To minimize RAM usage, two-dimensional simulations have been employed in this chapter<sup>1</sup>. The simulation volume size was set to model air ( $\epsilon_{\text{air}} = 1$ ) with dimensions of  $50 \times 50 \mu\text{m}^2$ . The AFM tip was modeled as a  $15 \mu\text{m}$ -long Si needle ( $\epsilon_{\text{Si}} = 11.7$ ) coated with  $\sim 20 \text{ nm}$  of Pr ( $\epsilon_{\text{Pr}} = 9.2 \times 10^9$ ), designed to have a similar geometry as the AFM tip

<sup>1</sup>Three-dimensional simulations will be performed in Chapter 5 to discuss three-dimensional polarization

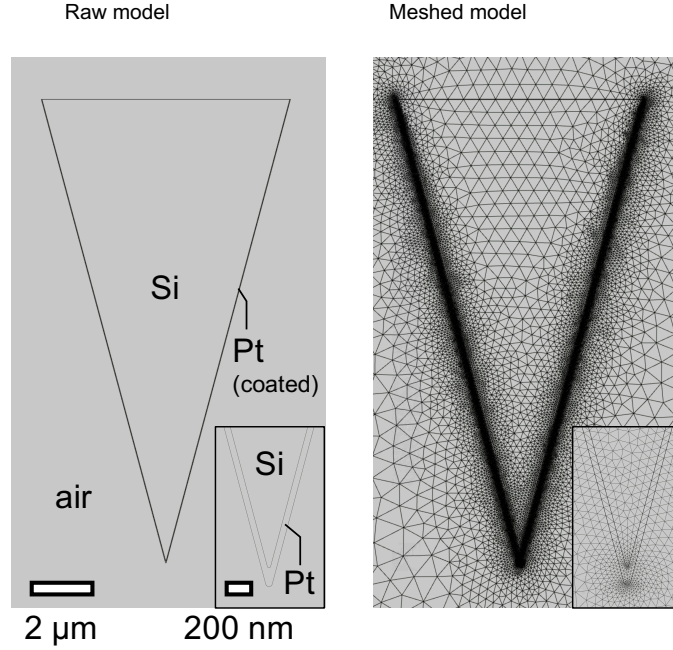


**Figure 2.10:** Meshed geometry of an AFM-tip

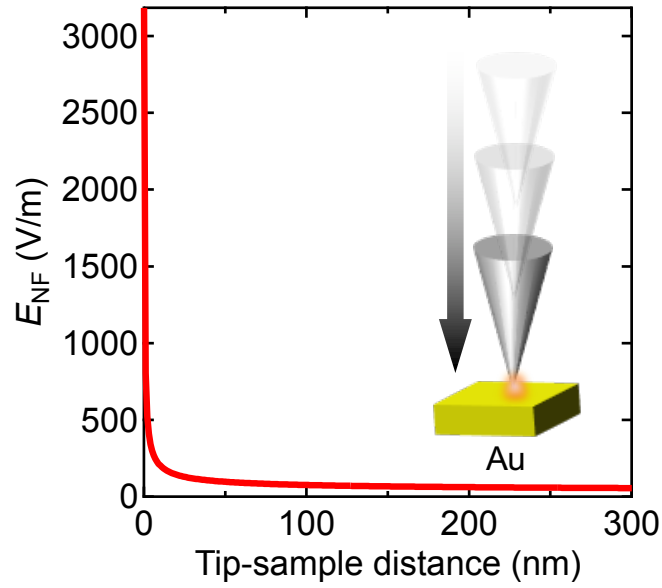
used in the experiments. The apex of the AFM tip was given a radius of curvature of 20 nm based on SEM images (Fig. 2.2).

In this chapter, Au, dielectric Si, and  $\text{CaF}_2$  substrates were investigated, each with a thickness and width set to 100 nm and 30  $\mu\text{m}$ , respectively. To suppress background light and extract the scattered field due to the presence of the tip, a full-field calculation was performed on the substrate alone, and then the scattered field was calculated using the results of the all-field calculation as background light. The irradiation was set to be a p-polarized plane wave with a wavenumber of  $1074\text{ cm}^{-1}$ , which was used in the experiments. The incident angle was  $30^\circ$  to the surface of the host materials. All sides of the simulation volume were surrounded by a perfect matched layer (PML) with a thickness of 1  $\mu\text{m}$ ; this PML attenuates the radiation and prevents reflections from the simulation boundaries.

The mesh conditions are summarized in Table 2.4. In principle, the size of mesh elements in FEM simulations depends on the wavelength, thus the effective wavelength modification needs to be included within the host materials. Therefore, the maximum mesh size for each host material has been divided by the refractive index  $n$ . As an exception, maximum element sizes for metals, such as Au and Pr, were calculated with  $n = 12$ . To accurately simulate the hot spots at the chip-sample junction, the curved surfaces of the filled tip were finely meshed, with 0.4 nm for the Pr apex and 0.2 nm for the Si apex. The PML was meshed using 16 rectangles.

The NFs, especially the electrical field, on an AFM-tip apex ( $E_{\text{NF}}$ ) calculated by FEM,

materials (or location)	element size (m)
Air	$\lambda/6$
Si	$\lambda/(6 \cdot 3.4)$
CaF <sub>2</sub>	$\lambda/(6 \cdot 1.32)$
Au, Pr	$\lambda/(6 \cdot 12)$
the apex of Pr	$4 \cdot 10^{-10}$
the apex of Si	$2 \cdot 10^{-10}$

**Table 2.4:** The mesh condition for the FEM calculation.**Figure 2.11:** Static approach curve for Au substrate.

are shown in Fig. 2.11. In this case, the substrate was set to Au. The field enhancement is maximum just below the chip vertex, so that point was chosen as the observation point. It is observed that the NF light intensity increases exponentially as the tip moves closer to the sample surface.

To incorporate the dynamics of an AFM tip, the tip height ( $h$ ) can be expressed as a sinusoidal function of time ( $t$ ) with a tapping frequency ( $\Omega_{\text{tip}}$ ). Here, the frequency of the incident light is in the terahertz range ( $\sim 10^{12}$ ), while the frequency of the tip motion is in the sub-megahertz range ( $\sim 10^5$ ). Therefore, the motion of the tip can be effectively modeled as a static condition (quasi-static model).

Revised sentences:

Tapping amplitude  $a_{\text{tip}}$  is differently expressed in two regions: one is the tapping region, and the other is a free-standing region. Specifically, in the tapping region,  $h$  becomes smaller, and  $A_{\text{tip}}$  decreases simultaneously due to the repulsion between the sample surface

and the tip [57]. If i assume that an AFM tip symmetrically oscillates with the height  $h(t)$  as the center, the respective values can be written as

$$h = \begin{cases} A_{\text{tip}}/2 & (h \leq h_{\text{tra}}) \\ \max \{A_{\text{tip}}\}/2 & (h \geq h_{\text{tra}}) \end{cases} \quad (2.10)$$

This equation was used to theoretically construct the approach curve, including the dynamics of an AFM tip.

For instance, let's consider a critical point between the tapping and free-standing modes, where  $h_{\text{tra}}$  is set to 52 nm (matching the experimental value obtained later), and the substrate is Au. The time evolution of  $E_{\text{NF}}$ , normalized by the excitation period of the tip, is depicted in Fig. 2.12 (time domain), revealing a strong nonlinearity.

To extract the dynamics of an AFM tip, I perform a Fourier transform of the result, as shown in Fig. 2.13 (frequency domain). In this analysis, the time window is set to one period of AFM tapping time,  $t_{\text{tip}}$ . It's evident from the frequency domain plot that frequency components at integer multiples of the excitation frequency of the AFM appear. These demodulated spectrum amplitudes must correspond to high-order demodulated signals  $\tilde{E}_{\text{NF}}^n$  at harmonic orders  $n$  of an AFM tip oscillation frequency  $\Omega_{\text{tip}}$ .

By calculating  $\tilde{E}_{\text{NF}}^n$  at different values of  $h$ , I can reconstruct the approach curves, incorporating the dynamics of an AFM.

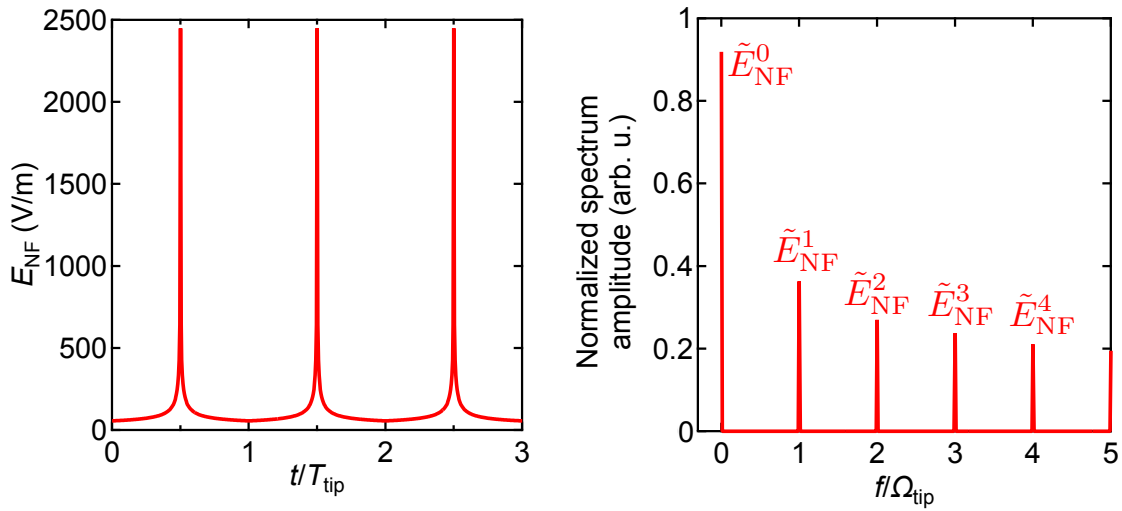


**Figure 2.12:** Time-domain behavior of  $E_{\text{NF}}$  for **Figure 2.13:** Spectrum amplitude of Fourier-transformed  $E_{\text{NF}}$  using Fig. 2.12.

Revised sentences:

The dynamic approach curve for an Au substrate is presented in Fig. 2.14 (dynamic approach curve for Au). When the tip-sample distance is sufficiently far away, the higher-

order modulation components ( $> 2$ ) are almost absent. This theoretical result demonstrates that NF images should be taken with a high-harmonic signal above the second order. Additionally, higher-order harmonic components show a more dramatic increase in the NF signal; this trend theoretically indicates that spatial resolution can be increased using a higher-demodulation NF signal.

An interesting point is that  $\tilde{E}_{NF}^n$  decreases in the tapping region. This feature can be understood by the fact that the effect of the mirror dipole cannot be efficiently removed by excitation, and the nonlinear effect is weakened. This dynamic approach curve theoretically demonstrates that the transition point between tapping and free-standing modes is the most efficient way to obtain the NF components.

To verify the validity of the theoretical model, a comparison with experimental results has been performed. The approach curves obtained by the experiments are shown in Fig. 2.15 (experimental approach curves for Au). The transition height  $h_{\text{tra}}$  was set to be  $\sim 105$  nm, which is the same value as in the theoretical model. As shown in the theoretical model, a peak of  $s_n$  was observed at approximately the transition height  $h_{\text{tra}}$ ; this agreement demonstrates the validity of the dynamic approach curve model. This maximum tendency is not described by the static approach curve (shown in Fig. 2.11), and previous reports[51, 58]. This dynamic approach curve model provides a quantitative explanation for the NF reduction in the approach curve, which has been observed but unexplained in some experiments.

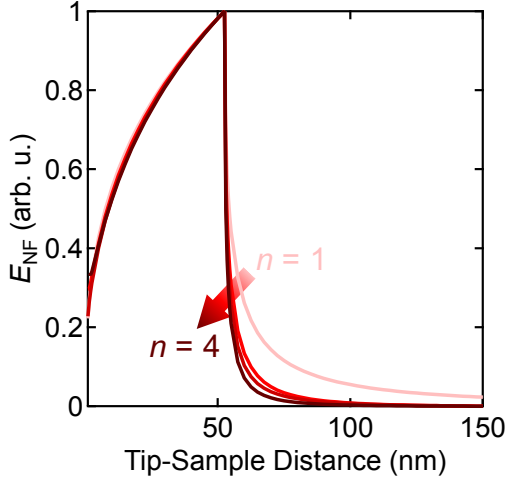


**Figure 2.14:** Dynamic approach curve for an Au substrate.

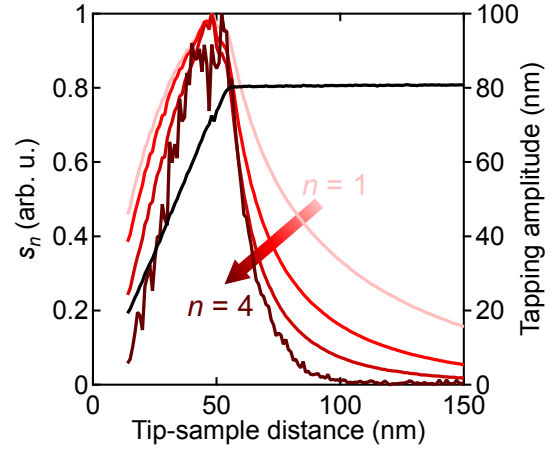


**Figure 2.15:** Experimental approach curve for an Au substrate.

This dynamic approach curve model, derived from the strong nonlinearity due to optical interactions with a host material as explained earlier, is expected to exhibit a strong dependence on the type of host materials. Therefore, I applied the dynamic approach

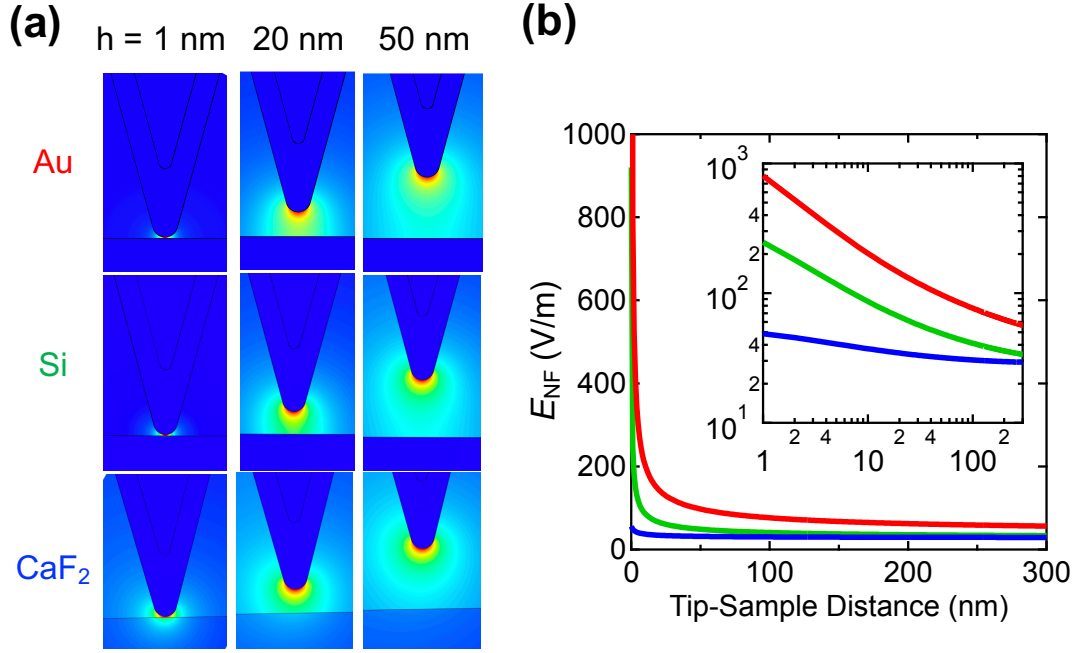


**Figure 2.16:** (a) Electrical distribution of an AFM-tip apex for several tip-sample distances. (b) Static approach curve for three substrates.

curve model to three typical host materials: Au (as described earlier), Si, and CaF<sub>2</sub>. As hypothesized, nonlinearity can be observed from the electric field distribution shown in Fig. 2.16(a)(b) (dynamic approach curves for various host materials), which displays a typical distribution.

The time domain behavior of  $E_{NF}$  at  $h = 75$  nm is shown in Fig. 2.17. Very strong nonlinearity appears in Au, while CaF<sub>2</sub> shows weak nonlinearity (similar to a triangular wave). The dynamic approach curve constructed by applying the process of Fig. 2.17 is shown in Fig. 2.18. A strong dependence on the material can be seen; within the tapping

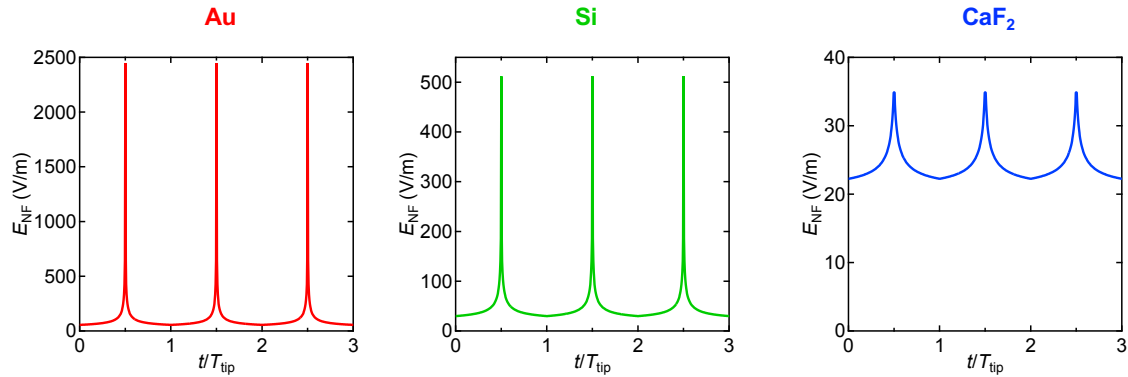


**Figure 2.17:** Time-domain behavior of  $E_{NF}$  for three substrates.

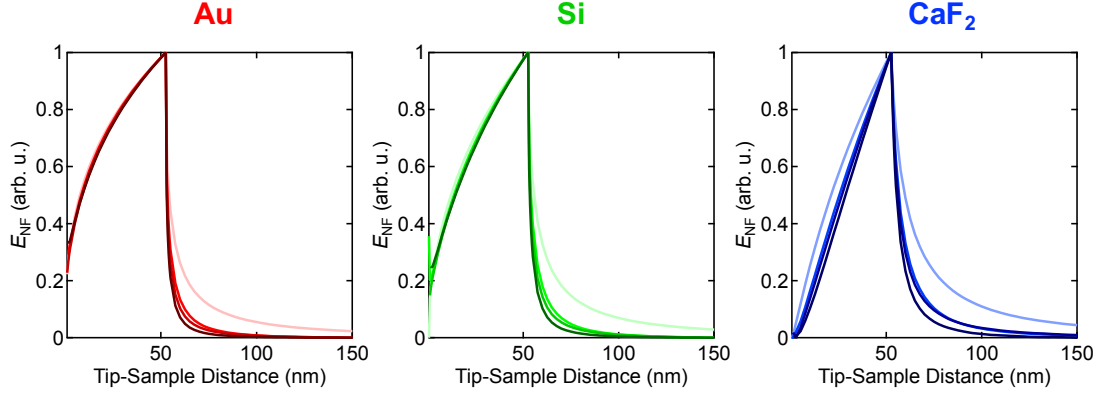


**Figure 2.18:** Dynamic approach curve for three substrates.

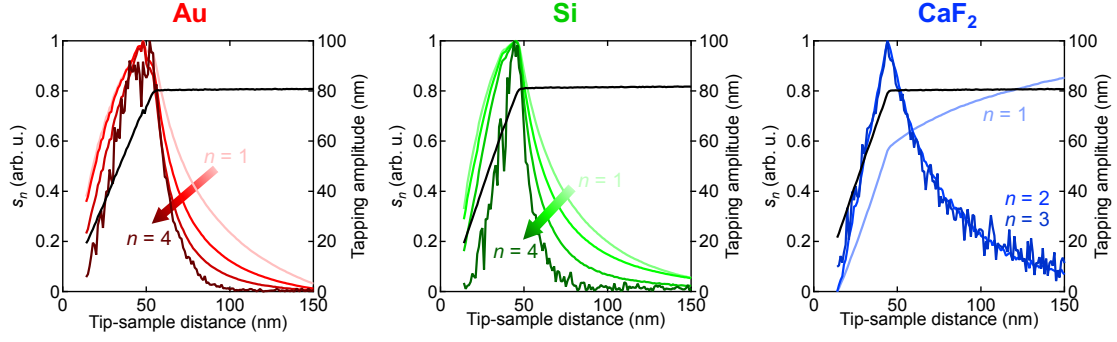


**Figure 2.19:** Experimental approach curve for three substrates. For a  $\text{CaF}_2$  substrate, the 4th-order demodulated result is not shown because it is almost noise level.

region, Au and Si show parabolic behavior while  $\text{CaF}_2$  shows linear behavior. Also, in the free-standing region, a decrease in the decay rate is observed in  $\text{CaF}_2$ ; this corresponds to a poor spatial resolution in the  $z$ -axis. This modification is due to the absence of the mirror dipole in  $\text{CaF}_2$ .

Fig. 2.19 displays the experimentally acquired approach curves for Au, Si, and  $\text{CaF}_2$  substrates. It's notable that the trends closely align with the dynamic approach curve model presented in Fig. 2.18. However, a noticeable deviation is observed, particularly in the case of  $s_1$  and  $s_2$  for  $\text{CaF}_2$ . This discrepancy might arise from the weak NF interaction in  $\text{CaF}_2$ , where the value of the first-demodulated background signal is not negligible. This result is consistent with the simulation results shown in Fig. 2.18.

The developed dynamic-approach-curve model accurately reconstructs the experimental data, indicating its reliability. Therefore, I evaluate the spatial resolution of the developed s-SNOM system using this model.

In Fig. 2.20, I present a comparison of the spatial resolution between the experimental and simulated results. The spatial resolution is defined as the NF signal where its value is  $1/e$ . According to the results, the spatial resolution of the developed s-SNOM is 18.3

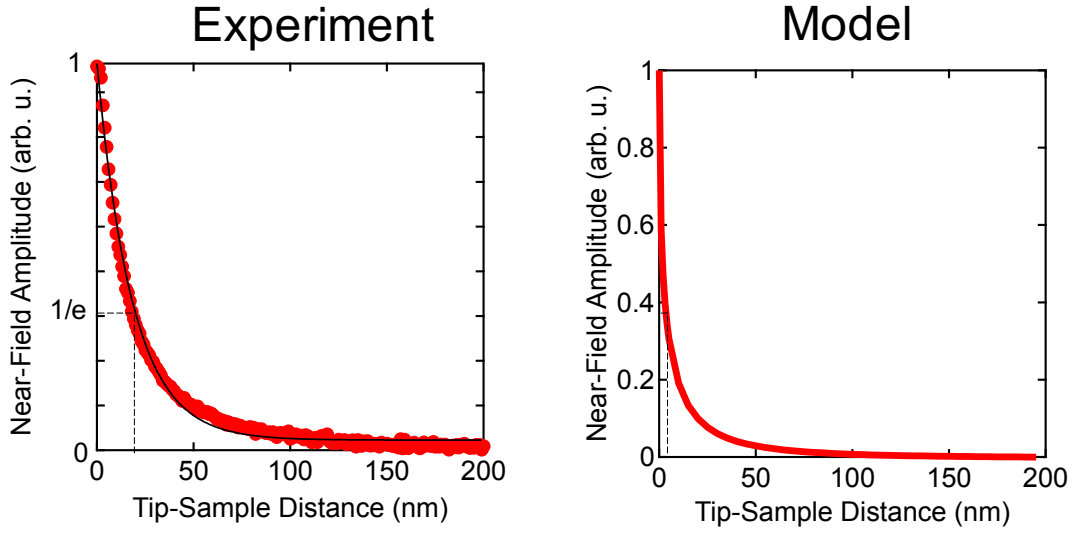


**Figure 2.20:** Comparison of the spatial resolution between the experimental and simulated results.

$\pm 0.2$  nm, whereas the model predicts a resolution of 3.10 nm. This observation suggests that further improvement of the spatial resolution is possible.

## 2.4 Conclusion of Chapter 2

In conclusion, I have successfully developed a phase-resolved s-SNOM. The introduction of reference light has enabled not only NF phase imaging but also improvements in statistical reliability (SNR) and spatial resolution.

To evaluate the current performance of the s-SNOM, I have theoretically developed a quasi-static model of s-SNOM, considering the dynamics of an AFM-tip. This model highlights that the optical tip-sample distance corresponds to the transition height between tapping and free-standing regions, a critical parameter employed in subsequent experiments. Furthermore, the spatial resolution of an s-SNOM is found to be dependent on the host material, emphasizing the importance of carefully selecting host materials for s-SNOM measurements. This observation directly impacts NF images, which is a consideration taken into account in the subsequent chapters. While Si and Au are typically used for optical devices, the difference in their spatial resolutions is qualitatively negligible.





## Chapter 3

# Nanoscale visualization of optical-field vector on an LSA

In this part, I investigate phase-resolved NF imaging of the optical field vector in the logarithmic spiral antenna[34]. Experimental and simulated results provide direct visualization of the characteristics of the logarithmic spiral antennas (LSA), such as its polarization independence with respect to radiation and the rotationally symmetric optical response originating from its geometry. Furthermore, phase mapping measurements indicate a  $\pi$  phase reversal in the out-of-plane direction between two adjacent antenna probes, regardless of the polarization direction. This suggests the presence of a confined and bridged line of electric force.

### 3.1 Introduction & Concept

Optical fields at the nanometer scale can be engineered by designing nanostructures, such as nanoantennas, plasmonic materials, and metamaterials. Micro- and nanoantennas play a crucial role in efficiently transferring the power of irradiated electromagnetic fields to nanostructured materials, enabling various nano-optical investigations of single molecules[32, 59, 60] and nanostructured materials[24, 61, 62].

Because the optical field on these optical devices changes dramatically below the diffraction limit, it is challenging to access its detailed distribution using conventional far-field optical probing techniques. Furthermore, the optical field is characterized by a complex-valued polarization state, i.e., a vector field, rather than a scalar field. As a result, the distribution of the optical field is predominantly discussed through numerical simulations nowadays.

NF optical probing technologies are a powerful tool for achieving ultra-high-spatially

resolved optical investigations beyond the diffraction limit. Recently, various near-field microscopy techniques, including aperture-type SNOM, interferometric SNOM, and s-SNOM [63], have visualized the distribution of the optical field beyond the diffraction limits. This direct visualization provides experimental guidance for optimizing optical devices and exploring new functionalities. Among them, several phase-sensitive s-SNOM techniques enable the probing of both optical field amplitude and phase, which can help restore the vectorial nature of the optical field.

In this section, NF investigations have been conducted using microscale LSAs [34]. They are classified as self-complementary antennas, allowing efficient coupling with optical fields over a broad frequency band. This broadband property simplifies the experimental setup and maintains reproducibility, as precise wavelength selection is not required in the IR region, where IR lasers are less developed and expensive. Furthermore, since the microscale geometry can be integrated with other optical components using well-established microprocessing technologies, the optical-field vector can be examined through various physical quantities, such as electrical responses (as described in Section 4).

## 3.2 Logarithmic spiral antenna

### 3.2.1 Theory

The LSA is a type of spiral antenna<sup>1</sup>. It was first reported by J. D. Dyson in 1961[64]. The geometry of an LSA is constructed by a two-arm spiral or multiple arms arranged symmetrically around a central point. To mathematically describe its geometry, the arms of an LSA are expressed by a spiral equation in polar coordinates, which can be written as

$$r(\theta) = R_{\text{in}} \exp(g\theta) \quad (3.1)$$

, where  $R_{\text{in}}$  represents the inner radius,  $g$  is the growth speed of the arm with  $N$  turns, and  $\theta$  the angle.

Since the length of the arms is finite, an LSA is terminated with an arbitrarily defined radius  $R_{\text{out}} = R_{\text{in}} \exp(2\pi gN)$ . Each radius  $R_{\text{in}}$  and  $R_{\text{out}}$  determines the limit frequencies of desined LSA as

$$\nu_{\text{low}} = \frac{c_0}{2\pi R_{\text{out}}} \quad (3.2)$$

$$\nu_{\text{high}} = \frac{c_0}{2\pi R_{\text{in}}} \quad (3.3)$$

---

<sup>1</sup>There are various types of spiral antennas, including the Archimedean spiral, logarithmic spiral, square spiral, and star spiral antennas

, where  $\nu_{\text{low}}$  and  $\nu_{\text{high}}$  are the lowest and highest operative frequencies of a LSA, and  $c_0$  is the speed of light. Once bandwidth is determined, the  $g$  can be calculated as  $g = (2\pi N)^{-1} \ln(R_{\text{out}}/R_{\text{in}})$ .

Another characteristic of an LSA is its role as a self-complementary antenna. A self-complementary antenna is an antenna of arbitrary shape, where one-half consists of an infinitely wide, perfectly conducting plate, and the remaining hole is completely isomorphic to the shape of the conducting part. Theoretically<sup>2</sup>, an LSA can also be designed and functionalized as a self-complementary antenna.

A unique property of self-complementary antennas is that their polarization, radiation pattern, and input impedance remain independent of frequency over a wide frequency range[2]. The impedance of a self-complementary antenna can be expressed using Babinet's principle[65], as,

$$Z_{\text{slot}} Z_{\text{metal}} = (Z_0/2)^2 \quad (3.4)$$

, where  $Z_{\text{slot}}$  and  $Z_{\text{metal}}$  are the slot antenna impedance and the surface antenna impedance, respectively.  $Z_0 (= \mu_0/4\epsilon_0)$  is the intrinsic impedance of vacuum. Since the self-complementary antenna is a combination of the two in-phase antennas mentioned above, the input impedance  $Z_{\text{in}}$  is

$$Z_{\text{in}} = Z_{\text{slot}} = Z_{\text{metal}} \quad . \quad (3.5)$$

Since permittivity modifies the effective wavelength of electromagnetic fields (also considered in the mesh conditions of FEM in Section 2.3.2), the effective permittivity of the substrate should be taken into account when designing antennas. In the case where the substrate is homogeneous and its thickness is much greater than the antenna size, the effective relative permittivity  $\epsilon_{\text{eff}}$  can be derived as

$$\epsilon_{\text{eff}} = (1 + \epsilon_{\text{sub}})/2 \quad (3.6)$$

, where  $\epsilon_{\text{sub}}$  is a relative permittivity of a substrate. According to this effect,  $c_0$  is effectively modified as  $c' = c_0/\sqrt{\epsilon_{\text{sub}}}$  and then the bandwidth can be calculated by substituting  $c'$  to Eq. (3.2) and (3.3) as  $c_0$ . Additionally, Eq. (3.5) is also changed as

$$Z_{\text{in}}^{\text{eff}} = \frac{Z_0}{2\sqrt{\epsilon_{\text{eff}}}} \quad . \quad (3.7)$$

This modification by the permittivity of the substrate is applicable in various techniques such as improvement of the spatial resolution[66] or miniaturization of antennas[30].

---

<sup>2</sup>in cases where a log-spiral antenna has infinitely extended structures

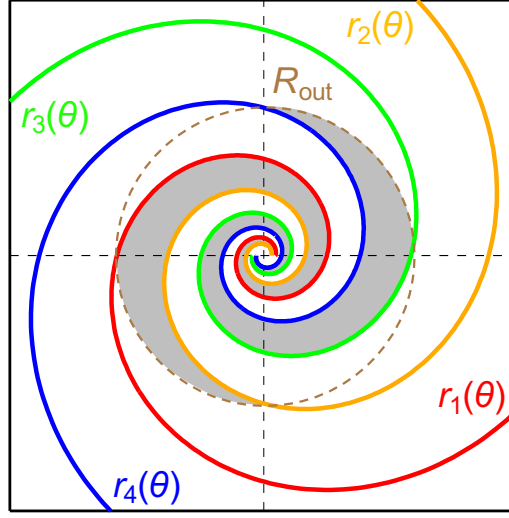


**Figure 3.1:** Designed LSA characterized by (3.8).

### 3.2.2 Design

The LSA was designed through the equations described in the previous section. To determine the geometry of the LSA, four spiral equations are used based on Eq. (3.1) as

$$r_m(\theta) = R_{\text{in}} \exp(g(\theta - 2m\pi / \max\{m\})) \quad (3.8)$$

, where  $m = 1, 2, 3, 4$  in this work.

The parameter values relevant to the LSA are summarized in Table 3.1 and 3.2. The substrate is made of Si with  $\epsilon_{\text{sub}}$ , and the modified resultant effective permittivity is represented in (3.6) .

The bandwidth of this designed LSA falls between  $45.2$  and  $1330 \text{ cm}^{-1}$ , which is optimized for the IR lasers used in this study (as discussed in Section 2.2.2).

The arms of this LSA are designed to be smoothly terminated. Ideally, an LSA has infinitely extended structures; thus, the design of the spiral arms' ends is believed to strongly influence its optical properties. To investigate this arm termination, a non-terminated antenna was compared with the arm-terminated LSA through numerical simulations. The geometry and design parameters of the non-arm-terminated LSA are shown in Table 3.1 and 3.2, respectively.

In Fig. 3.3(a), the  $S_{11}$  parameter of the two LSAs is shown. It was observed that terminating the arms of an LSA significantly reduces the  $S_{11}$  value compared to not terminating them. The behavior of  $Z_{\text{in}}$  also indicates that arm termination closely matches the ideal input impedance described in Fig. 3.3(b);  $Z_{\text{in}}^{\text{eff}}$  is approximately  $75\Omega$  for  $\epsilon_{\text{sub}} = 11.7$  (the permittivity of Si[67]).

parameters	value	unit
$R_{\text{in}}$	0.350	$\mu\text{m}$
$R_{\text{out}}$	10.3	$\mu\text{m}$
$g$	0.30	-
$N$	1.5	rad
$\delta$	$\pi/2$	rad

parameters	value	unit
$R_{\text{in}}$	0.350	$\mu\text{m}$
$R_{\text{out}}$	10.3	$\mu\text{m}$
$g$	0.30	-
$N$	1.5	rad
$\delta_r$	0.45	rad

**Table 3.1:** The parameter value of the designed LSA (arm-terminated).

**Table 3.2:** The parameter value of the non-arm terminated LSA.

Based on these simulation results, the arm-terminated LSA was chosen for the s-SNOM measurements.

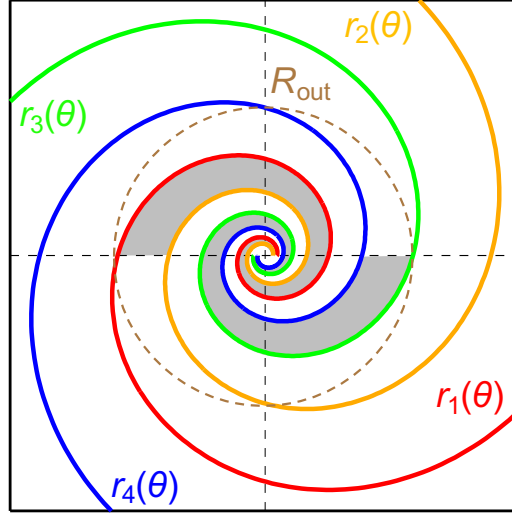


**Figure 3.2:** Designed non-arm-terminated LSA characterized by (3.8)

### 3.3 Method

#### 3.3.1 Fabrication

The LSA was designed using CAD (DraftSight; Dassault Systèmes, France) and then patterned using electron-beam lithography on a Si substrate. The patterned substrate was coated with an Au (100 nm)/Cr (10 nm) film using an electron beam evaporator, followed by a lift-off process. The fabricated LSA is depicted in Fig. 3.4.

#### 3.3.2 Setup

The schematic diagram of the s-SNOM setup for the LSA is depicted in Fig. 3.5. The s-SNOM measurements are described in Section 2.2.2. In this section, I present the NF

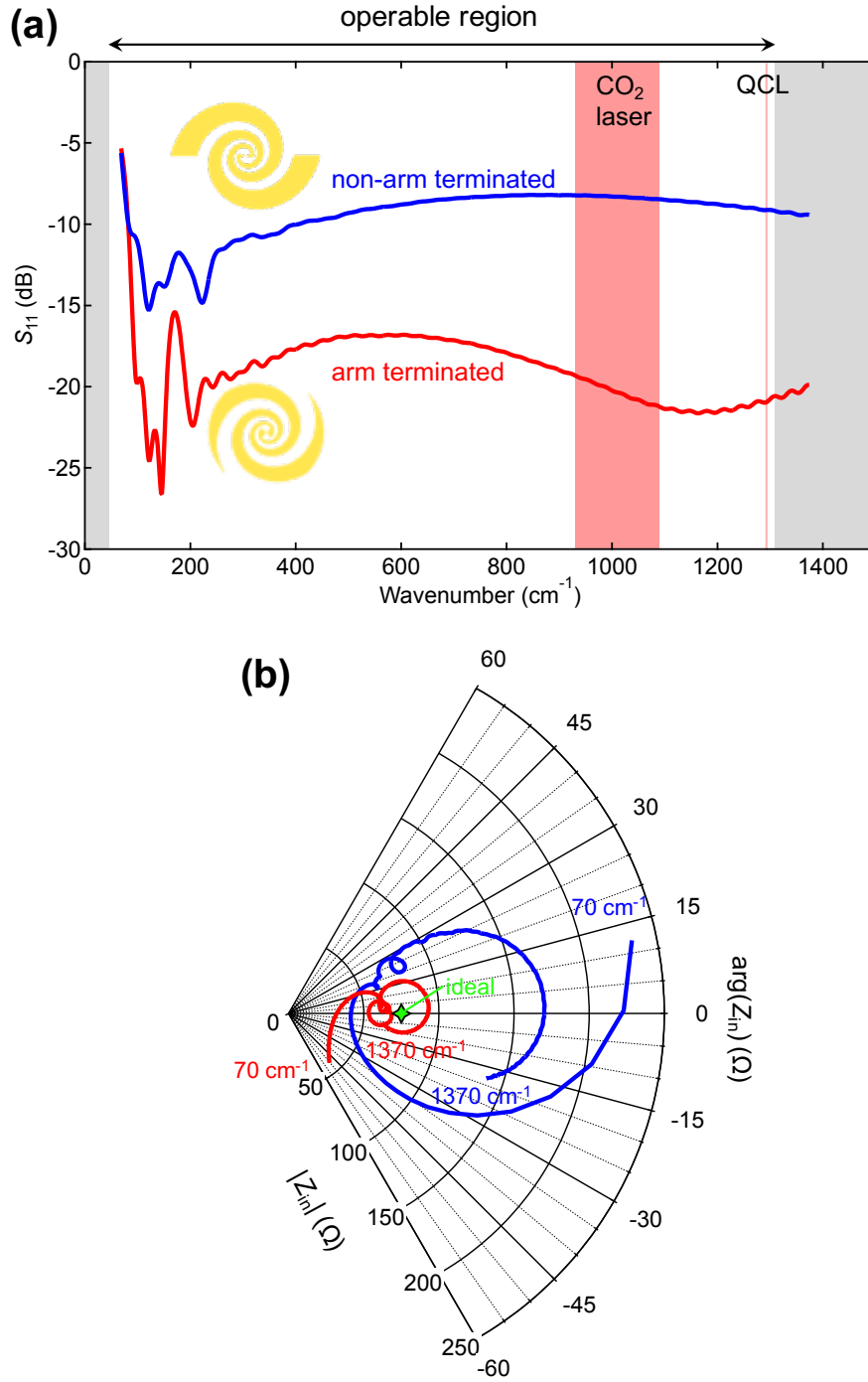


**Figure 3.3:** (a)  $S_{11}$  parameter. (b) Complex impedance in radial coordinates. Adapted from the Ref. [34, 68]. ©2018 The Author(s). Distributed under a Creative Commons Attribution 3.0 and 4.0 International license (CC BY 3.0 and 4.0), respectively

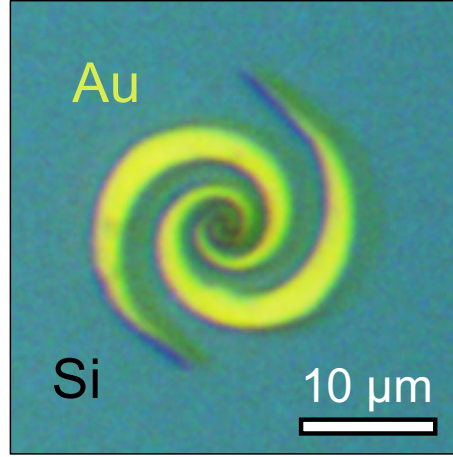


**Figure 3.4:** Optical image of a fabricated LSA.

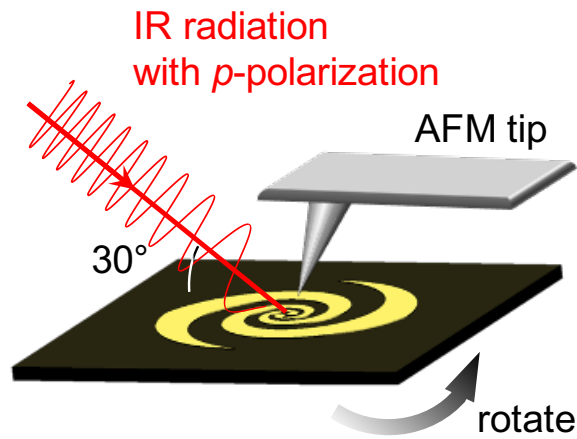


**Figure 3.5:** Schematic illustration of s-SNOM setup for LSA measurements. Adapted from the Ref. [34]. ©2018 The authors. Distributed under a Creative Commons Attribution 3.0 International license (CC BY 3.0).



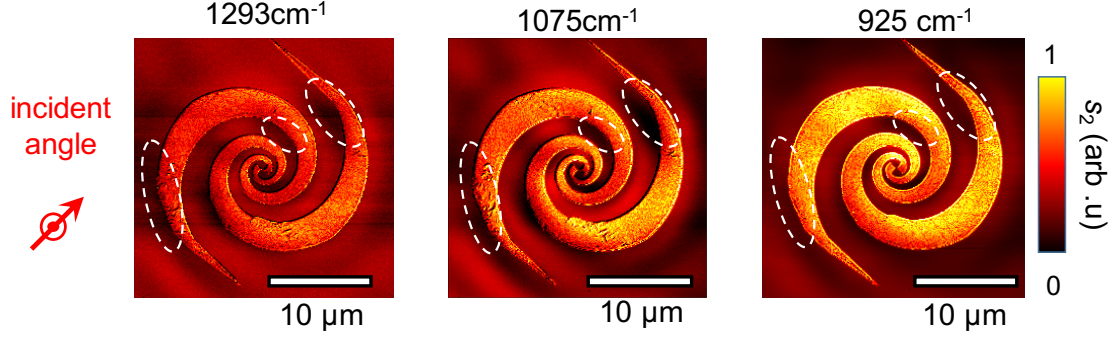


**Figure 3.6:** Wavenumber dependence of the NF images of the LSA.

results for  $n = 2$ , following the theoretical model outlined in Chapter 2. In fact, the data for  $n > 2$  exhibited similar features, thus it is reasonable. To investigate the polarization independence in the direction of radiation, the LSA was rotated by  $\pi/4$  radians in a step-by-step manner, while the optical components and systems remained stationary and undisturbed, as shown in Fig. 3.5.

## 3.4 Experimental results

### 3.4.1 NF-amplitude imaging

The wavenumber dependence of the NF amplitude  $s_2$  of the LSA is shown in Fig. 3.6. The unique patterns, i.e. local decrease in  $s_2$ , are surrounded by dashed circles. These patterns are irrelevant to the wavenumber, which demonstrates the broadband properties of the LSA. The  $s_2$  images are simply expected to correspond to the amplitude of the optical-field vector.

One of the most important results in this part is shown in Fig. 3.7, which illustrates the incident-angle dependence of  $s_2$  in the LSA. It was observed that as the angle ( $\theta$ ) varies, the pattern of the  $s_2$  distribution rotates accordingly. The typical patterns are indicated by being surrounded by black dashed circles, which clearly demonstrate the incident-angle independence.

The corresponding FEM simulation results are shown in the Fig. 3.8, where this numerical simulation has been performed in the same setup as the experimental one except the existence of the AFM tip. For calculated data, I plotted  $\text{norm}, |E_{\text{norm}}|$  inplane  $|E_{\text{in}}|$ , and  $|E_{\text{out}}|$ , defined as  $|E_{\text{norm}}| = \sqrt{E_x^2 + E_y^2 + E_z^2}$ ,  $|E_{\text{in}}| = \sqrt{E_x^2 + E_y^2}$ ,  $|E_{\text{out}}| = |E_z|$ , respectively. These calculated results are taken at the 5 nm above the surface of the LSA and of the Si substrate. The weak patterns observed in experimental data was restored in the simulation data of  $|E_{\text{norm}}|$  and  $|E_{\text{out}}|$ , which demonstrated that  $s_n$  is equivalent to the amplitude of the optical-field vector. However, it is unanswered that the probing

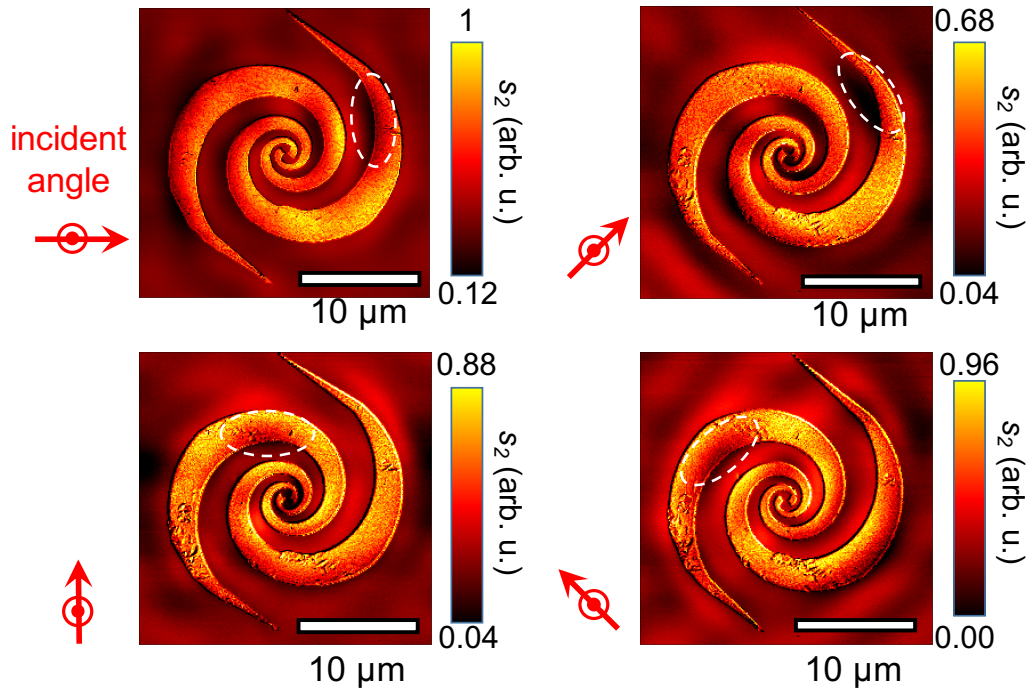


**Figure 3.7:** incident-angle dependence of NF images of the electric fields on the LSA at  $\theta = 0, \pi/4, \pi/2$ , and  $\pi$ . The dashed circles are guides to the eye. Adapted from the Ref. [34]. ©2018 The authors. Distributed under a Creative Commons Attribution 3.0 International license (CC BY 3.0).

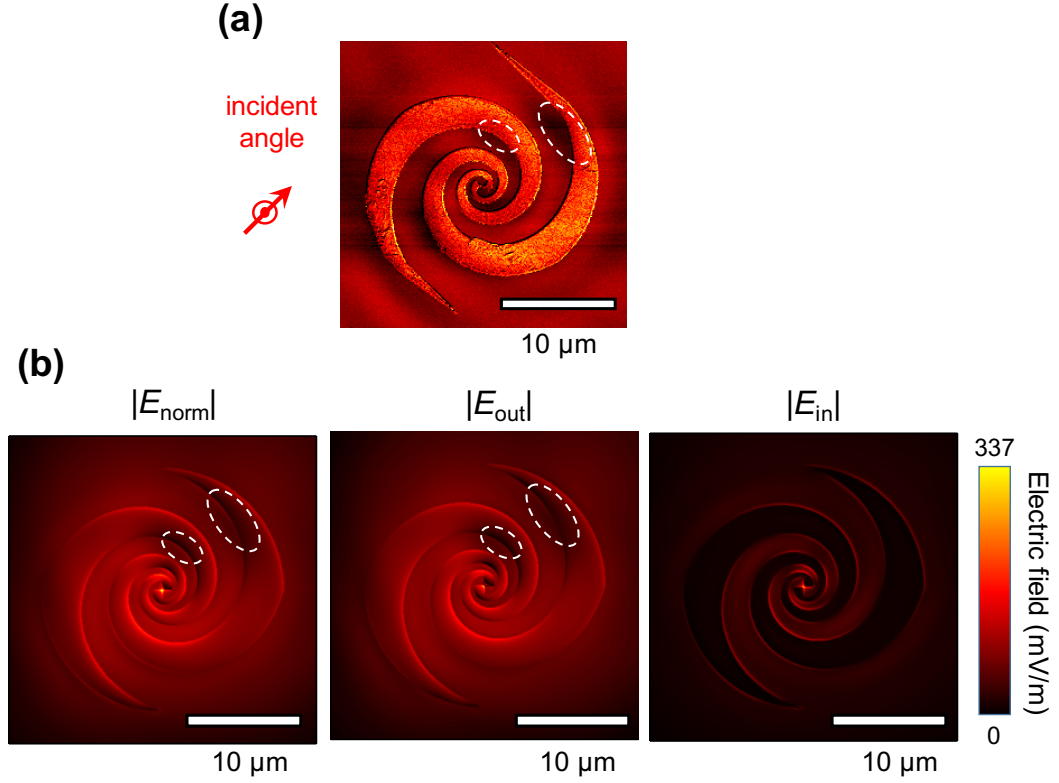


**Figure 3.8:** (a) Experimental result. (b) Calculated data for  $|E_{\text{norm}}|$ ,  $|E_{\text{out}}|$ , and  $|E_{\text{in}}|$

direction of the s-SNOM is independent or out-of plane relative to the surface of the sample due to the similar patterns of  $|E_{\text{norm}}|$  and  $|E_{\text{out}}|$ .

### 3.4.2 NF-phase imaging

To discuss not only amplitude (scalar field) but also the vector field with two physical variables, NF phase imaging was performed. Another significant result is shown in Fig. 3.9, which presents the NF phase distributions of the bow-tie part located at the center of the LSA. These NF phase images indicate a phase reversal at the center of the bow-tie probes for all polarization directions.

It is well-known that a bow-tie antenna alone exhibits a specific polarization dependence, in which its phase jumps by  $\pi$  between the two probes only for the polarization parallel to the two probes. In fact, a similar phase behavior was observed in this s-SNOM measurement, as shown in Fig. 3.10. The phase reversal of the bow-tie antenna is weaker than that of the LSA, which may be due to the size mismatch between the wavelength of the irradiation and the size of the bow-tie antenna (approximately  $\lambda/4$ ).

These results lead to the conclusion that when a bow-tie antenna is combined with a logarithmic-spiral structure, the antenna becomes independent of linear polarization.

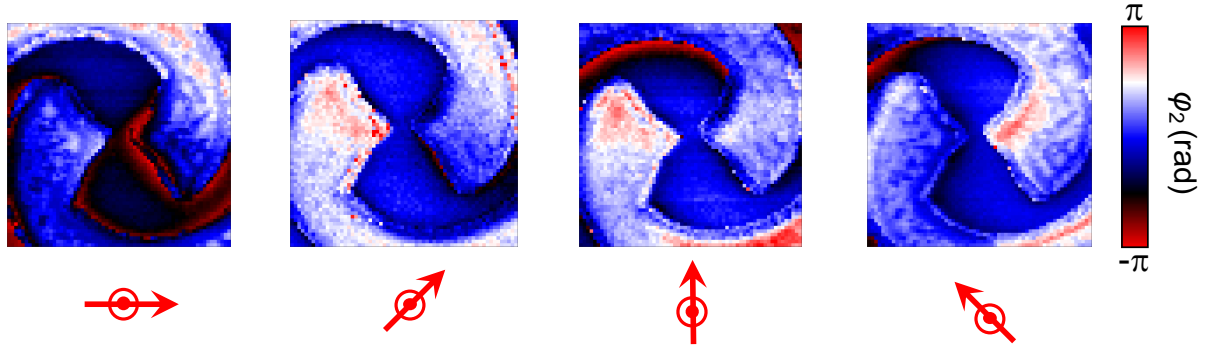


**Figure 3.9:** NF phase at the center of the LSA.

This feature has the advantage of efficiently focusing the optical field without polarization dependency.

## 3.5 Discussion

### 3.5.1 what NF phase shows?

The interesting result obtained is the NF phase reversal observed at the center of the LSA. Such a phase reversal of  $\pi$  has been reported in several studies[69–71]; however, there are also studies reporting non- $\pi$  reversal even for antenna resonance[72]. Therefore, the correspondence of the NF phase to the actual phenomena remains unanswered.

As a hypothesis, the optical-field vector is expected to bridge the two probes located at the center of the LSA, because its center is a hot spot. Thus, I can expect that the NF phase corresponds to the direction of the optical-field vector. To demonstrate this hypothesis, another phase-resolved optical probing technique beyond the diffraction limit is required. Another aspect of this physical picture is the strongly confined optical field vector at the center of the LSA. Such a confined optical field enables efficient coupling with nanostructured materials, which typically do not couple with light of longer wavelengths than their size. Therefore, the response of the nanostructured materials provides experimental evidence of the bridged optical-field vector and leads to a deeper understanding of the physical meaning that the NF phase represents. This approach using nanostructured materials has been demonstrated in Chapter 4.

### 3.5.2 Status of the NF on the tip apex

As shown in Fig. 3.8, the NF amplitude distribution agrees well with both the norm of and the  $z$ -component of the electric field on the surface of the LSA calculated by the finite element method (FEM). This match originates from the weak amplitude of  $|E_{\text{in}}|$ , indicating the potential of s-SNOM for probing the vectorial nature, especially out-of-plane relative

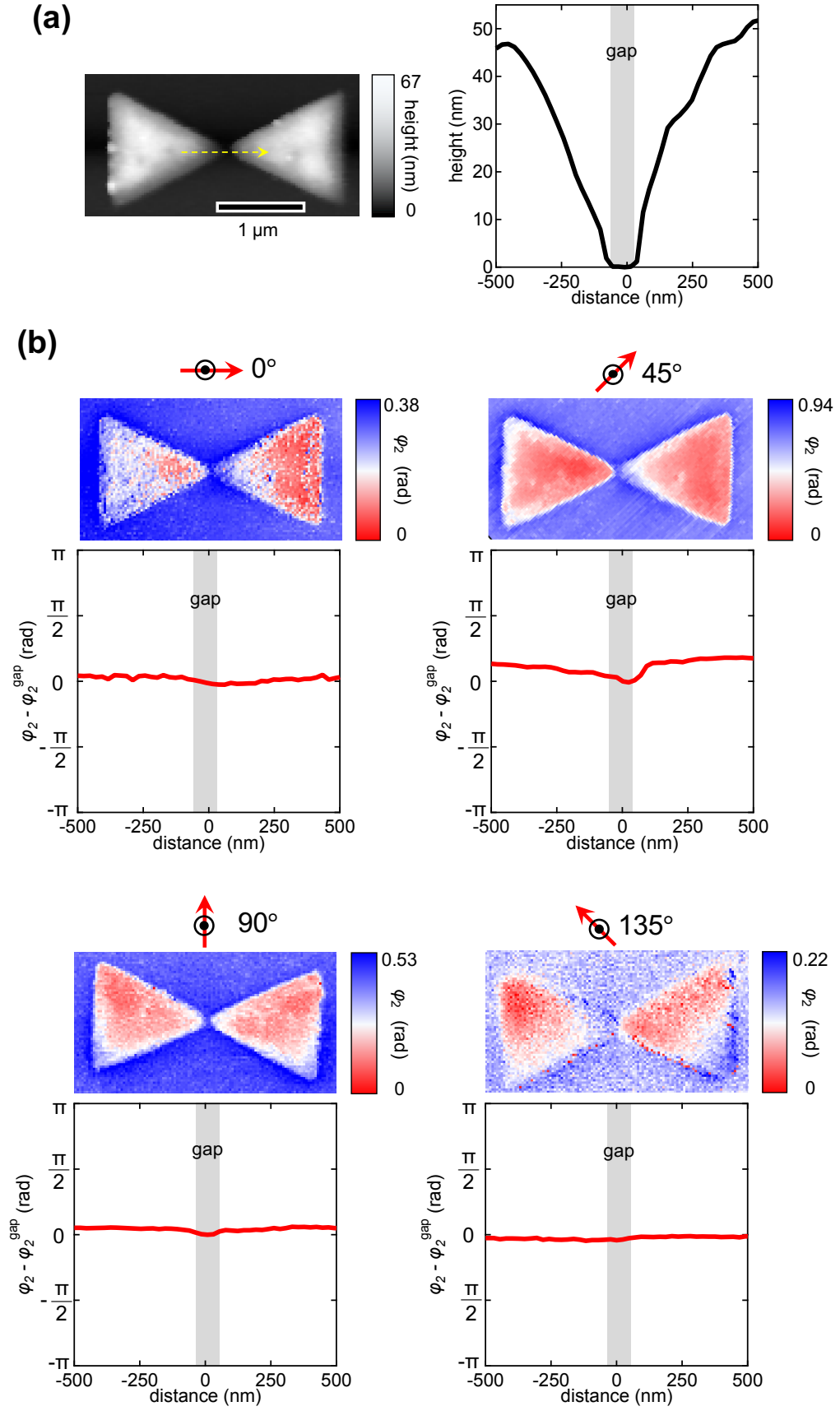
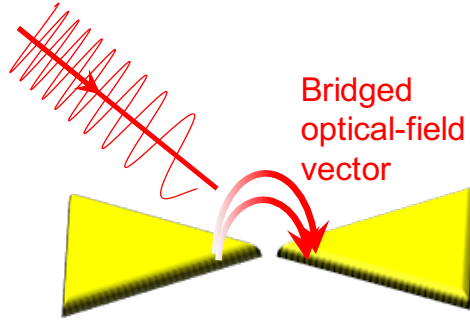


Figure 3.10: Comparison experiment of bow-tie antenna without a spiral structure.



**Figure 3.11:** Illustration of the predicted light field.

to the sample surface. Such vectorial selectivity has been reported in several studies of s-SNOMs [73, 74], while there are also studies [75] that deny such an effect due to the unknown scattering characteristics of an AFM tip. To clarify this unanswered vectorial nature, it will be experimentally investigated in Chapter 5.

### 3.6 Conclusion of Chapter 3

In conclusion, the visualization of the optical-field vector with s-SNOM has been successfully demonstrated on the platform of the LSA. The experimental results are in good agreement with both the norm and  $z$  components of the electric field and reproduce the characteristic properties of the LSA, such as polarization independence and rotational symmetry, beyond the diffraction limit. Furthermore, additional NF phase mapping revealed a  $\pi$  phase jump between the two opposite probes located at the center of the LSA for all polarization directions. This phase jump suggests the existence of bridged electric field lines between the two probes, indicating efficient optical coupling with materials much smaller in size compared to the MIR wavelength.



## Chapter 4

# Electrical approach for local optical-field vector

In this chapter, I delve into the phenomenon of NF reversal at the center of the LSA by conducting electrical transport measurements on a nanostructured highly-doped silicon (Si) transistor. Highly doped Si materials have unique characteristics. Specifically, the energy depth of donor levels and the energy required for tunneling processes between these donor levels are typically on the order of millielectron volts, corresponding to FIR photon energy. These properties make highly-doped Si highly sensitive to optical-induced changes in percolation pathways within Si devices. These changes occur due to modifications in the electrostatic environment caused by incident light, ultimately resulting in the generation of an observable photocurrent [68]. These distinct features enable us to detect the presence of an optical field bridged at the center of the LSA. This electrical signal serves as secondary experimental evidence, supporting the existence of this phenomenon.

### 4.1 Introduction & Concept

Electrons, being highly responsive to external perturbations, serve as a versatile tool for probing a wide range of fields, including electric, electromagnetic, and magnetic fields. Recent advancements in microfabrication techniques have enabled the creation of nanoscale electrical transistors, opening up opportunities to access information about various local fields through the precise design of artificial structures. Consequently, I can explore the previously mentioned central optical confinement through electrical properties, providing secondary experimental evidence.

To avoid interfering with the properties of the LSA, it is crucial to minimize the ratio of



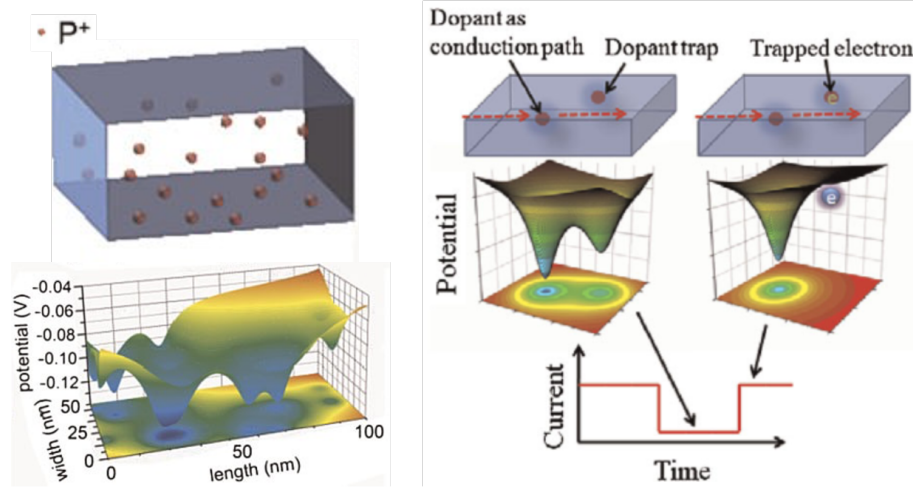


**Figure 4.1:** Left; Potential profile of dopant-rich system in Si. Right; modification of observable current with de-trapped/trapped condition. Reprinted figures with permission from Ref. [21]. Copyright 2011 WILEY-VCH Verlag GmbH & Co. KGaA, Weinheim

photosensors to the LSA. The size of the LSA can be increased, thanks to the broadband properties of self-complementary antennas (as described in Rumsey, 1966). Conversely, to downsize the photosensors while maintaining sensitivity, nanostructured silicon quantum dots (QDs) present a promising solution. QDs exhibit a wide range of highly sensitive optical responses across the electromagnetic spectrum, encompassing microwave, FIR, MIR, NIR, and visible light. This wide spectral range makes them suitable for extracting local information about the optical field.

Moreover, Si-based detectors offer reliability and can be fabricated using mature complementary metal-oxide-semiconductor processes. This advantage allows for precise fabrication, ensuring accurate and repeatable placement at the center of the LSA. In this study, I employed FIR light because it can be externally irradiated similarly to SNOM measurements, using the longest possible wavelength <sup>1</sup>.

As a far-IR response of Si QD, I focused on the donor bands <sup>2</sup> of Si. For highly doped Si with donor bands, the typical energy depths of individual donor levels are known to be on the order of millielectron volts (meV) as shown in Fig. 4.1 [20, 77, 78], corresponding to far-IR photon energies. Irradiating far-IR induces de-trapping processes of electrons trapped in the donor levels, resulting in local polarization. The modification of this polarization strongly alters the local electrostatic environment of percolation pathways in Si devices, leading to the generation of an observable photocurrent. Tabe et al. observed single-electron transport through a single dopant [20] and demonstrated the application of highly

<sup>1</sup>Recently, high-power sub-THz wave sources with approximately 10 mW have become available for free-space transmission (a multiplier-based source, Virginia Diodes, Inc., U.S.)

<sup>2</sup>When increasing donor concentration, each discrete donor level merges and thus forms continuous donor bands [77, 78].

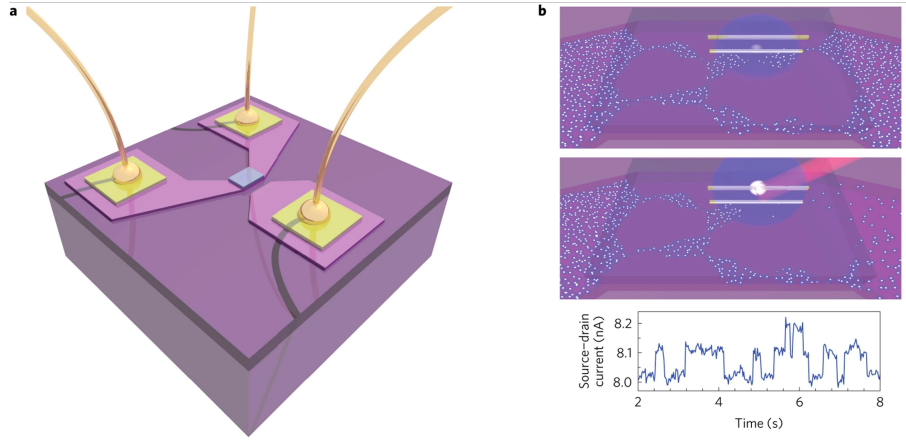


**Figure 4.2:** **a.** Schematic channel structure for probing trapping dynamics on defect state. **b.** Illustration of modification of percolation pathway by changing electrostatic potential. Reprinted figures with permission from Ref. [76]. Copyright 2005 by Springer Nature.

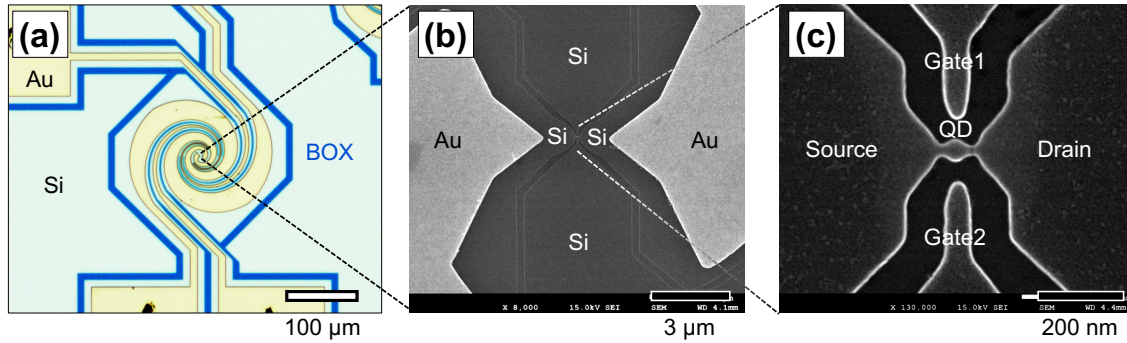


**Figure 4.3:** (a) Optical image of the LSA integrated with Si QD. (b) SEM image of the bow-tie part located in the center of the LSA. (c) SEM image of the Si QD. Adapted from the Ref. [68]. ©2019 The authors. Distributed under a Creative Commons Attribution 4.0 International license (CC BY 4.0).

sensitive photon detectors in the visible light region [21]. Additionally, microwave-induced excitation from donor levels [79, 80] or defect states[76] in the insulator has been recently demonstrated (as shown in Fig. 4.2). Thus, a highly doped Si QD serves as an appropriate platform for investigating the confined optical field at the center of the LSA. This section explores the existence of an optical field bridged at the center of the LSA through the strategies described above, providing secondary experimental evidence.

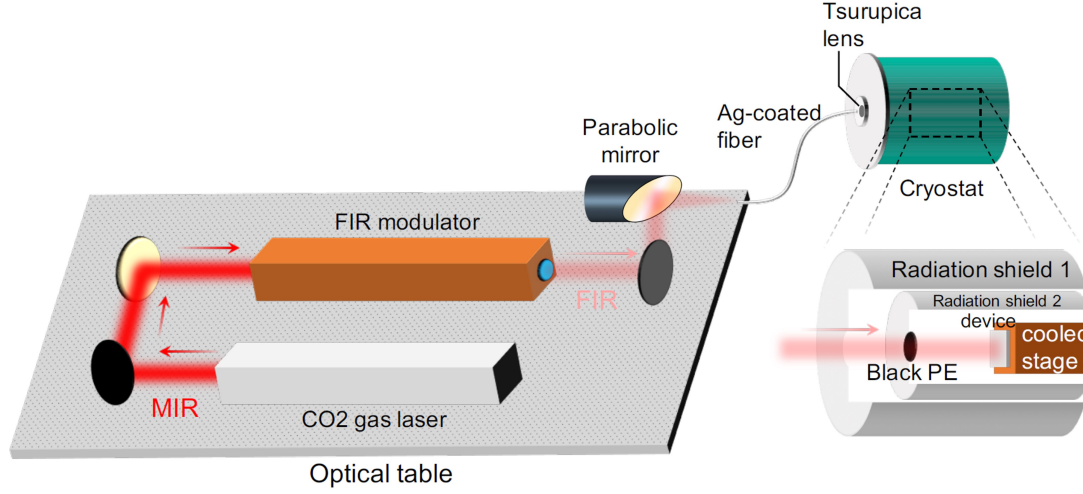


**Figure 4.4:** Optical and cryogenic setup.

## 4.2 Method

### 4.2.1 Device fabrication

The FIR detector integrated with an LSA was fabricated on a silicon-on-insulator (SOI) substrate. The optical image is shown in Fig. 4.3(a). The QD structure and the LSA were lithographically patterned. The LSA part was made of a Au (100 nm)/Cr (10 nm) film, while the QD part was Si (not deposited with metals) as shown in Fig. 4.3(b). To utilize the trapping processes from the donor bands, the QD part shown in Fig. 4.3(c) was doped using phosphine gas flow, with a dopant concentration of approximately  $10^{19} \text{ cm}^{-3}$ .

### 4.2.2 Experimental setup

The temperature of the Si-QD FIR detector was reduced to approximately 3 K using a mechanical refrigerator (NIKI GLASS Co., LTD) as shown in Fig. 4.4. The electrical measurements were conducted using a voltage source (Hewlett-Packard Company, 3245 A), a voltage meter (Agilent Technologies International Japan, Ltd, 34401 A), and a current amplifier (DL Instruments, LLC, Model 1211).

As an FIR laser source, I used a molecular gas laser pumped by a CO<sub>2</sub> laser (FIRL-100: Edinburgh Instruments Ltd.). The frequency of the FIR source could be varied across several frequency lines, ranging from 8.34 to 244  $\text{cm}^{-1}$ , by either tuning the wavelength of the CO<sub>2</sub> pump laser or changing the type of gas, as shown in Table 4.1. The beam was focused and guided using a Tsurupica lens, passing through a silver-coated pipe (3 mm core and 1.2 cm) and a Tsurupica window (7 mm thickness) at room temperature, and then filtered by a black-polyethylene (PE) film at low temperature. The transmission factors

were estimated to be approximately 0.7 for the silver-coated pipe, 0.6 for the Tsurupica window, and 0.4 for the black-polyethylene film, using a power meter (Ophir Optronics, NOVA II).

All measurements were performed at approximately 3 K. This temperature corresponds to  $2.10 \text{ cm}^{-1}$ , which is significantly below the photon energy of the FIR illumination ( $> 19.5 \text{ cm}^{-1}$ ).

Gas	Wavenumber ( $\text{cm}^{-1}$ )	Power (mW)	Gas	Wavenumber ( $\text{cm}^{-1}$ )	Power (mW)
CD <sub>3</sub> OD	244	1	CD <sub>3</sub> OD	39.4	5
CH <sub>3</sub> OH	142	20	CD <sub>3</sub> OH	34.4	10
CH <sub>3</sub> OH	116	10	CD <sub>3</sub> OD	28.0	2
CH <sub>3</sub> OH	<b>103</b>	90	15NH <sub>3</sub>	26.7	50
15NH <sub>3</sub>	89.1	5	CD <sub>3</sub> OC1	26.0	25
CH <sub>3</sub> OH	84.4	150	HCOOH	<b>25.4</b>	40
CH <sub>2</sub> F <sub>2</sub>	81.7	40	HCOOH	24.0	30
CH <sub>3</sub> OH	<b>75.1</b>	1	HCOOH	23.0	40
15NH <sub>3</sub>	65.4	150	HCOOH	<b>19.5</b>	20
CH <sub>3</sub> OH	61.4	36	CH <sub>3</sub> OH	17.7	5
CD <sub>3</sub> OD	<b>54.4</b>	30	<sup>13</sup> CD <sub>3</sub> I	14.3	20
CH <sub>2</sub> F <sub>2</sub>	54.0	150	HCOOH	13.3	2
CH <sub>2</sub> F <sub>2</sub>	51.7	10	<sup>13</sup> CD <sub>3</sub> I	12.3	4
CH <sub>2</sub> F <sub>2</sub>	<b>46.7</b>	100	<sup>13</sup> CD <sub>3</sub> F	8.34	1

**Table 4.1:** frequency of FIR modulator versus gas. The wavenumber described in bold font is used in this experiment.

## 4.3 Experimental results and discussion

### 4.3.1 FIR responses of the LSA-coupled QD

The most important result in this part is shown in Fig. 4.5, where the FIR photocurrent  $I_{\text{FIR}}(\nu) = I(\nu) - I_{\text{dark}}$ , with  $I_{\text{dark}}$  representing the dark current and  $I(\nu)$  denoting the measured current under FIR illumination at a frequency of  $\nu$ . Periodic dark current oscillations relative to  $V_G$  were observed. This strong nonlinearity is well-known as Coulomb blockade, a typical electrical property of zero-dimensional systems. Interestingly, the FIR photocurrent was mainly observed in the Coulomb blockade regions<sup>3</sup>, with weak  $\nu$  dependence.

To discuss the  $\nu$  dependence of  $I_{\text{FIR}}(\nu)$ , the  $\nu$  dependence of the responsivity is plotted in Fig. 4.6, where the responsivity is derived by dividing  $I_{\text{FIR}}(\nu)$  by the irradiation power.

<sup>3</sup>the  $V_G$  region where  $I_{\text{dark}} \sim 0$

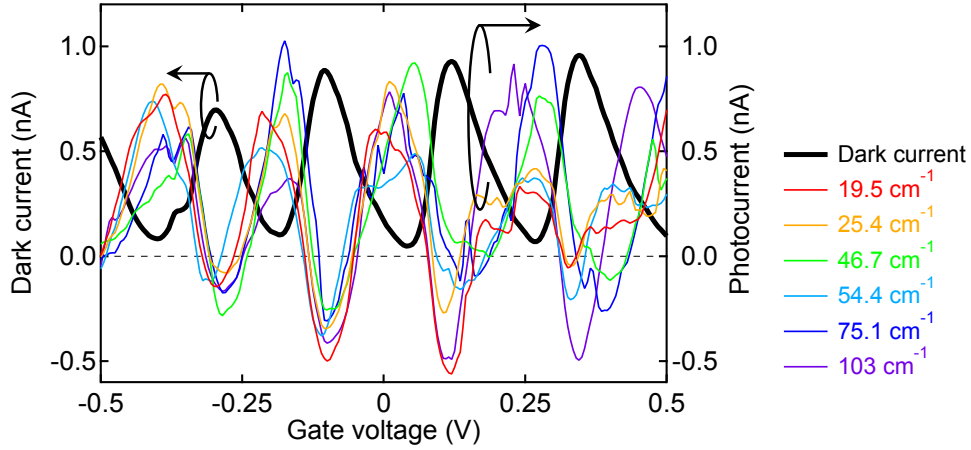


**Figure 4.5:** The  $V_G$  dependence of the dark current  $I_{\text{dark}}$  (the dark curve) and the FIR photocurrent  $I_{\text{FIR}}(\nu)$  (the other colored curves) was recorded at a source-drain voltage of 5 mV under the FIR irradiation with six frequencies.

The FIR power onto the devices was estimated to be several tens of nW using transmission factors. The effective photoactive area was approximated as a square of the FIR wavelength, a common approach for materials much smaller than the wavelength. The results for fixed  $V_G$  responsivity were derived through fitting analysis of a Lorentz function. This broadband-dependent behavior can be observed in the wavenumber dependence of the responsivity, and it is reasonable to attribute this broadband response to the optical properties of both the LSA and the QD. The former has already been demonstrated in Chapter 3, but the latter is still unclear.

Here, I discuss the origin of the appearance of  $I_{\text{FIR}}(\nu)$  in a broadband manner. One of the possible mechanisms is photon-assisted tunneling[23, 81, 82]; the electron tunneling process via optical excitation of photon energies. Through this process, irradiation with different photon energies impacts the peak position of the photocurrent<sup>4</sup> as shown in Fig. 4.7[23, 83]. However, the peak positions of the FIR photocurrent seem to be unrelated to the photon energy of the radiation. Therefore, photon-assisted tunneling processes are not the dominant mechanism of the FIR photocurrent in the Coulomb blockade region.

Another possible mechanism is the FIR response of the donor bands, which is separated by two factors: One is the detrapping processes from individual localized energy states created by the donor levels depicted as (I) in Fig. 4.8. This typical energy depth is known to be of the order of FIR-photon energies, which corresponds to FIR photon energy [84]. Note that this energy depth effectively decreases compared to that of an isolated donor ( $\sim 45$  meV for phosphorus) because the donor level broadens into bands. The other is FIR-assisted tunneling to empty donor levels depicted as (II) in Fig. 4.8. Both of these processes lead to an FIR-induced polarization field  $P$  and strongly modify the local

<sup>4</sup>referred to as "satellite peaks"

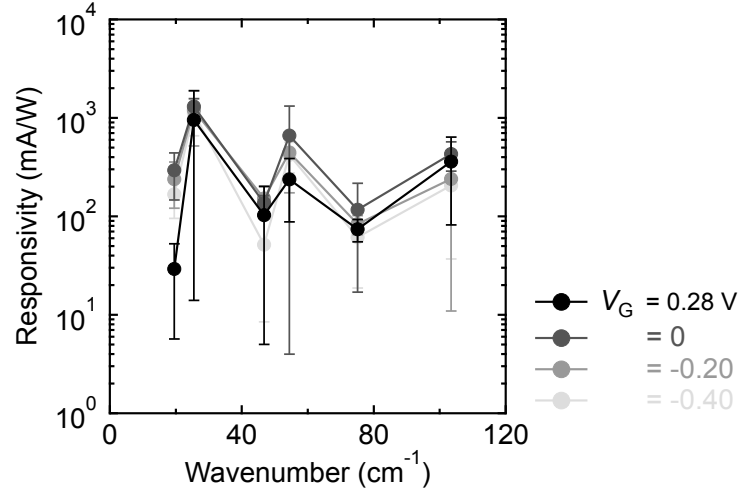


**Figure 4.6:** Frequency dependence of the responsivity at the various  $V_G$ . Adapted from the Ref. [68]. ©2019 The authors. Distributed under a Creative Commons Attribution 4.0 International license (CC BY 4.0).

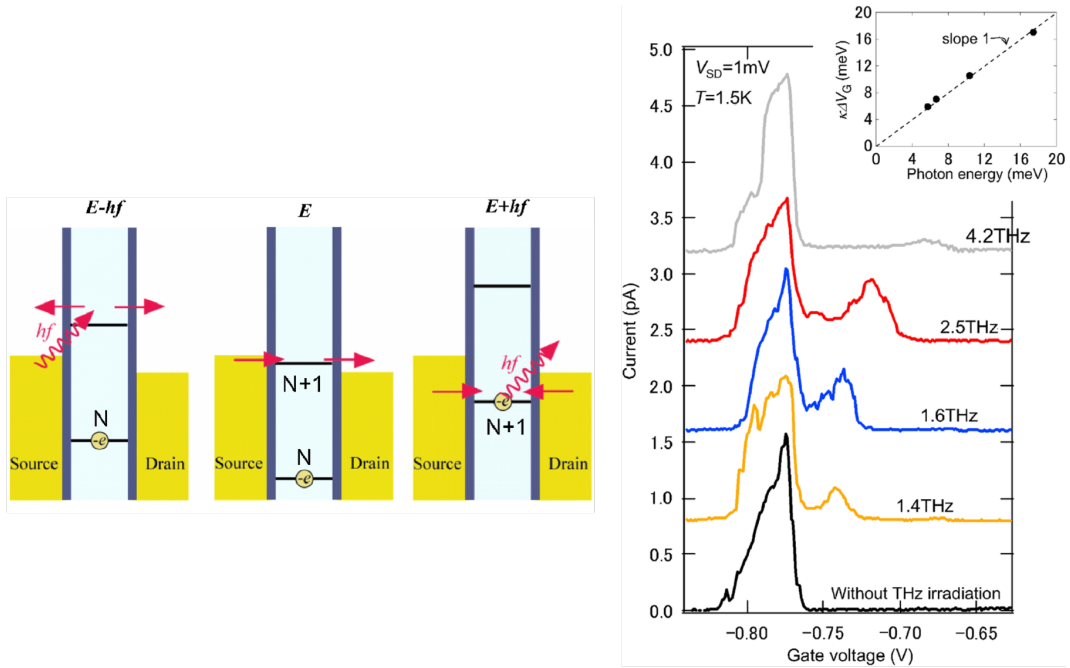


**Figure 4.7:** left: schematic of the photon-assisted tunneling process. right: Satellite peaks observed in the Coulomb blockade. The inset shows the peak position of the satellite peak versus the photon energy of irradiation. Reprinted figures with permission from Ref. [23]. Copyright 2008 AIP Publishing.

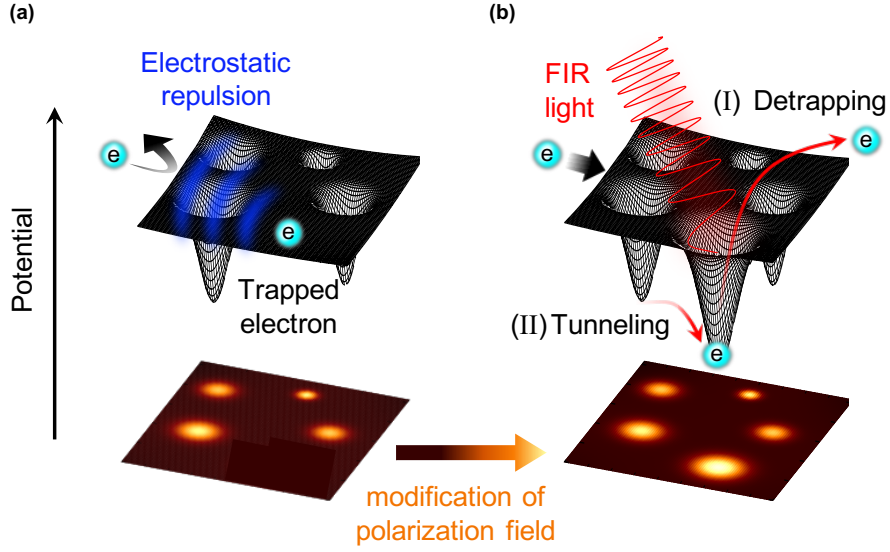


**Figure 4.8:** Schematic view of the FIR responses in the Coulomb blockade region in dark conditions (a) and under FIR irradiation (b). (I) detrapping process of the localized electron in donor levels. (II) FIR-assisted single-electron tunneling between the donor levels. These processes provide the modification of the polarization field as shown in the bottom plains. Reproduced from the Ref. [68]. ©2019 The authors. Distributed under a Creative Commons Attribution 4.0 International license (CC BY 4.0).

electrostatic environment of percolation pathways in the Si QD. This modification is assumed to lead to the generation of an observable photocurrent[21, 76]. Additionally, these processes occur at various energy levels in donor bands, leading to broadband responses. The number of dopants is estimated to be  $\sim 40$  by calculating the volume of the QD and dopant concentration, thus making multiple excitation/tunneling reasonable. To explain this process, I will attempt to theoretically reveal the occurrence of this FIR photocurrent in the next section.

### 4.3.2 theoretical analysis

The phenomena depicted in Fig. 4.8 are governed by quantum mechanics, thus it should be described using Hamiltonian. This system consists of the two-level system (TLS) with trapped  $|1\rangle$  and de-trapped  $|2\rangle$  states in the QD, and external FIR waves (AC external electric field with terahertz ( $\sim 10^{12}$ ) frequency), which can be expressed by the Hamiltonian  $\hat{\mathcal{H}}$  as

$$\hat{\mathcal{H}} = \hat{\mathcal{H}}_{\text{TLS}} + \hat{\mathcal{H}}_{\text{ext}} \quad (4.1)$$



, where  $\hat{\mathcal{H}}_{\text{TLS}}$  and  $\hat{\mathcal{H}}_{\text{ext}}$  represent the Hamiltonian of the TLS and of its interaction with the external FIR waves with the frequency  $\omega_{\text{ext}}$ <sup>5</sup>, respectively. The time( $t$ )-dependent wavefunction of this system is described as  $|\Psi(t)\rangle = c_1 |1\rangle + c_2 e^{-i\omega_{\text{ext}}t} |2\rangle$ . The population of each state is described using density matrix  $\rho(t) = |\Psi(t)\rangle \langle \Psi(t)|$ , whose elements are  $\rho_{mn} = c_m c_n^* (m, n = 1, 2)$ .

The first term of Eq. (4.1) is given by  $\hat{\mathcal{H}}_{\text{TLS}} = (\hbar\omega_{12}/2)\sigma_z$ , where  $\omega_{12}$  is transition frequency of the TLS, and  $\sigma_z = \text{diag}(1, -1)$  is Pauli matrix. The second term of Eq. (4.1) is expressed as  $\hat{\mathcal{H}}_{\text{ext}} = -\boldsymbol{\mu} \cdot \mathbf{E}_{\text{ext}}(t) = -\boldsymbol{\mu} \cdot \mathbf{E}_0 e^{i\omega_{\text{ext}}t}$  using dipole moment  $\boldsymbol{\mu}$ ; where I used dipole approximation because this system is much smaller than wavelength of the FIR waves ( $\sim$  several-hundreds micrometers). To describe  $\hat{\mathcal{H}}$  with the interaction picture as  $\hat{\mathcal{H}}_i$ , I performed a unitary transformation  $\hat{U} = \exp(-i\hat{\mathcal{H}}_{\text{TLS}}t/\hbar)$ ;

$$\hat{\mathcal{H}}_i = \hat{U}^\dagger (\hat{\mathcal{H}} - \hat{\mathcal{H}}_{\text{TLS}}) \hat{U} \quad (4.2)$$

$$= -\Delta |1\rangle \langle 1| - \hat{U}^\dagger (\boldsymbol{\mu} \cdot \mathbf{E}) \hat{U} e^{i\omega_{\text{ext}}t} \quad (4.3)$$

$$= \frac{1}{2} \begin{pmatrix} 0 & -\langle 1 | \boldsymbol{\mu} | 2 \rangle \cdot \mathbf{E}_0 (1 + e^{-2i\omega_{\text{ext}}t}) \\ -\langle 2 | \boldsymbol{\mu} | 1 \rangle \cdot \mathbf{E}_0 (1 + e^{2i\omega_{\text{ext}}t}) & -2\hbar\Delta \end{pmatrix} \quad (4.4)$$

where  $\Delta = \omega_{\text{ext}} - \omega_{12}$  is the detuning between the transition frequency of the TLS and of the external FIR waves. By using rotating-wave approximation,  $\hat{\mathcal{H}}_i$  is deformed into  $\hat{\mathcal{H}}_{\text{RWA}}$  without time dependence

$$\hat{\mathcal{H}}_{\text{RWA}} = \frac{1}{2} \begin{pmatrix} \hbar\Delta & -\langle 1 | \boldsymbol{\mu} | 2 \rangle \cdot \mathbf{E}_0 \\ -\langle 2 | \boldsymbol{\mu} | 1 \rangle \cdot \mathbf{E}_0 & -\hbar\Delta \end{pmatrix} \quad (4.5)$$

$$= -\frac{\hbar}{2} \begin{pmatrix} -\Delta & \Omega \\ \Omega & \Delta \end{pmatrix} \quad (4.6)$$

where  $\Omega = \langle 1 | \boldsymbol{\mu} | 2 \rangle \cdot \mathbf{E}_0 / \hbar$  is the Rabi rate, which is a positive real value owing to adequate adjustment of the phase of the wavefunction.

In the TLS, damping processes have to be taken into account. To describe such processes phenomenologically, the motion equation of  $\rho(t)$  is expressed with the  $\hat{\mathcal{H}}$ :

$$\partial_t \rho(t) = -\frac{i}{\hbar} \left[ \hat{\mathcal{H}}_{\text{TLS}} + \hat{\mathcal{H}}_{\text{RWA}}, \rho(t) \right] \quad (4.7)$$

Here, the two damping processes are conceivable: One is the FIR-induced emission and absorption processes with rates  $\Gamma$ , and another is an intrinsic dephasing process with rates  $\gamma$ . These damping processes are phenomenologically introduced as  $\gamma_a = \Gamma/2 + \gamma$ . By using

---

<sup>5</sup>Here,  $f$  is described as  $\omega_{\text{ext}}$ , because angular frequency  $\omega$  is usually used in quantum mechanics.



these damping rates, Eq. (4.7) is transformed as

$$\partial_t \rho(t) = \begin{pmatrix} -i\frac{\Omega}{2}(\rho_{21} - \rho_{12}) + \Gamma\rho_{22} & -i\frac{\Omega}{2}(\rho_{22} - \rho_{11}) - (\gamma_a + i\Delta)\rho_{12} \\ i\frac{\Omega}{2}(\rho_{22} - \rho_{11}) - (\gamma_a - i\Delta)\rho_{21} & i\frac{\Omega}{2}(\rho_{21} - \rho_{12}) - \Gamma\rho_{22} \end{pmatrix} \quad (4.8)$$

To discuss the occurrence of the FIR-induced current in the following section, the steady-state solution is solved by setting the time derivatives to 0.

$$\rho_{21}^{\text{ste}} = \frac{\Omega}{2} \frac{\Gamma(\Delta - i\gamma_\alpha)}{\Gamma(\gamma_\alpha^2 + \Delta^2) + \gamma_\alpha \Omega^2} \quad (4.9)$$

Here, let us discuss the FIR-induced photocurrent  $I_{\text{FIR}}(t)$ . Given that a typical dopant energy level corresponds to an FIR photon energy due to intrinsic dephasing, I assume that the complex conductivity  $\sigma(t)$  can be expressed as  $\sigma(t) = \sigma_0 \exp\{(-i\omega_b - \Gamma_b)t\}$ , where  $I_{\text{FIR}}(t)$  is resonant with the frequency  $\omega_b$  and dephasing rate  $\Gamma_b$ .

Through linear response theory,  $I_{\text{FIR}}(t)$  is given by:

$$I_{\text{FIR}}(t) = \int_0^t \sigma(t-t')E(t')dt' \quad (4.10)$$

Through the time-derivative of Eq. (4.10), the motion equation of  $I_{\text{FIR}}(t)$  can be obtained as:

$$\partial_t I_{\text{FIR}}(t) = -(i\omega_b + \Gamma_b)I_{\text{FIR}}(t) + \sigma_0 E(t) \quad (4.11)$$

$E(t)$  is the total electric field having two contributions: one is the external FIR field  $E_{\text{ext}}(t) = E_0 \exp(i\omega_{\text{ext}}t)$ , and another is the field induced by the ionized dopants with polarization  $P(t)$ :

$$P(t) = \langle \Psi(t) | -\boldsymbol{\mu} | \Psi(t) \rangle \quad (4.12)$$

$$= \mu \rho_{21} e^{i\omega_{\text{ext}}t} \quad (4.13)$$

$P(t)$  effectively contains photon-assisted tunneling between donor levels, because this process requires the empty donor levels created by de-trapping processes through the Pauli exclusion principle. Substituting Eq. (4.13) into Eq. (4.11) yields

$$\partial_t I_{\text{FIR}}(t) = -(i\omega_b + \Gamma_b)I_{\text{FIR}}(t) + \sigma_0 (E_0 + \mu \rho_{21}/\epsilon_r) e^{i\omega_{\text{ext}}t} \quad (4.14)$$

where  $\epsilon_r$  represents the dielectric function of highly doped Si. Introducing  $\tilde{I}_{\text{FIR}}(t) =$

$I_{\text{FIR}}(t)e^{-i\omega_{\text{ext}}t}$  removes the fast rotating term  $e^{i\omega_{\text{ext}}t}$ ; which transform the Eq. (4.14) to

$$\partial_t \tilde{I}_{\text{FIR}}(t) = i(\Delta + \delta) \tilde{I}_{\text{FIR}}(t) - \Gamma_b \tilde{I}_{\text{FIR}}(t) + \sigma_0 (E_0 + \mu\rho_{21}/\epsilon_r) \quad (4.15)$$

where,  $\delta = \omega_{12} - \omega_b$  is the frequency difference between the TLS and the background resonance. The steady current  $I^{\text{ste}}$  can be derived by setting the time derivatives to 0 in Eq. (4.15) as:

$$I_{\text{FIR}}^{\text{ste}} = \frac{\sigma_0}{\Gamma_b - i(\Delta + \delta)} (E_0 + \mu\rho_{21}^{\text{ste}}/\epsilon_r) \quad (4.16)$$

This result of Eq. (4.16) gives an analytical description of FIR-induced photocurrent, which is expected to correspond to the FIR photocurrent observed in Fig. 4.5.

In the Coulomb blockade regions, there are many trapped electrons but few conducting electrons (easily affected by  $P$ ). Therefore, the second term of transition processes  $\rho_{21}^{\text{ste}}$  is governed by Eq. (4.9). Meanwhile, in the resonant transmission regions where  $I_{\text{dark}}$  is observed, the eigenstates are almost governed by de-trapped states  $|2\rangle$ . Since this situation leads to the strong suppression of transition processes  $\rho_{21} \sim 0$ , the second term in Eq. (4.16) is negligible. The above-mentioned discussion suggests that the Fermi-level dependence of  $\rho_{21}$  yields the gate-voltage dependence of the FIR-induced photocurrent, thus indicating that the FIR-induced photocurrent observed in the Coulomb blockade regions mainly originates from the transition processes in the TLS of the trap/de-trapped states. Although this theoretical expression phenomenologically explains broadband photocurrent, experimental proof is strongly required. Since donor atoms are randomly arranged on the atomic scale, nanoscale space-resolved photocurrent measurements are one of the promising candidates (described in Chapter 7.3.2 of Chapter 7).

The negative FIR photocurrents observed in the resonant transmission region may originate from the pumping phenomenon, in which current flows from the source to the drain in the positive direction and from the drain to the source in the negative direction. This phenomenon has been observed in various research, for example, the pumping phenomenon is observed when the current flows in the negative direction by photon-assisted tunneling [83], and the method of raising and lowering the tunnel barrier by using a gate is also used. This transition of (dis/)appearance in the Coulomb blockade/resonant transmission region remains an unanswered phenomenon.

### 4.3.3 Control experiment for the effect of LSA

To verify the effect of the LSA, control experiments of a QD device without an LSA were performed. The non-LSA Si QD was fabricated using the same processes used for the LSA-coupled QD device as shown in Section 4.2.1.

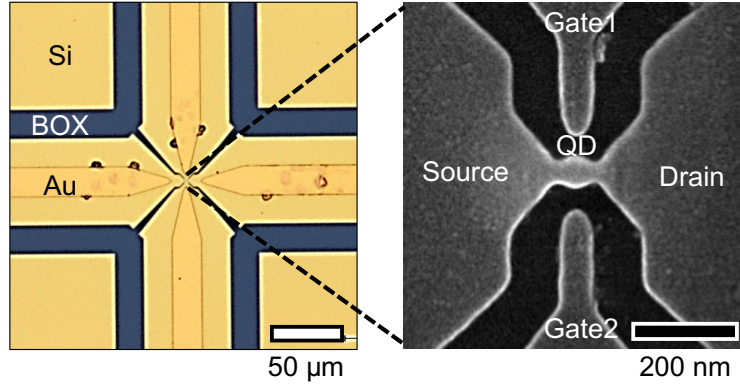


**Figure 4.9:** Optical and SEM images of non-LSA-integrated QD. Reproduced from the Ref. [68].  
 ©2019 The authors. Distributed under a Creative Commons Attribution 4.0 International license (CC BY 4.0).

Because FIR photocurrents are very weak, the FIR photocurrent signal was further amplified by a lock-in amplifier (NF Corporation, LI5640). The other setup is the same as the one used for the LSA-coupled QD.

Fig. 4.10 compares the responsivities between the two types of QD detectors under FIR irradiation at  $103 \text{ cm}^{-1}$ . For the LSA-coupled QD, oscillations in responsivity can be observed, which are attributed to the trapping processes discussed earlier. Conversely, the non-LSA-coupled QD exhibits a non-oscillatory trend, indicating that FIR waves do not excite FIR responses in the QD. The maximum responsivity values are  $10^2 \text{ mA/W}$  and  $10^{-2} \text{ mA/W}$  for the LSA-coupled and non-LSA-coupled QD, respectively. Thus, the enhancement factor resulting from the presence of the LSA is approximately  $10^4$ . These results confirm that the nanostructured QD located at the center of the LSA efficiently couples with FIR waves.

Equation (4.16) also explains the difference in FIR-induced photocurrent between the antenna-coupled and non-antenna QD devices. Since the QD device without such an antenna cannot efficiently couple with the FIR waves, the FIR electric field on the non-antenna QD device is much weaker than that on the antenna-coupled QD device. This fact directly results in the decrease in the contribution of the first term in (4.16). Additionally, such a weak electric field hardly excites the electrons trapped in individual dopant potentials; hence, the eigenstates are almost determined by trapped states  $|1\rangle$ , and consequently,  $\rho_{21}$  becomes very small. For this reason, the FIR-induced photocurrent of (4.16) without the antenna is much smaller than that with the antenna.

Such efficient optical coupling realized by the integration with the LSA enables the bridging of the optical field vector at the nanoscale. Thus, the bridged optical field vector has been indirectly demonstrated using electrical measurements as secondary data. Therefore, this comprehensive experimental evidence concludes that the NF amplitude

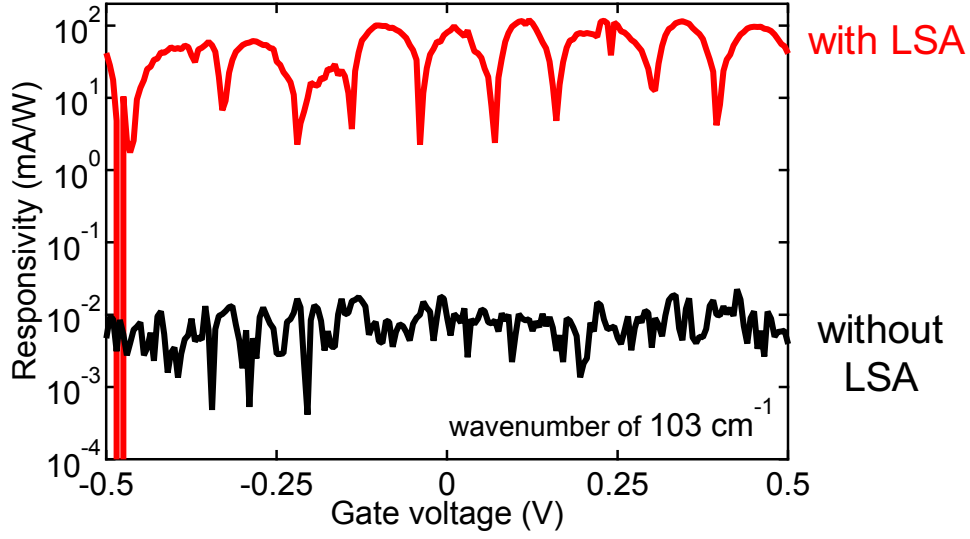


**Figure 4.10:** Comparison of the responsivities of the coupled/non-coupled QD with the LSA.

and phase correspond to the optical-field vector.

#### 4.3.4 contribution of the QD on the optical response of the LSA

Generally, the optical responses of the antenna are highly sensitive to small environmental changes at the gap[69, 85–87]. Hence, the presence of the QD in the bow-tie part at the center could potentially influence the formation of the bridged optical field, even though electrical experiments clearly demonstrate the confined optical field vector. More specifically, the QD connects to the bow-tie part of the LSA, which may disrupt the coherence of the optical field across different frequency components. Since such a modification could lead to incorrect conclusions, the impact of the QD's presence on the optical field is investigated in this section. Here, I examine how coupling with a tiny QD-like connection at the center affects the bridged electric field vector using s-SNOM.

In essence, I utilized the same bow-tie antenna as shown in Fig. 3.10 in Chapter 2 and compared it with a modified version featuring a metallic dot intendedly remaining at the center, as illustrated in Fig. 4.11.

The NF phase ( $\varphi_2$ ) images of the connected/non-connected bow-tie antennas are depicted in Fig. 4.12, with an irradiation wavenumber of  $9.3 \mu\text{m}$ . Surprisingly, despite the presence of the remaining metallic dot, the NF-phase image reveals that the metallic dot has a minimal impact on the NF phase. For a more detailed analysis, line profiles are plotted across their centers in Fig. 4.12(b)(d). In the case of the bow-tie antenna with a gap, I observe a NF phase change of  $0.168 \pm 0.008$  rad, while for the bow-tie antenna with the metallic dot, the NF phase change is  $0.212 \pm 0.011$  rad. Hence, it's evident that the

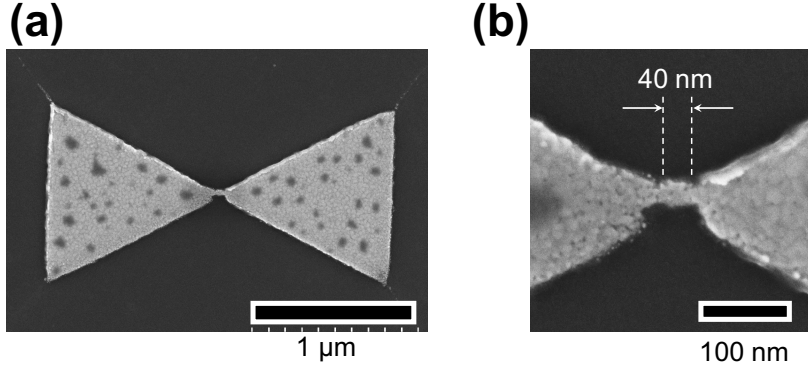


**Figure 4.11:** SEM images of the connected bow-tie antenna.

tiny remaining metallic dot does not significantly affect the NF phase behavior.

The relative size of the QD compared to the LSA is approximately  $10^3$  times larger than that integrated with the LSA designed for the FIR region. This means that the impact of the Si QD is even smaller compared to what the s-SNOM results suggest. Therefore, the integration of the Si QD within the LSA does not significantly influence the bridged optical field vector, further supporting the experimental results obtained through electrical measurements.

#### 4.4 Conclusion of Chapter 4

In conclusion, the investigation of the confined optical field vector was carried out through the electrical responses of a Si QD positioned at the center of the LSA. The strong photocurrents observed from the LSA-coupled QD, along with control experiments to confirm the influence of the LSA, provided compelling evidence for the existence and orientation of the confined optical field vector as deduced from the electrical responses, marking a significant achievement in probing the NF by experimental means. This unique approach of employing electrical measurements to compare and verify optical results provides a new proposal for investigating the NF at the nanoscale. “

If you have any more text to revise or further questions, please feel free to ask!

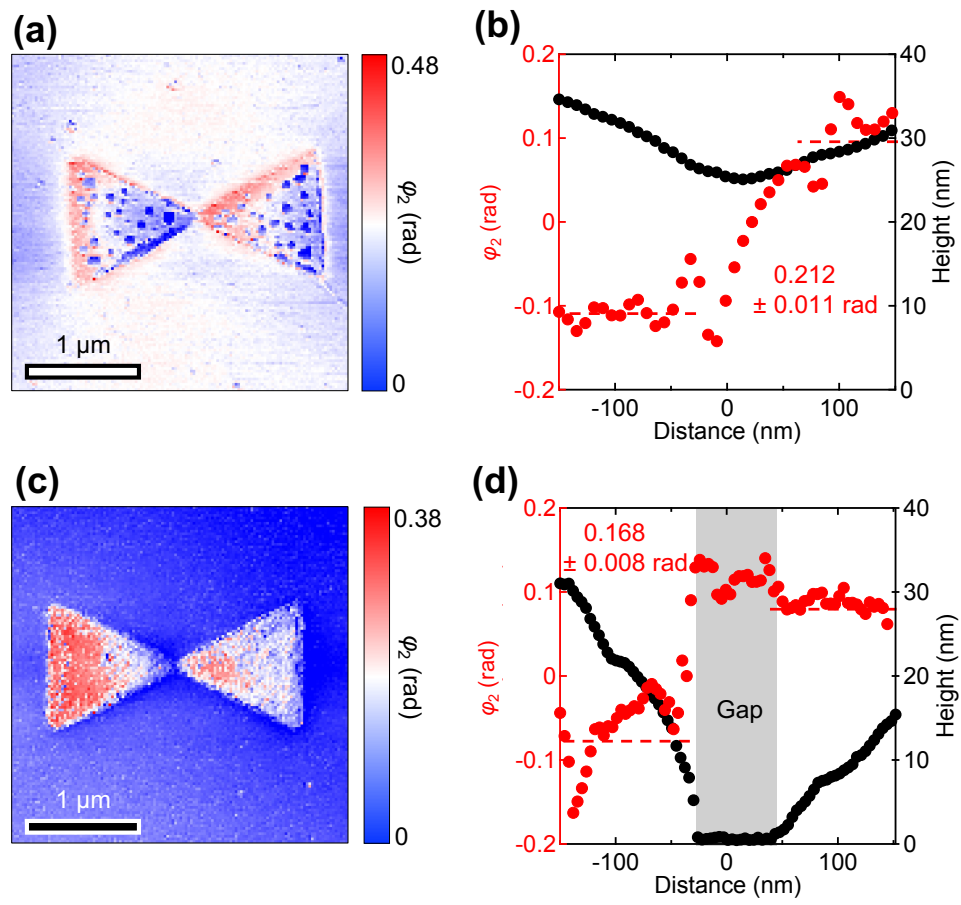


**Figure 4.12:** (a,b) NF phase images (a) and line profile (b) for connected bow-tie antenna (shown in Fig. 4.11).



## Chapter 5

# Vectorial nature of an s-SNOM

In this chapter, a comprehensive experimental investigation of the vectorial properties of NFs in s-SNOM is conducted. The primary focus is on assessing the optical coupling efficiency of host materials, particularly in relation to phenomena such as absorption and radiation. Given that the IR light used in this study corresponds to the energy associated with molecular vibration transitions, the NF status is expected to be influenced by the molecular orientation of the host materials. Polyhydroxybutyrate spherulites (PHB) are employed as the host material for this investigation due to their structural anisotropy, characterized by spatially and periodically twisted higher-order structures. The experimental results reveal that the NF light on the tip apex is predominantly polarized in the out-of-plane direction, aligning with the tip axis. This observation is made through a comparison with topography and far-field spectroscopic results. The findings presented here open up possibilities for selective nanoscale polarimetry and raise intriguing questions about the feasibility of in-plane vectorial NF measurements.

### 5.1 Introduction & Concept

In optical measurements, the polarization of light plays a critical role in determining which information is being probed. Specifically, in the context of s-SNOM, the results are significantly influenced by the polarization of the localized NFs on the tip apex, making a detailed understanding of this polarization essential.

Typically, when the radius of curvature of the AFM tip (around 10 nm in this study) is much smaller than the wavelength of the incident light, a local surface plasmon polariton polarized along the tip axis (the  $z$ -direction) is known to appear due to the elongated shape of the tip. This theoretical interpretation suggests that s-SNOM selectively probes



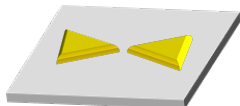
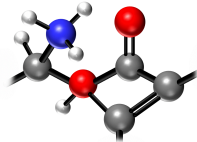
the optical response of the host material projected along the  $z$ -axis. However, there have been reports indicating the presence of residual NF polarization perpendicular to the tip axis (in the  $x-y$  plane) due to depolarization effects or unknown scattering characteristics of the AFM tip. As a result, the actual polarization status of NFs on an AFM-tip apex has remained uncertain, prompting the need for experimental determination.

Accessing the NF polarization experimentally can be challenging due to the closed loop of electric/magnetic forces characterizing the NF. One approach is to couple the NF with the surface optical vector field of optical devices, as discussed in Chapter 3. While this approach offers a strong optical signal (high SNR), it can exhibit strong variations on sub-wavelength scales and be influenced by external factors such as the direction of irradiation and the AFM tip itself. Additionally, obtaining secondary data to support s-SNOM results can be difficult, making quantitative analysis challenging.

Another approach involves vibrational spectroscopy of host materials, offering potential advantages over the former method. IR light, with photon energies corresponding to the excitation energy of molecular vibration transitions, can directly reveal structural information, including chemical bonding, molecular orientation, and higher-order structures [11, 16]. Thus, experimental investigation of NF polarization can be approached through the selection of host materials with well-known structural information. Moreover, the extensive and mature IR database allows for a robust analysis of the polarization components in s-SNOM with confidence. This strategy forms the basis for the experimental investigation of NF polarization in s-SNOM, as presented in this study.

In this work, I conducted an experimental investigation of NF light polarization using banded polyhydroxybutyrate (PHB) spherulites. These polymeric spherulites possess a multiscale structure with mesoscale layered crystals that radially twist from the spherulite nucleus at the micrometer scale. Within the microscale structural layer of this material, where lamellar crystals consist of regularly repeating molecular chain conformations, it becomes possible to explore whether NF light is primarily polarized along the  $z$ -axis by examining the optical coupling efficiency of host materials, specifically through absorption. Therefore, the polarization of NFs can be experimentally explored by studying the spatial dependence of the torsional structure of lamellar crystals.

Furthermore, the lower multiscale structures within the mesoscale structural layer, including the separation of the amorphous and conformed layers, provide additional experimental evidence related to the orientational order of molecular chains. This structural feature offers a suitable platform to investigate the polarization of NFs in s-SNOM.

(a)	Optical devices	Molecular vibration
		
targets	optical-vector field	moment transition of molecular
Spatial dependence	complicated	<b>Distribution of atoms (determined)</b>
Secondary data	Difficult to gain (e.g. Part 4)	<b>Well-known</b> (e.g. structural info. FTIR database)
impacts of external environment	influenced	<b>Robust</b>
Phenomena (SNR)	Radiation ( <b>High</b> )	Absorption (Low)

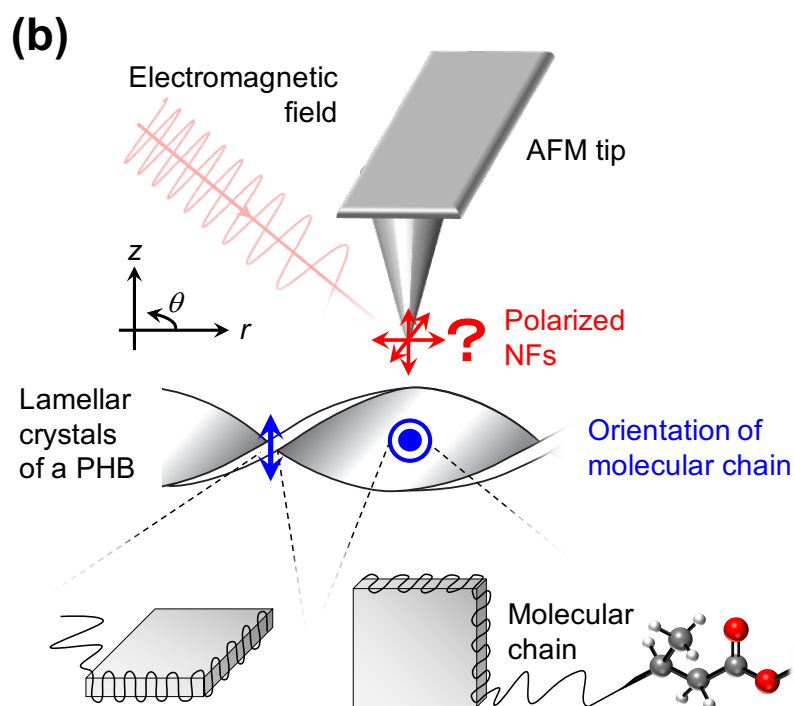


**Figure 5.1:** The concept of this part. (a) Comparison of the feature for investigating the vectorial nature of the NFs. (b) Illustration of the concept for clarifying the vectorial nature of the NFs.

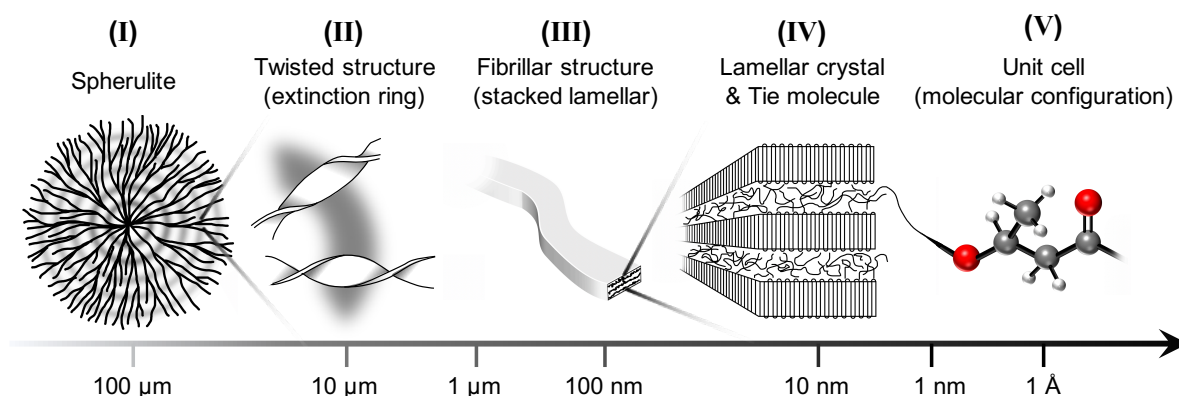


**Figure 5.2:** Hierarchical structures formed in banded PHB spherulites.

## 5.2 PHB spherulites

### 5.2.1 Properties

In general, spherulites are spherical semi-crystals commonly found in unbranched linear polymers in polymer physics. Polymeric spherulites require a specific perspective distinct from low-molecular-weight materials because they possess numerous degrees of freedom in the primary structure of polymers, including molecular weight, distribution, and branching structures, in addition to the chemical structure of repetitive units. As an example, Fig. 5.2 shows hierarchical structures ranging from the macro- to Å-scale of the banded PHB spherulite. The fundamental element in these hierarchical structures is the lamellar crystal represented as (VI) in Fig. 5.2. Such a unique structure results in birefringence properties, leading to a variety of optical phenomena.

PHB spherulites exhibit a distinctive optical response known as a cross pattern, sometimes referred to as the Maltese cross, when observed under a polarizing microscope. Especially when viewed with a cross-Nicole configuration, these patterns manifest in a variety of colors. This striking phenomenon arises due to the polarizing nature of the lamellar crystals within the spherulites, which are radially arranged from the spherulite's center in a fibrillar structure, as depicted in (III) in Fig. 5.2. Furthermore, owing to the birefringence property of the lamellar crystals, spherulites exhibit coloration due to retardation when observed through a cross-Nicole light microscope. Another distinctive optical feature is the presence of ring patterns known as extinction rings, as illustrated in (II) in Fig. 5.2.

## 5.3 Method

### 5.3.1 s-SNOM

The s-SNOM measurements mainly followed the setup described in section 2.2.2 in chapter 2. The nanoscale IR response of PHB spherulites is discussed in this study primarily using a local absorbance  $a_n(\nu) = \Im[\sigma_n(\mu)]$ , where  $n = 2$  throughout this work. Since the SNR is smaller than the LSA (as shown in chapter 3) due to the poorly resonant properties of the s-SNOM, the accumulation time for each pixel was set to 15 ms.

The nanoscale IR response of PHB spherulites is discussed in this study primarily using a local absorbance  $a_n(\nu) = \Im[\sigma_n(\mu)]$ , where  $n = 2$  throughout this work.

Through the extensive IR database, the vibration mode can be selected using the laser available. Fig. 5.3(a) displays the FF spectrum of the PHB spherulite, exhibiting numerous resonant peaks. The bonding assignment has already been reported as shown in Fig. 5.3(b) [11]. This wealth of information is a strong advantage when studying organic materials with s-SNOM.

The inset in Fig. 5.3(a) covers the approximate spectrum range accessible using a CO<sub>2</sub> gas laser. There are two peaks of C-C backbone mode and  $\nu(\text{C-O})$  mode at approximately 980 and 1050  $\text{cm}^{-1}$ , respectively. Additionally, the bonding alignment is parallel and perpendicular to the molecular chain orientation, which strongly influences the absorption phenomena. Therefore, these two bonding modes are primarily utilized in this study.

### 5.3.2 Fabrication

The PHB samples utilized in this study were synthesized by Prof. Junko Morikawa<sup>1</sup> and Dr. Ryu Meguya<sup>2</sup>. The banded PHB spherulite employed in this study is depicted in Fig. 5.3.2(a) (visible light image).

After being melted at 250 °C, PHB (Sigma-Aldrich Co. LLC) was crystallized at 75~90 °C, placed between the CaF<sub>2</sub> substrate and Au-coated glass substrates. The resulting PHB was positioned on the CaF<sub>2</sub>, a transparent substrate for the MIR regions. This choice of CaF<sub>2</sub> was made to avoid disturbing the NF, as analyzed by the dynamic approach curve in chapter 2, since it is not a resonant substrate like Au.

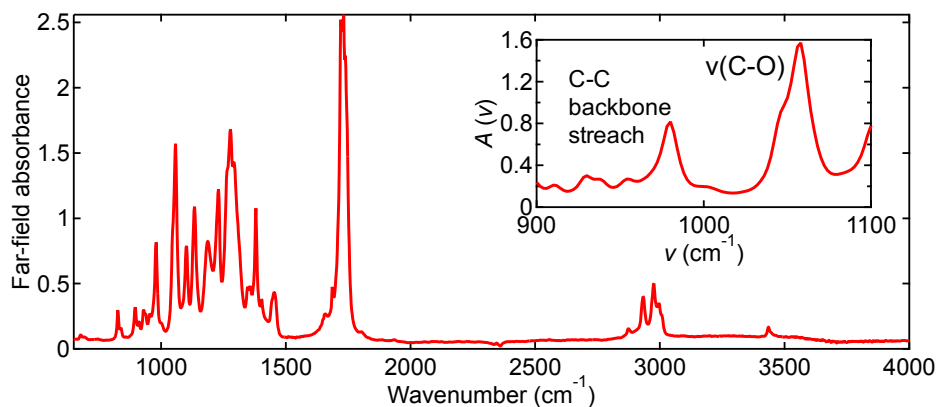
A close-up of the center of the banded PHB spherulite is presented in Fig. 5.3.2(b), where a periodic extinction ring characteristic of the banded structure is observable. In the polarization microscopic image in Fig. 5.3.2(c), one can observe not only the Maltese crosses characteristic of spherulite but also the periodic coloring due to retardation.

Fig. 5.3.2(d) displays the RGB values of the line profile, extracted using the yellow dotted line in the inset. Since the R-value effectively reflects the band structure, I esti-

<sup>1</sup>Department of Materials Science and Engineering, Tokyo Institute of Technology, Tokyo, Japan

<sup>2</sup>National Institute of Advanced Industrial Science and Technology, Tsukuba, Ibaraki, Japan

(a)



(b)

wavenumber / $\text{cm}^{-1}$	assignment	dichroism
896	C-C backbone stretching region correlating to the formation of the $2_1$ helix structure of PHB chain	parallel
910		parallel
930		perpendicular
938		parallel
954		parallel
980		parallel
1058	$\nu(\text{C-O})$	perpendicular
1102	$\nu(\text{C-O-C})$	parallel
1134	$\gamma(\text{CH}_3)$ , $\nu_s(\text{C-O-C})$	parallel
1230	$\nu(\text{C-O-C})$	parallel
1380	$\delta_s(\text{CH}_3)$ , $\delta_s(\text{CH})$	parallel
1404	—	parallel
1686	$\nu(\text{C=O})(?)$	perpendicular
2932	$\nu_{\text{as}}(\text{CH}_2)$	parallel
2974	$\nu_{\text{as}}(\text{CH}_3)$	perpendicular

**Figure 5.3:** (a)FF spectrum of the PHB spherulite. (b)Bonding assignment of the PHB spherulite in the IR region. Reprinted table with permission from Ref. [11]. Copyright 2013, American Chemical Society.

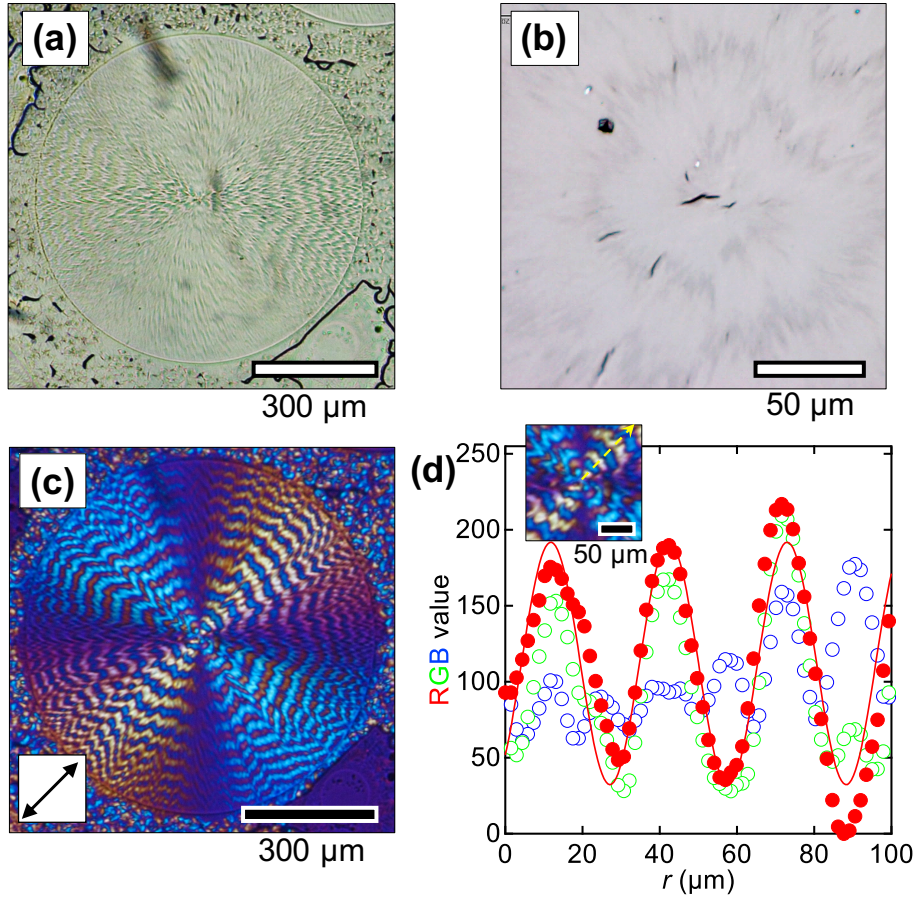


**Figure 5.4:** Visible light images of the banded PHB spherulite employed in this study: (a) Non-polarized optical image of the entire region. (b) Close-up image of the center. (c) Polarized optical microscopy image, with the polarization of irradiation indicated by a black arrow. (d) The radial dependence of the RGB value, with the line profile extracted around the center (as shown in the inset). The red solid curve represents the result of sinusoidal fitting.

mated the period of the twisted lamellar  $T_{\text{vis}} = 30.6 \pm 0.2 \mu\text{m}$  via fitting the sinusoidal curve.

For control experiments involving twisted structures, I prepared the non-banded PHB spherulite as depicted in Fig. 5.5. Fig. 5.5(a) and 5.5(b) confirm the absence of extinction rings, indicating the absence of twisted structures. The polarization microscopic image in Fig. 5.5(c) also shows no extinction rings, although Maltese crosses are clearly visible. Therefore, this non-banded-PHB sample is suitable for control experiments involving twisted structures.

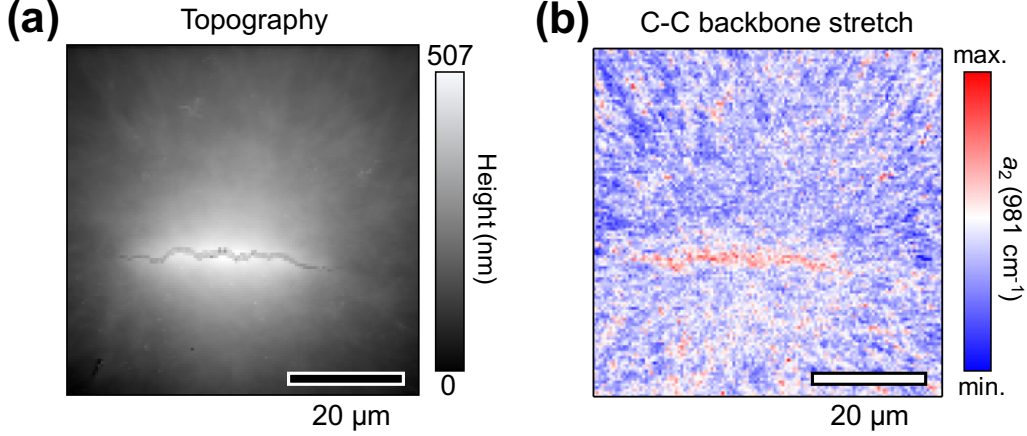


**Figure 5.5:** Visible light images of the non-banded PHB spherulite used in this work. (a) Unpolarized-optical image of the whole region. (b) Closed image in the center. (c) Polarised-optical microscopy image, where the polarization of irradiation is indicated by a black arrow.

## 5.4 Experimental results

### 5.4.1 Twisted structure

The schematic of the experimental setup is roughly shown in Fig. 5.6(a), where the coordinate axes are defined in cylindrical coordinates with  $r$ ,  $\theta$ , and  $z$ . Such  $z$ -directional polarized NF optically interacts with a banded PHB spherulite and generates scattered FF light to visualize the spatially resolved structural information of lamellar structures composed of molecular chains repeated in regular conformation at the nanoscale (shown in Fig. 5.1(b)).

Fig. 5.6(b) presents the topography of the banded PHB spherulite in the scanned region by the s-SNOM. The torsionally uneven surface of the lamellar crystals observed in Fig. 5.3.2 can also be seen in the topography; the convex and concave parts correspond to the upright and sideways orientations of the lamellar crystals, respectively (see Fig. 5.1).

The most significant experimental results are displayed in Fig. 5.6(c); these IR images were recorded on resonance with the C-C backbone stretching mode at  $981 \text{ cm}^{-1}$ ,  $\nu(\text{C-O})$  mode at  $1054 \text{ cm}^{-1}$ , and off-resonance mode at  $946 \text{ cm}^{-1}$ . The  $r$ -directional periodic changes in the  $a_2(\nu)$  images at  $981$  and  $1054 \text{ cm}^{-1}$  demonstrate the structural information of the twisted lamellae. In contrast, the vanishing contrast at the off-resonance of  $1038 \text{ cm}^{-1}$  indicates that the  $a_2(\nu)$  is derived from the effects of artifacts.

For comparison between the topography and  $a_2(\nu)$  images, I extracted results surrounded by the yellow dashed region in Fig. 5.6(b) to (d). The  $a_2(981 \text{ cm}^{-1})$  and  $a_2(1054 \text{ cm}^{-1})$  images show sinusoidal responses and are positively and negatively correlated with the topography, respectively. To clarify, the  $r$ -dependence is shown by ex-



	$T_{\text{vis,NF,FF}} (\mu\text{m})$	$\beta_{\text{NF}} - \beta_{\text{topo}} (\text{deg.})$
Visible	$30.6 \pm 0.2$	-
AFM topography	$23.3 \pm 0.5$	0
$a_2 (981 \text{ cm}^{-1})$	$25.4 \pm 0.6$	$192.03 \pm 12.75$
$a_2 (1054 \text{ cm}^{-1})$	$24.0 \pm 0.6$	$9.22 \pm 15.03$
$A_t (981 \text{ cm}^{-1})$	22 to 33	-

**Table 5.1:** Comparison of the period of the twisted structure  $T_{\text{vis,NF,FF}}(\nu)$  and spatial phase  $\beta_{\text{NF}}(\nu) - \beta_{\text{topo}}$ .

tracting the line profiles described as the yellow dotted arrows (Fig. 5.6(e)).

The values of  $T_{\text{topo}}$  and  $T_{\text{NF}}(\nu)$  obtained by sinusoidal fitting, described by solid curves, and the spatial phase based on topography  $\beta_{\text{NF}}(981\text{cm}^{-1}) - \beta_{\text{NF}}(1054\text{cm}^{-1})$ , are summarized in Table 5.1. The values of  $T_{\text{topo}}$  and  $T_{\text{NF}}(\nu)$  agree well with that of  $T_{\text{vis}}$ , experimentally demonstrating that monochromatic NF techniques in the IR region enable optical reconstruction of the higher-order structure of the twisted lamellar crystals.

For the spatial phase,  $\beta_{\text{NF}}(1054\text{cm}^{-1})$  and  $\beta_{\text{topo}}$  have almost the same phase, approximately  $0^\circ$ , whereas  $\beta_{\text{NF}}(981\text{cm}^{-1})$  and  $\beta_{\text{topo}}$  (and  $\beta_{\text{NF}}(1054\text{cm}^{-1})$ ) have a reverse phase, approximately  $180^\circ$ . This phase relation indicates that the structural information of the twisted lamellar crystals is encoded by the transition moment of the molecular chains. Specifically, considering the relationship between the lamellar crystals and the molecular chains (shown in the lower panel of Fig. 5.6(d)), the C-C backbone stretching and  $\nu(\text{C-O})$  mode correspond to the perpendicular and parallel vibration modes to the molecular chain, which corresponds to  $\beta_{\text{NF}}(981\text{cm}^{-1}) - \beta_{\text{NF}}(1054\text{cm}^{-1}) \sim 180^\circ$ . For the topography, because lamellar crystals are composed of molecular chains oriented perpendicular to the in-plane direction of lamellar crystals (shown in Fig. 5.1),  $\beta_{\text{topo}} - \beta_{\text{NF}}(1054\text{cm}^{-1})$  is equal to  $\sim 0^\circ$ .

Fig. 5.6(f) displays the polar plot of  $\theta$  dependence of the  $r$ -directional averaged  $\overline{a_2(\nu)} \equiv \int_0^R A_t(\nu) dr / \int_0^R dr$ , where  $R$  is the radius of the banded PHB spherulite. As clearly shown in Fig. 5.6(c), there is no significant  $\theta$  dependence; this result suggests that the s-SNOM does not efficiently couple with the in-plane optical response of host materials. This in-plane vectorial nature is also discussed by FF imaging in the next section.

The sinusoidal behavior of the banded PHB spherulite is unable to be observed in the  $a_2(981\text{cm}^{-1})$  image of the non-banded sample, as shown in Fig. 5.7. This result further supports the fact that  $a_2(\nu)$  images of banded PHB spherulite reflect the structural information of twisted lamellar crystals.



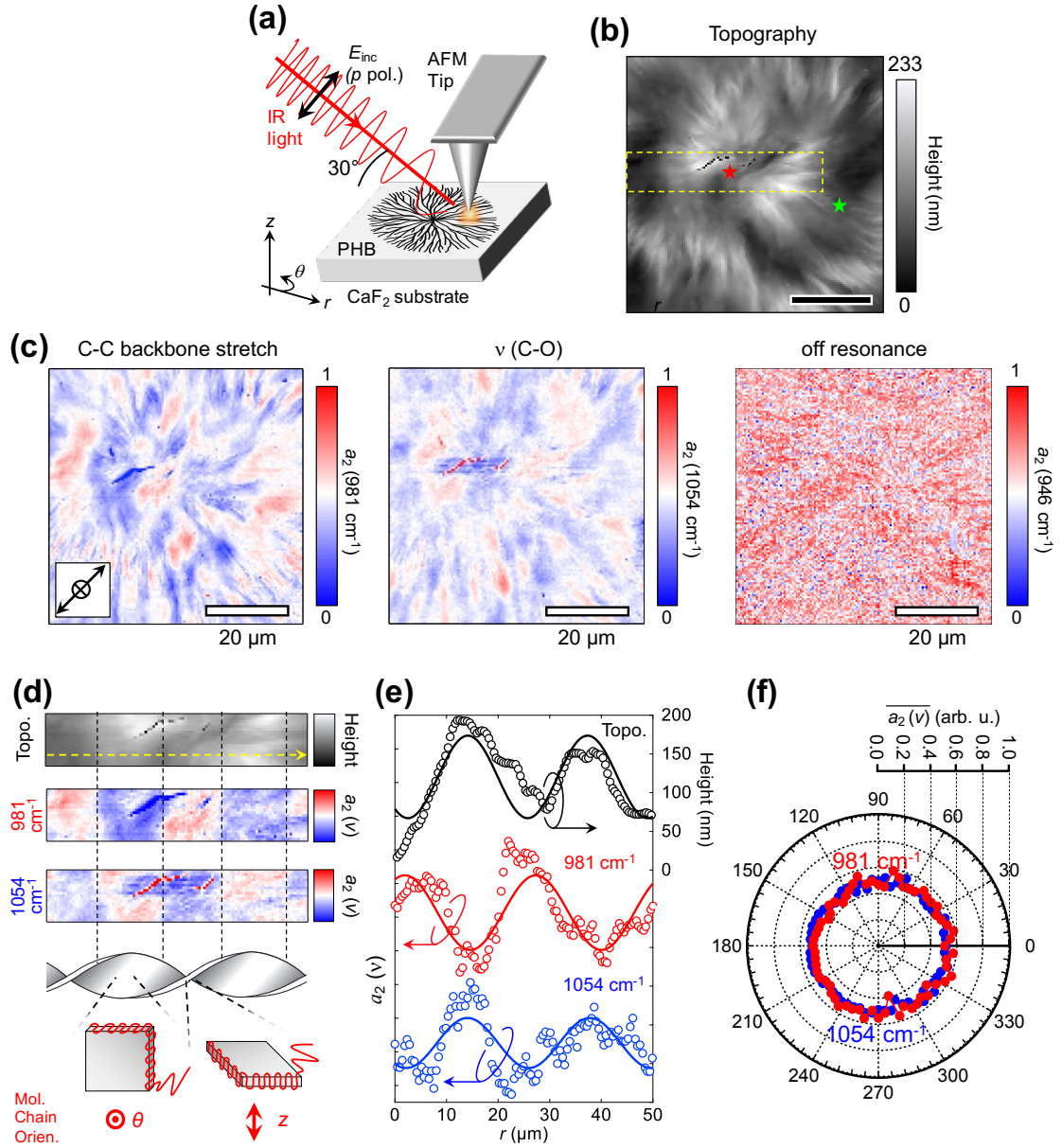


**Figure 5.6:** Monochromatic NF IR measurements. (a) Schematic diagram of the s-SNOM measurements. (b) Topography of the banded PHB spherulite. (c) NF absorbance images at the C-C backbone stretch mode at  $981 \text{ cm}^{-1}$ ,  $\nu(\text{C-O})$  mode at  $1054 \text{ cm}^{-1}$ , and off-resonance at  $945 \text{ cm}^{-1}$ . The black arrow indicates the polarisation of the IR irradiation. These images were taken at  $128 \times 128$  pixels. (d) Comparison of topography and NF images extracted from the region marked by the yellow dotted box in (b). (e) The line profiles shown below were taken from the yellow dotted arrows in (d), where solid lines are sinusoidal fitting results. (f) polar plot of  $\overline{a_2(\nu)}$

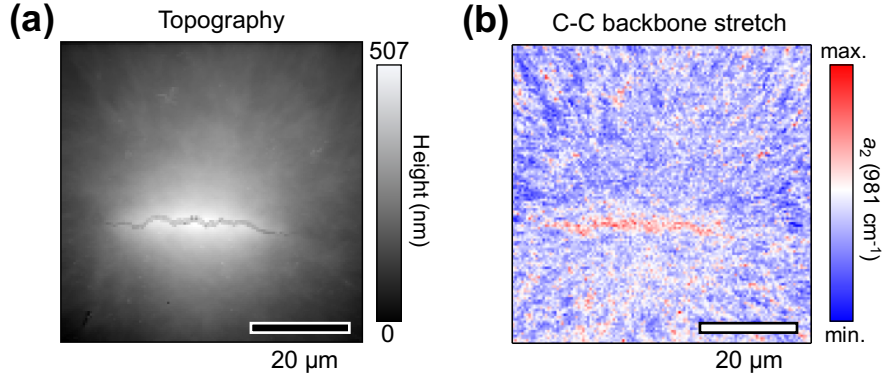


**Figure 5.7:** (a) Topography of the non-banded PHB spherulite. (b) NF absorbance image of the non-banded PHB spherulite at  $981 \text{ cm}^{-1}$ .

### Far-field investigation

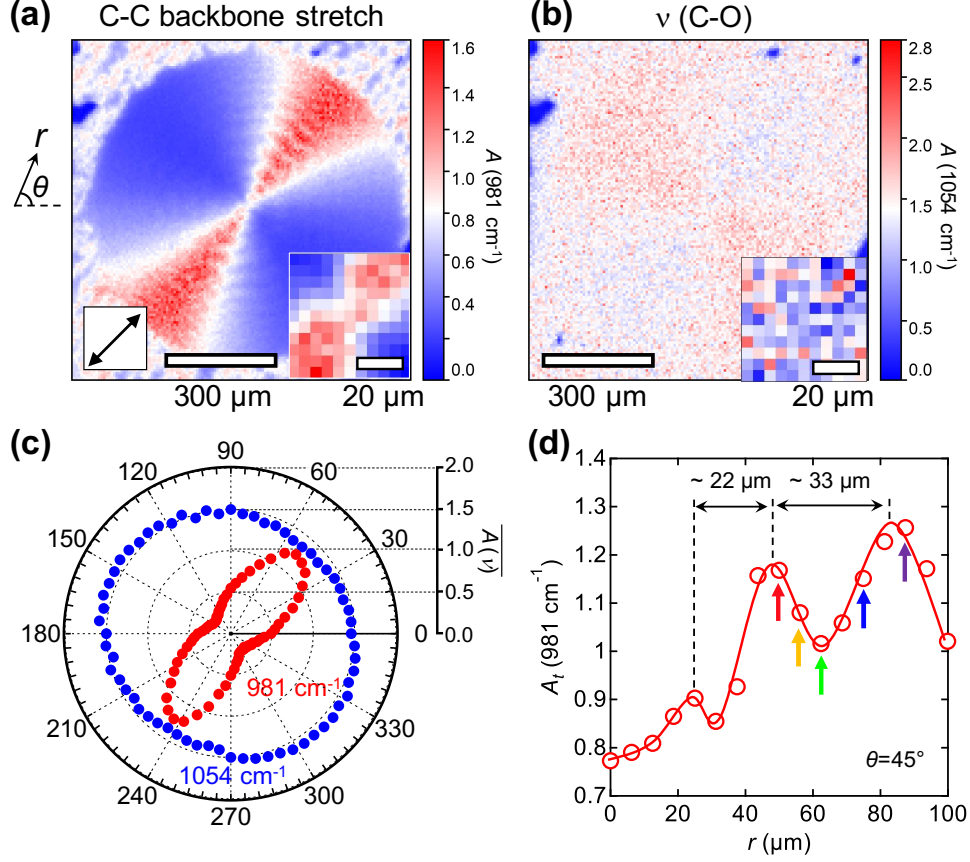
To discuss the monochromatic NF results from the secondary data, I compared NF and FF IR images. All FF images are represented by the transmission absorbance  $A_t(\nu) = -\log(I_t(\nu)/I_{\text{inc}}(\nu))$ , where  $I_t(\nu)$  and  $I_{\text{inc}}(\nu)$  denote the power transmitted through the banded PHB sample and the incident power, respectively. The FF IR images consist of several hundreds of IR spectra with spatial resolution.

Fig. 5.8 displays FF IR images recorded in resonance with the C-C backbone stretching mode at  $981 \text{ cm}^{-1}$  and  $\nu(\text{C-O})$  mode at  $1054 \text{ cm}^{-1}$ . The inset provides the same spatial scale as scanned by the s-SNOM, highlighting the superior spatial resolution of s-SNOM measurements over FF measurements.

In the  $A_t(\nu)$  images, both a Maltese cross and an  $r$ -dependent periodic pattern are observed, resembling the results in Fig. 5.3.2(d). This polarization dependence reflects in-plane ( $r - \theta$  plane) momentum transitions of the molecular chains. In comparison with the NF results, no Maltese crosses were observed in the  $a_2(\nu)$  images. This difference arises because the  $z$ -polarized NF of s-SNOM hardly optically couples with the in-plane momentum transition.

Fig. 5.8(c) presents a polar plot of the  $\theta$  dependence of the  $r$ -directional averaged  $\overline{A_t(\nu)} \equiv \int_0^R A_t(\nu) dr / \int_0^R dr$ , where  $R$  is the radius of the banded PHB spherulite. The distribution of the Maltese crosses exhibits an inverse  $\theta$  dependence for the C-C backbone stretching and  $\nu(\text{C-O})$  mode, although  $\overline{A_t(1054 \text{ cm}^{-1})}$  reveals a small contrast. This inversion indicates that their momentum transitions are orthogonal to each other, and the orthogonal phase relation obtained in the NF is experimentally demonstrated in the FF measurements as well.

To obtain structural information about the lamellar crystal, the  $r$ -dependence of  $A_t(\nu)$  is plotted at  $981 \text{ cm}^{-1}$ , and the line profile is extracted from the yellow dotted arrows in



**Figure 5.8:** Far-field IR images. (a,b) Maps of  $A_t(\nu)$  recorded while exciting the C-C backbone stretch mode at  $981 \text{ cm}^{-1}$  (a) and  $\nu(\text{C-O})$  mode at  $1054 \text{ cm}^{-1}$  (b). (c) Polar plot of  $\theta$  dependence of  $A_t(\nu)$ . (d)  $r$  dependence of  $A_t(\nu)$  at  $\theta = 45^\circ$ , which is extracted by the line profile of the yellow dashed arrow described in the inset image. The red trace guides your eyes.

the inset. Although the  $r$ -dependence of  $A_t(\nu)$  is subject to diffraction and reproduces sinusoidal behavior compared to the  $a_2(\nu)$  images, the period gained by FF  $T_{\text{FF}}(981 \text{ cm}^{-1})$  is estimated to be roughly  $22\text{--}33 \text{ }\mu\text{m}$ , which aligns well with  $T_{\text{vis}}$ ,  $T_{\text{topo}}$ , and  $T_{\text{NF}}(\nu)$ .

Through the momentum transition of the molecular chain, the local maximum and minimum values of  $A_t(981 \text{ cm}^{-1})$  can be assigned to be the ridge and valley of the banded PHB spherulite, respectively. In contrast, the  $A_t(\nu)$  image at  $1054 \text{ cm}^{-1}$  lacks sufficient contrast and cannot be used to estimate  $T_{\text{far}}(\nu)$ .

#### 5.4.2 Fibrillar structure

To further illustrate the vectorial nature of the s-SNOM, I have examined the lower-scale structure of the fibrillar pattern (classified as (III) in Fig. 5.2) with ultra-high spatial resolution. Fig. 5.9(a) presents ultra-close-up NF IR images at  $981 \text{ cm}^{-1}$  of the area indicated by the green star in Fig. 5.6(b). A fibrillar pattern, spanning less than  $100$

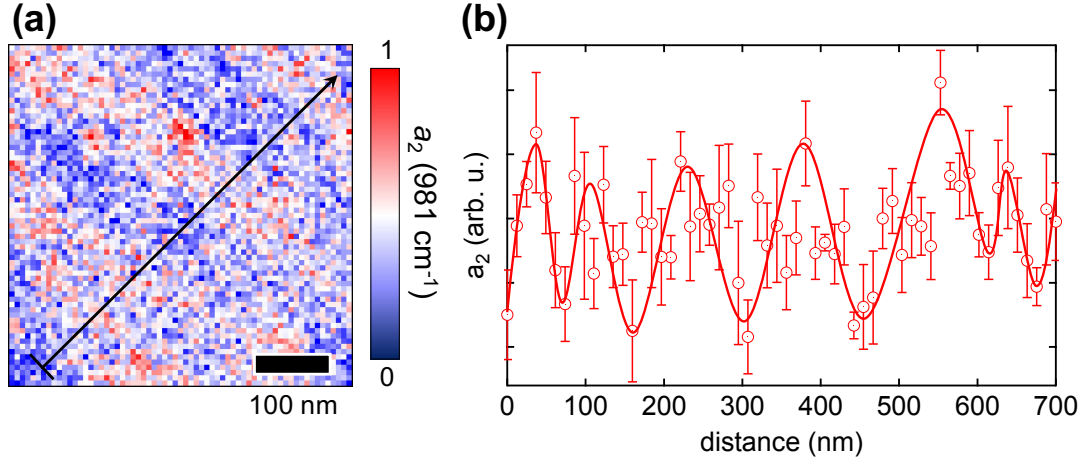


**Figure 5.9:** Mesoscale NF IR images of the banded PHB spherulite (corresponding to the scale of (III) in Fig. 5.2). (a) NF IR images at the region indicated by the red star in Fig. 3(d). The acquired pixels are  $64 \times 64$  pixels. (b) The line profiles were extracted from the black arrow with a 5-pixel thickness in (a). The solid trace serves as a guide.

nm along the radial direction ( $r$ -direction), is clearly observable, as shown in Fig. 5.9(b). Such a mesoscale pattern has been previously reported, indicating that the NF images can effectively distinguish between the fibrillar structure and the amorphous region of the PHB spherulite.

To validate this hypothesis, I conducted selective etching to exclusively remove the amorphous region. To distinguish between amorphous and fibrillar structures, I crosslinked the amorphous regions by staining with ruthenium tetroxide and introduced metals [88] to enhance etching resistance. Following this process, plasma etching was carried out under atmospheric conditions to etch away the amorphous regions. The resulting PHB was coated with osmium to a thickness of approximately 5 nm using vapor deposition (Neoc-Pro, Meiwafoysis Co., Ltd.) to prevent charging during scanning electron microscopy (SEM) measurements (JSM-7500F, JEOL Ltd.). SEM observations were conducted at an accelerating voltage of 3 kV, with the samples affixed to conductive carbon tapes.

The SEM image of the etched PHB spherulite is displayed in Fig. 5.10, captured near the region where the NF imaging was conducted. The radial orientation and thickness of the remaining fibrillar structure closely match those observed in the NF image, although slight underestimation of thickness may have occurred due to over-etching during the etching process.

It's important to note that the SEM setup, including parameters like acceleration voltage and the presence of covering metals, did not reveal the single lamellar crystals depicted as (IV) in Fig. 5.2. However, the mesoscale NF images effectively demonstrated the vertical polarization of the NF and allowed differentiation between the amorphous and well-structured regions of the fibrillar structure.

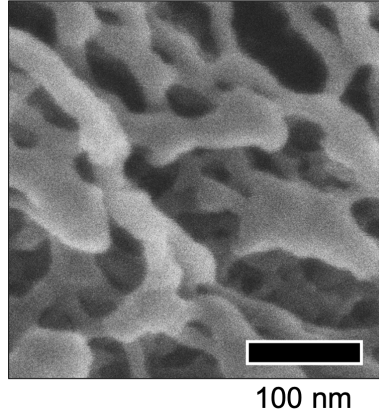


**Figure 5.10:** SEM images of the selectively-etched banded PHB spherulite.

## 5.5 Conclusion of Chapter 5

In conclusion, I evaluated the polarization of NFs on the tip apex by measuring the absorption images and spectroscopies of the PHB spherulites. Through a comparison with the topography, FF visible and IR images, and chemical bonding assignments, the polarization of NF has been demonstrated to be predominantly out-of-plane ( $z$ -direction), thereby confirming the quantitative strategy of our polarization assessment.

This unique  $z$ -directional polarization enables the measurement of out-of-plane optical responses of host materials, which is challenging to achieve using transverse light. Additionally, this nature of NFs provides advantages in terms of spatial resolution compared to conventional  $z$ -axis measurements using radial polarization [89, 90].

The revealed polarization of NF light not only offers structural insights into host materials, such as organic or anisotropic materials demonstrated in this chapter but also facilitates the quantitative interpretation of s-SNOM images, including the visualization of the optical field vector.

## Chapter 6

# Nanoscale visualization of in-plane optical-field vector

In this chapter, I address the intriguing question raised in the preceding chapters: whether it is feasible to conduct in-plane vectorial NF measurements. Leveraging the optical setup flexibility of the Michelson interferometer and the linearity of the wave equation of light, I have successfully probed weak NF signals with in-plane polarization.

### 6.1 Introduction & Concept

The s-SNOM has revealed the vectorial nature of NF measurements, indicating that the NF is polarized out-of-plane and selectively couples with the vector field perpendicular to the sample surface [91]. This unique characteristic sets s-SNOM apart from conventional FF optical measurements, which are typically limited to in-plane measurements within a two-dimensional plane. Consequently, the distinctive capability of s-SNOM suggests that if in-plane optical-field vectors can be probed, it becomes possible to reconstruct the three-dimensional optical vector field. This achievement holds the promise of advancing our understanding of optical device properties at the nanoscale, surpassing the limitations imposed by the diffraction limit, and offering a powerful tool for advanced optics development.

Moreover, this technique holds significant potential for diverse research fields, including materials science. For instance, it can be employed to analyze optical axes and orientations in anisotropic materials [11], as well as to probe polarization induced by material rotation. Therefore, there is a natural inclination to pursue the realization of NF in-plane probing techniques.

Several reports have discussed NF in-plane probing techniques using a-SNOM and s-



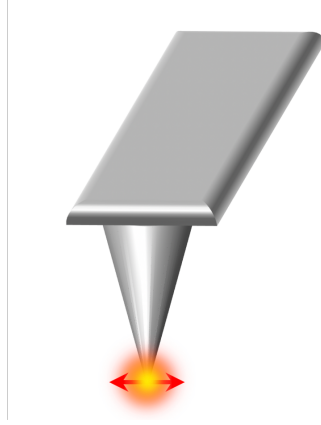


**Figure 6.1:** Illustration of the objective in this chapter.

SNOM. However, these studies typically utilized apertures (in the case of a-SNOM) or AFM tips (in the case of s-SNOM) as local scatterers, rather than using the NF excited on a tip or aperture itself. This approach led to complex optical setups, often requiring illumination from the bottom [69, 71, 92] or the side [93]. Such optical setups introduce limitations on device design, including substrate selection. For example, silicon (Si) substrates, despite being highly reliable and amenable to sophisticated fabrication techniques, are challenging to investigate using these SNOM setups due to their broadband absorption properties (they are transparent only within specific spectral regions, typically between 1666 to 8333  $\text{cm}^{-1}$ ). This disparity impedes the development of optical components. Thus, the preference for using an AFM tip as an in-plane polarized NF source, rather than a mere local scatterer, becomes evident.

In this chapter, the goal is to realize in-plane polarized NF illumination at the apex of an AFM tip as shown in Fig. 6.1 and to challenge the visualization of the optical field vector.

## 6.2 Method

### s-SNOM setup

The s-SNOM measurements closely followed the setup described in section 2.2.2. The wavenumber of irradiation was set to 1075  $\text{cm}^{-1}$ , generated by a  $\text{CO}_2$  gas laser. In polarization-resolved measurements,  $\text{BaF}_2$  holographic wire grid polarizers were employed.

In the experiments aiming to achieve *s*-polarized NFs, a bare Au substrate was utilized due to its high SNR, as demonstrated in Chapter 2. However, to extract *s*-polarized NFs, modifications to the optical path were necessary, which is a primary focus of this chapter. Details regarding these optical setup upgrades will be provided below. Additionally, for the demonstration of in-plane visualization of the optical field vector, a patterned Au

materials (or location)	element size (m)
Air	$\lambda$
Si	$\lambda/2$
Pr	$\lambda/10$
the apex of Pr	$5 \times 10^{-10}$
the apex of Si	$5 \times 10^{-10}$

**Table 6.1:** The mesh condition for the FEM calculation.

substrate fabricated on the Si substrate was used, as described later in this chapter.

### FEM simulation

To study the *s*-polarized NFs, three-dimensional FEM simulations were conducted. Performing calculations in three dimensions involves a significantly increased computational load compared to two dimensions, necessitating various strategies to reduce the computational burden.

One strategy is limiting the size of the simulation volume. The simulation volume was minimized while preserving the AFM tip geometry, consisting of air ( $\epsilon_{\text{air}} = 1$ ) with dimensions of  $10 \times 10 \times 20 \mu\text{m}^3$ . The AFM tip was modeled as a  $15 \mu\text{m}$ -height Si cone coated with an approximately  $20 \text{ nm}$ -thick layer of Pr. The apex of the AFM tip was rounded using a sphere with a radius of curvature of  $20 \text{ nm}$ . This geometry closely resembles the AFM tip used in the experiments presented in Fig. 2.2.

The incident radiation was defined as plane waves with a wavenumber of  $1074 \text{ cm}^{-1}$ , matching the experimental setup. To examine polarization dependence, the plane waves were set to have either *p*- or *s*-polarization. The incident angle was  $30^\circ$  relative to the host material's surface, consistent with the experimental configuration. To prevent reflections at the boundaries of the simulation volume, Perfectly Matched Layers (PML) with a thickness of  $500 \text{ nm}$  were applied to all sides.

Mesh conditions also required optimization to strike a balance between computational efficiency and result accuracy. Multiple simulations were performed to determine suitable mesh sizes. The optimized mesh conditions are summarized in Table 16. The general trends in mesh size, such as dependence on wavelength, align with the description provided in section 2.3.2 of Chapter 2. The PML was meshed using 8 rectangular prisms, and the solve type was set to direct to reduce computational load.



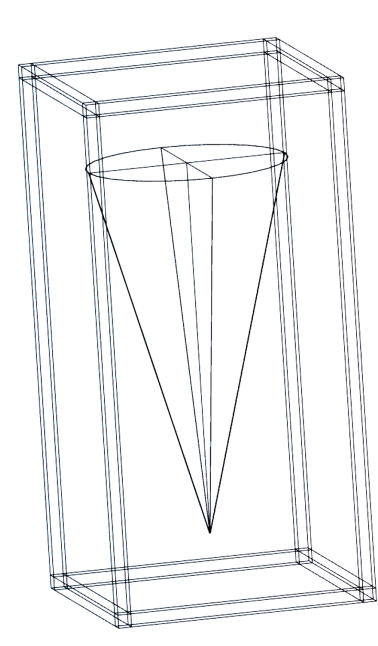


**Figure 6.2:** Simulation model for three-dimensional FEM simulations.

## 6.3 Experimental results and discussion

### 6.3.1 polarization dependence of scattering coefficient

First, the angle dependence of  $s_3$  with respect to the polarization of the incident light was investigated. The polarization of the incident light could be selectively controlled by varying the angle  $\theta_{\text{in}}$  of the polarizer, as depicted in Fig. 6.3(a). As  $\theta_{\text{in}}$  was rotated from 0 (corresponding to  $p$ -polarization) to 90 degrees (corresponding to  $s$ -polarization), the  $s_3$  signal exhibited a significant decrease. This behavior is likely attributed to variations in optical coupling efficiency due to the elongated shape of the AFM tip.

The noteworthy result is that the  $s_3$  signal remained above the noise level. The noise level was determined under the condition in which the AFM tip was retracted from the surface of the sample. This outcome provides evidence that the NFs are indeed excited by  $s$ -polarized incident light.

An alternative mechanism to consider is the enhancement of running irradiance due to standing waves at the sample surface. This phenomenon is often exploited in high-sensitivity reflectance spectroscopy with a small angle  $\theta$ . When IR light is incident on and reflected from a metal substrate, it undergoes phase changes and generates a standing wave on the metal surface. Under  $p$ -polarized light irradiation, the phase changes of the incident and scattered light add up in the out-of-plane direction, resulting in a large standing wave  $2 \cos \theta \times E_{\text{inc}}$ . However, under  $s$ -polarized light irradiation, the phase of the incident and scattered light cancels out, leading to an effective reduction in incident light.

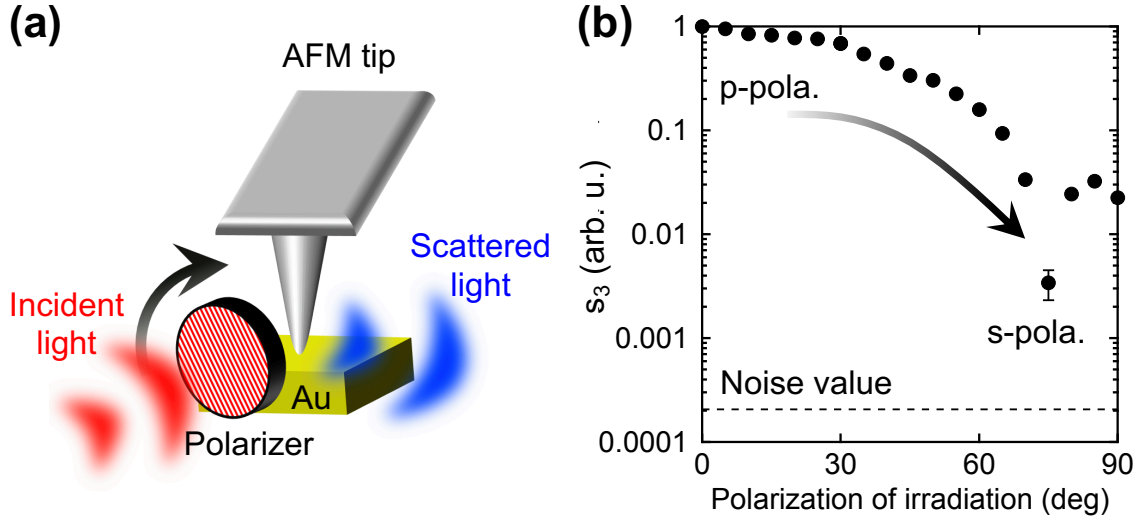


**Figure 6.3:** (a) Illustration of the measurement for the polarization dependence of the scattering coefficient. (b)  $s_3$  versus  $\theta_{\text{in}}$ .

In fact, s-SNOM exhibits a strong tendency for an irradiance angle of 25-35 degrees, while high-sensitivity reflectance spectroscopy primarily uses angles in the range of 15-30 degrees, which aligns well with these observations. It's worth noting that the numerous factors involved, including the geometric effects of the tip and the presence of a mirror dipole in the sample, make it challenging to isolate the contribution of the enhancement of the NF signal due to standing waves under *p*-polarized illumination.

To extract the NFs with *s*-polarization, one solution is to utilize reference light. As previously described in Chapter 2, the scattered light from the tip-sample interface interferes with the reference light and is subsequently detected. Leveraging the linearity of the electromagnetic field, the *s*-polarized scattered light can be strengthened by reference light with *s*-polarization.

Therefore, two possible approaches can be considered: One is setting all irradiation to be *s*-polarized (corresponding to  $\theta_{\text{in}} = 90$  degrees). The other is a modification of the reference light from *p*- to *s*-polarization while keeping the irradiation on the AFM tip as *p*-polarization.

Such an optical setup is feasible due to the flexibility of the Michelson interferometer.

### 6.3.2 Optical setup for in-plane NF probing

To efficiently couple the in-plane components of NFs with the reference light of *s*-polarization, two different optical setups were employed, as illustrated in Fig. 6.6.

The setup depicted in Fig. 6.3(a) had  $\theta_{\text{out}}$  set to 90 degrees, which corresponds to both the polarization of the reference light and the incident light being *s*-polarized. This

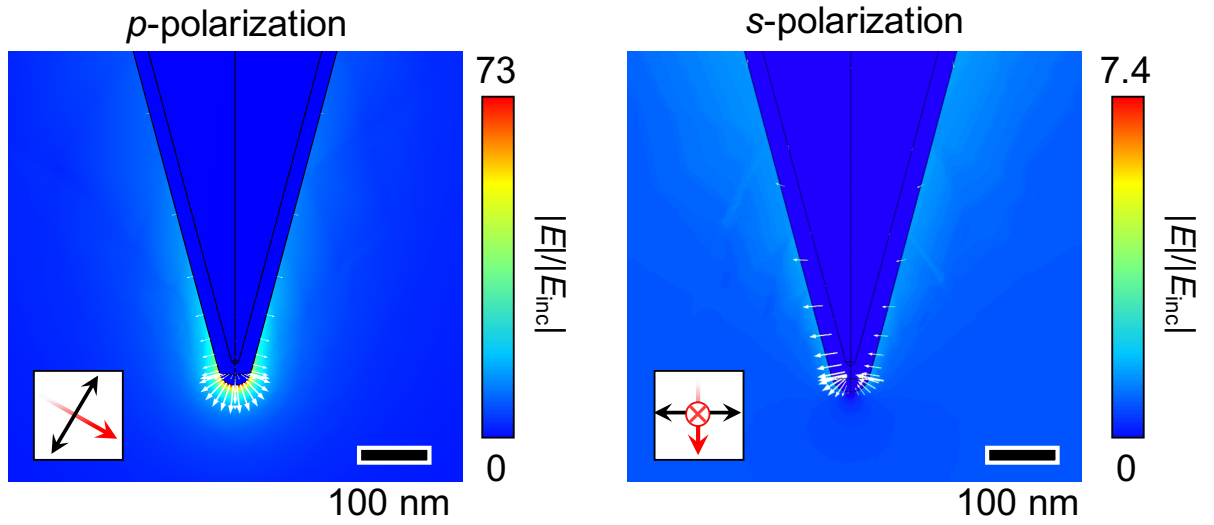


**Figure 6.4:** FEM results of the electromagnetic field distribution around a tip and its dependence on the polarisation of the irradiated light under IR irradiation at  $1075\text{ cm}^{-1}$ . The white arrows indicate the direction of the vector field, revealing the existence of  $z$ -polarised NF on the tip apex.

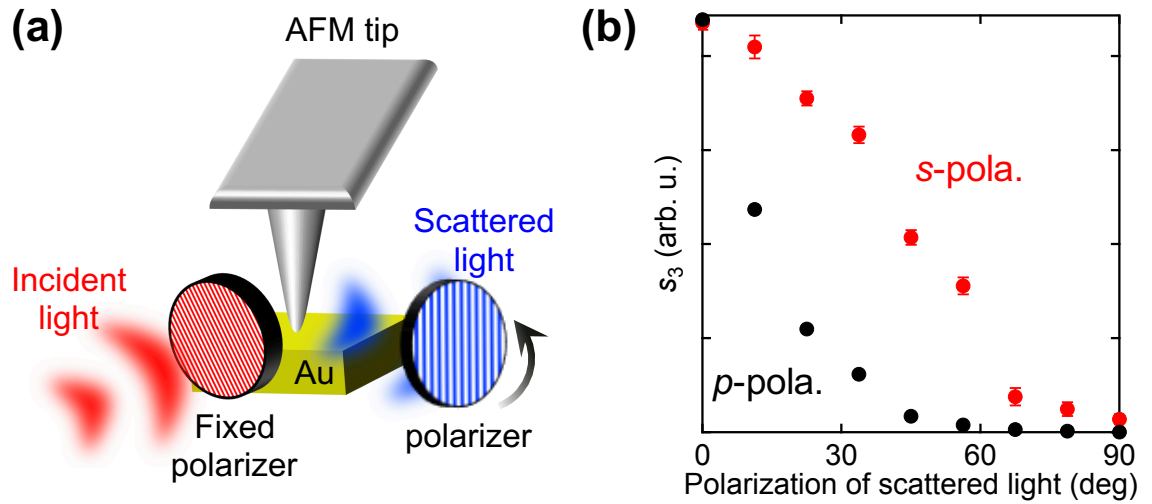


**Figure 6.5:** (a) Illustration of the measurement for the polarization dependence of the scattered light. (b) Polarization-resolved measurements of scattered light at  $\theta_{\text{in}} = 0$  and  $90^\circ$ .

	(a)	(b)
$\theta_{\text{out}}$ (deg.)	90	90
$\theta_{\text{in}}$ (deg.)	90	0
polarization of incident light	<i>s</i> -polarization	<i>p</i> -polarization

**Table 6.2:** The summary of the optical setup (Fig. 6.6).

condition allowed the scattered light to interfere with the reference light of *s*-polarization, thereby enhancing only the *s*-polarized components due to the linearity of the wave equations. The remaining *p*-polarized or other polarization components were blocked by the polarizer positioned in front of the MCT detector.

Another setup, as illustrated in Fig. 6.6(b), had  $\theta_{\text{out}}$  set to 0 degrees and utilized a quarter-wavelength plate placed in the reference arm. In this setup, the IR light traveling to the reference arm passed through the quarter-wavelength plate twice, resulting in the polarization of the reference light interfering with the scattered light being *s*-polarization. An important distinction of this optical configuration is that the polarization of the incident light was *p*-polarization. The details of these optical setups are summarized in Table 6.2.

### 6.3.3 In-plane visualization of the optical field vector

Using the developed optical setup described above, in-plane imaging was performed, and the most important results in this chapter are presented in Fig. 6.8. Fig. 6.8(a) and (b) correspond to the NF phase images taken with the setups (a) and (b) from Fig. 6.6, respectively. In Fig. 6.8(a), a weak phase reversal of approximately 1 rad parallel to the polarization of the incident light was observed, which strongly suggests the presence of the in-plane optical field vector. On the other hand, Fig. 6.8(b) does not exhibit NF-phase contrast. This comparison highlights that irradiation with *s*-polarization is preferable for optically visualizing the in-plane optical field vector.

An interesting result is the absence of NF-phase contrast in Fig. 6.8(b), even though the amplitude of the NF with *s*-polarization is approximately the same as in the condition of Fig. 6.8(a), as demonstrated in Fig. 6.13. This suggests that the NF components in the in-plane are unpolarized. If so, each polarization component in the in-plane, such as *x* or *y*, is separated within the in-plane, leading to very weak in-plane-resolved NF-phase information.

To investigate this hypothesis, I examined the in-plane distribution of the optical-field vector through FEM simulations. Fig. 6.9 displays the distribution of the optical field vector under irradiation with *s*-polarization (a) and *p*-polarization. A strongly distorted distribution can be seen under *s*-polarization, as shown in Fig. 6.9(a), while a symmetric

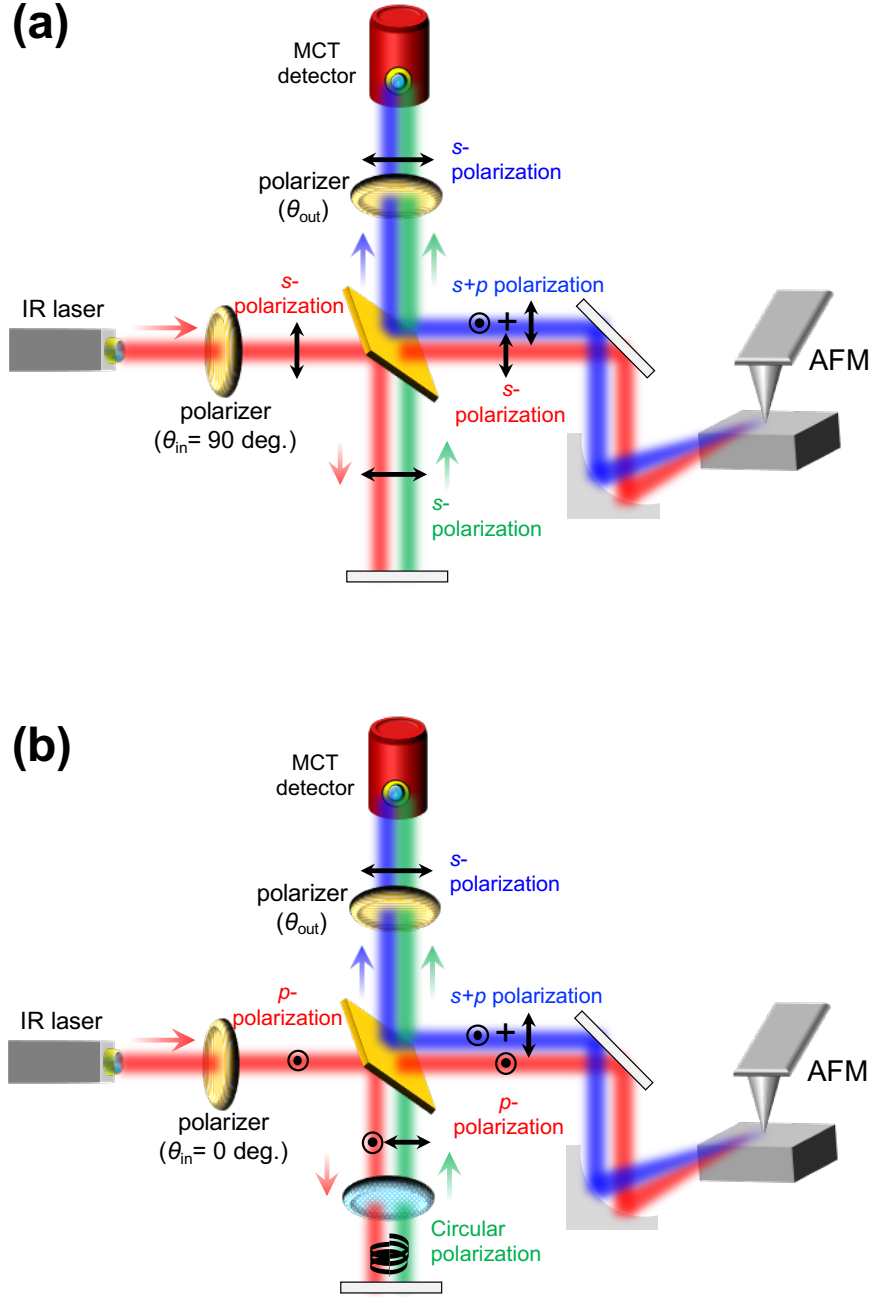


**Figure 6.6:** (a) Illustration of the measurement for the polarization dependence of the scattered light. (b) Polarization-resolved measurements of scattered light at  $\theta_{in} = 0$  and  $90 \text{ deg.}$

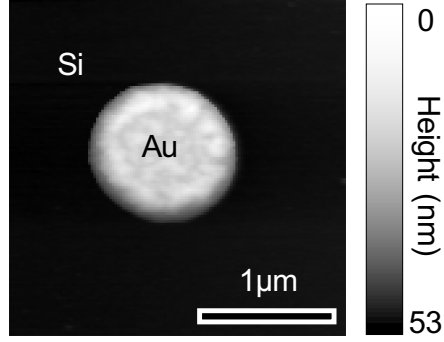


**Figure 6.7:** Topography of an Au disk for in-plane visualization.

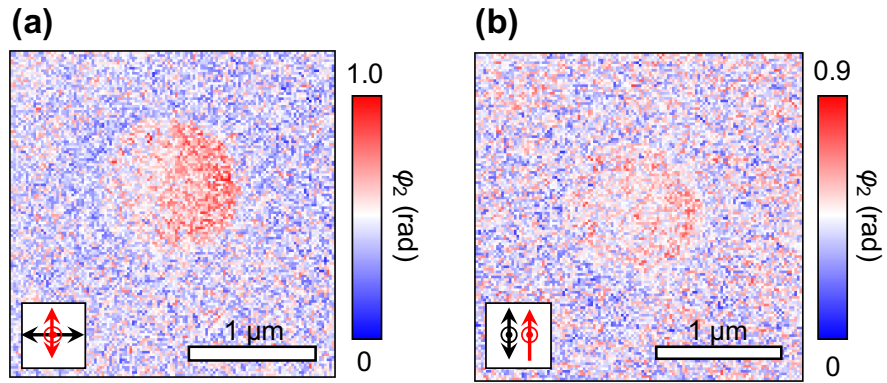


**Figure 6.8:** (a) Illustration of the measurement for the polarization dependence of the scattered light. (b) Polarization-resolved measurements of scattered light at  $\theta_{\text{in}} = 0$  and 90 deg.

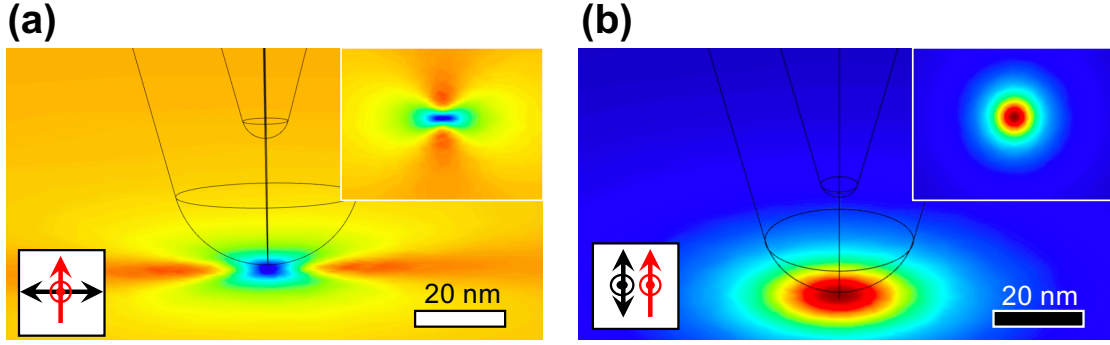


**Figure 6.9:** (a) Illustration of the measurement for the polarization dependence of the scattered light. (b) Polarization-resolved measurements of scattered light at  $\theta_{\text{in}} = 0$  and  $90$  deg.

distribution is evident under  $p$ -polarization, as shown in Fig. 6.9(b). This symmetric distribution of the optical-field vector results in a reduced polarization component in the in-plane direction, thus explaining the absence of NF-phase contrast under  $p$ -polarization, as shown in Fig. 6.8.

#### 6.3.4 Plasmon nanofocusing

Another approach to achieving  $s$ -polarized NFs involves utilizing plasmon nanofocusing, which allows for the transmission of polarized optical fields to specific locations through precise engineering. In this section, I propose the use of plasmon nanofocusing, specifically a tapered transmission line (see Fig. 6.10) [94]. By integrating a tapered transmission line onto the AFM tip to focus the hot spot onto the AFM-tip apex, it is expected that  $s$ -polarized NFs can be efficiently transmitted.

For patterning a tapered transmission line, a focused-ion beam (FIB) has been employed. This process offers several advantages, such as avoiding contamination and breakage under ultrasonic washing. To ensure electrical disconnection, the area around the apex has been sufficiently etched.

The FIB-patterned tip is depicted in Fig. 6.11. Its geometry (Fig. 6.12(a)) has been optimized using finite element method (FEM) simulation to efficiently excite the in-plane-polarized hot spot at an AFM-tip apex, as shown in Fig. 6.12(b).

To demonstrate the existence of  $s$ -polarized NFs transmitted by a tapered transmission line, I investigated the dependence of  $s_3$  on  $\theta_{\text{in}}$ .

Fig. 6.13 shows  $s_3$  versus  $\theta_{\text{in}}$  at  $\theta_{\text{out}} = 90^\circ$ . Fig. 6.13(a) presents the results for PrIr, which indicates a weak excitation of the NF with  $s$ -polarization. On the other hand, a stronger peak was observed at  $\theta_{\text{in}} = 90^\circ$  for the FIB-patterned tip, as shown in Fig. 6.13(b). These different contrast between  $s$ - and  $p$ -polarization demonstrates the existence of  $s$ -polarized NFs transmitted by a tapered transmission line.

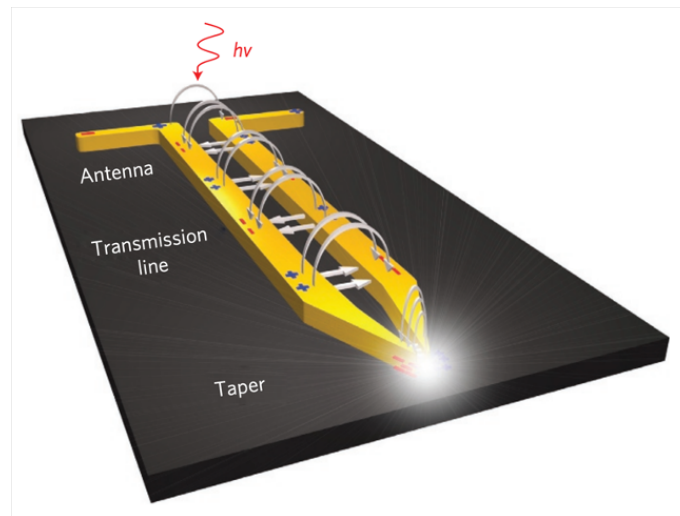


**Figure 6.10:** Illustration of the nanofocusing using tapered transmission lines. Reprinted figures with permission from Ref. [94]. Copyright 2011 by Springer Nature.

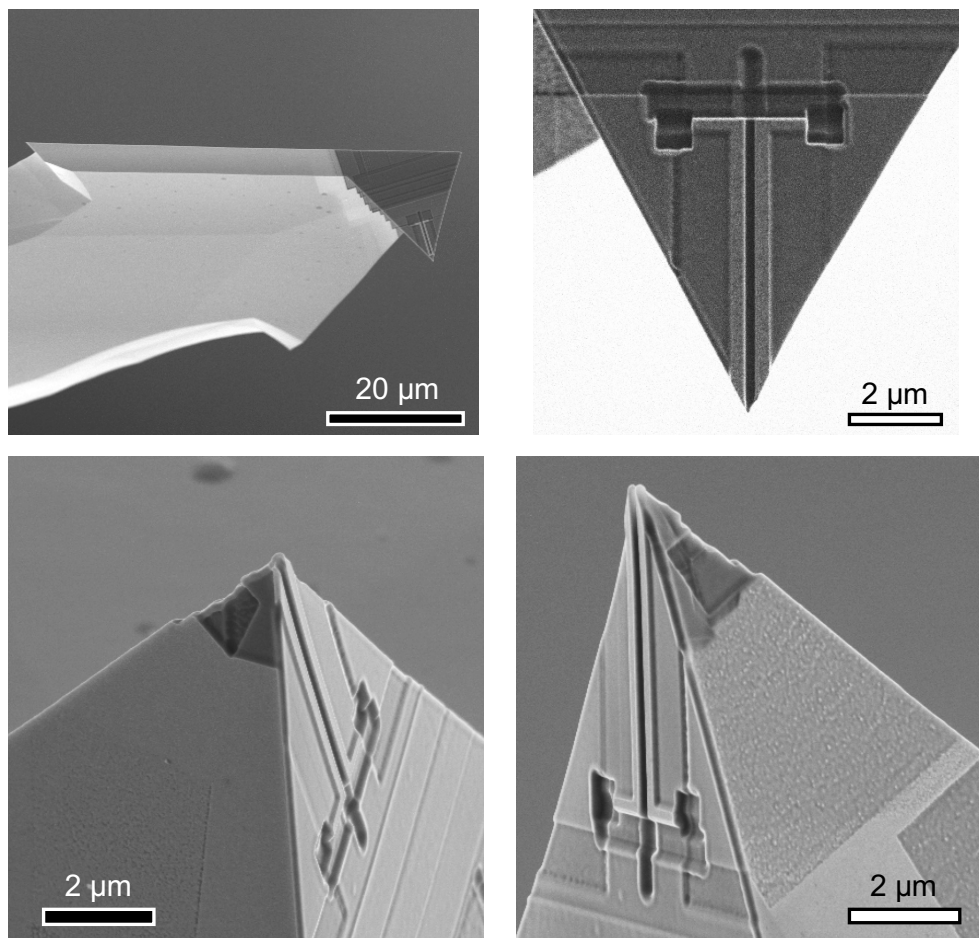


**Figure 6.11:** The SEM images of the FIB-patterned AFM tip for plasmonic nanofocusing.



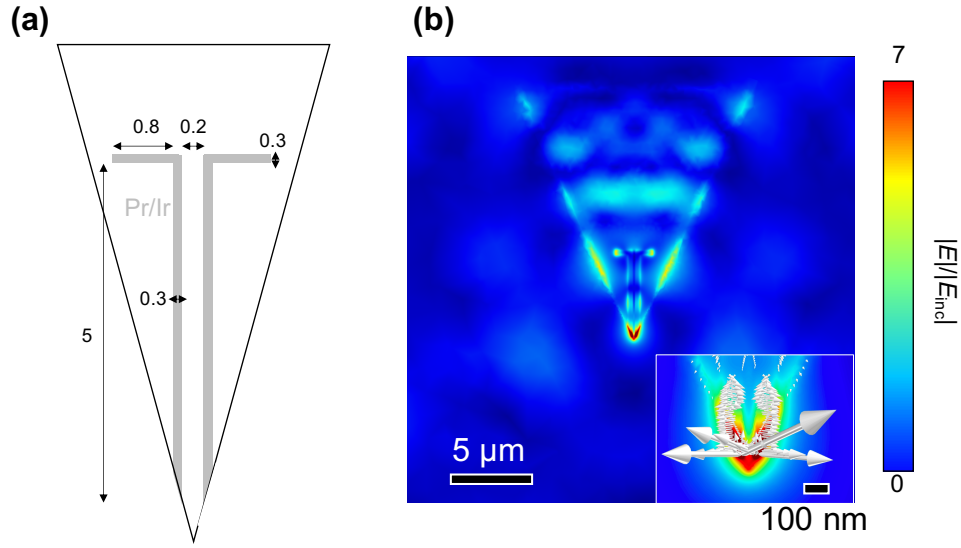


**Figure 6.12:** (a) Geometry of tapered transmission lines. (b) FEM simulation results for the FIB-patterned AFM tip. Inset; enlarge image of the apex.

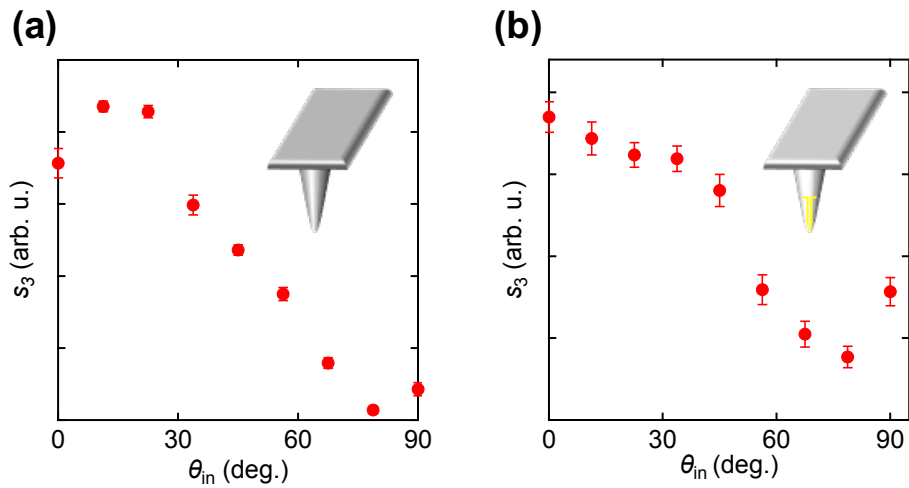


**Figure 6.13:** (a) Illustration of the measurement for the polarization dependence of the scattered light. (b) Polarization-resolved measurements of scattered light at  $\theta_{\text{in}} = 0$  and  $90$  deg.

## 6.4 Conclusion of Chapter 6

In conclusion, I have developed in-plane and out-of-plane resolved s-SNOM measurements. The controllability of polarization in the reference arm of the Michelson interferometer and the linearity of the wave equation for light enhance the detection of small NF signals with *s*-polarization. This enhancement was demonstrated through in-plane NF imaging of the Au disk.

To further improve the excitation efficiency of NFs with *s*-polarization, I patterned a tapered transmission line onto an AFM tip and successfully demonstrated the existence of resulting *s*-polarized NFs. This achievement, the first of its kind, paves the way for constructing nanoscale three-dimensional vectorial field mappings beyond the diffraction limit.



## Chapter 7

# Conclusions

**In this chapter, the studies referred to in this thesis are summarized and their importance is presented.**

### 7.1 Conclusions of this thesis

In this dissertation, a systematic and experimental exploration of the s-SNOM technique for visualizing the optical field vector has been presented through a multifaceted approach.

To obtain two physical values that characterize the optical field vector, phase-resolved s-SNOM was utilized. The introduction of reference light not only enabled the extraction of the NF phase but also improved SNR and spatial resolution. To quantitatively evaluate its performance, a quasistatic model, incorporating the dynamics of an AFM tip, was developed, and the s-SNOM setup's performance was assessed.

Utilizing s-SNOM, the optical field vector on an LSA was visualized. By employing tunable IR lasers and rotating the LSA, its characteristic optical properties, such as broadband response and polarization independence, were directly demonstrated through NF amplitude images. These images agreed well with finite element method (FEM) simulations of the electric field components  $E_z$  and  $|E|$ .

Furthermore, the NF phase image exhibited a phase jump of  $\pi$  at the center of the bow-tie part, suggesting the presence of a bridged optical field vector. However, the experimental demonstration by optical means is a difficult task due to the diffraction limit.

To confirm this hypothesis, electrical measurements of QDs placed at the LSA's center were employed as a novel approach. The QD integrated with the LSA exhibited photocurrents approximately 10,000 times stronger than those without the LSA, providing experimental evidence for the existence of the bridged optical field vector. These results collectively indicate the feasibility of reconstructing the optical field vector characterized

by both amplitude and direction.

Based on the NF images of the LSA, it was inferred that the probed optical field vector component is predominantly out-of-plane. Thus, an investigation of NF polarization in s-SNOM was conducted using structural information from banded PHB spherulites. This unique approach helped avoid the complex interpretation issues stemming from the coupling between the NF and the optical field vector on optical devices. A comparison with a rich FTIR database and structural information obtained via far-field microscopy clarified that s-SNOM predominantly probes out-of-plane optical field components. This not only confirms that s-SNOM primarily probes out-of-plane optical field components but also raises intriguing questions regarding the feasibility of in-plane NF imaging.

Finally, the exploration of in-plane NF imaging was undertaken. Leveraging the optical setup flexibility of the Michelson interferometer and the linearity of the electromagnetic field, the extraction of weak NFs with s-polarization was achieved. Additionally, to enhance NFs with s-polarization, a proposal and demonstration of the utility of plasmonic nano-focusing using a focused ion beam FIB-patterned AFM tip with a tapered transmission line were presented.

## 7.2 Future prospects

## 7.3 Future Prospects

In this thesis, I have systematically conducted studies on NFs, encompassing theoretical considerations, characteristics, and measurements of the optical field vector within optical devices. I envision two primary avenues for future research:

Firstly, I foresee research focused on nanoscale optical 3D reconstruction. Leveraging the in-plane probing technique pioneered in this dissertation, I can anticipate achieving nanoscale 3D reconstruction of the optical field vector. This 3D reconstruction holds the potential to directly assess the functionality and performance of designed optical devices, making it a significant goal in this line of research.

Secondly, I propose exploring the application of NF measurements in other fields. While this study indirectly integrated NF photonics with quantum electronics, as demonstrated in Chapter 4, such optoelectronic interactions have not been extensively explored within the realm of NF optics. To gain a more direct understanding of these nanoscale electron/light phenomena, "*Operando*" measurements are preferred. "*Operando*" experiments involve studying samples or devices in operation, such as batteries or electrical devices.

Here are specific examples of potential future studies:

### 7.3.1 Nanoscale 3D reconstruction of optical-field vector

#### Material approach; surface phonon polariton

The key challenges in demonstrating this 3D reconstruction are the low SNR and the presence of artifacts. To overcome both of these hurdles, I propose an approach that involves selecting appropriate host materials, specifically polar materials.

In the MIR band, polar materials can be excited to undergo lattice oscillations, effectively canceling incident irradiation light. Consequently, the bulk propagation of light is effectively prohibited<sup>1</sup>. However, surface modes, known as surface phonon polaritons (SPhPs), remain allowed. These SPhPs appear at the flat surface of a polar material with very high reflection, thus it can be thought to be one of the best platforms to demonstrate the nanoscale 3D reconstruction.

Among various polar materials, silicon carbide (SiC) stands out as it can be excited by the MIR light emitted by the CO<sub>2</sub> gas laser used in this thesis. When highly reflective materials, such as gold (Au), are introduced, these SPhPs are reflected and form standing waves, as depicted in Fig. 7.1. Given that the physical nature of SPhPs is that of surface waves, both out-of-plane and in-plane components are expected to exhibit periodic variations. Consequently, it is anticipated that the spatial phase of in-plane and out-of-plane NF amplitudes ( $s_n^{\text{out}}, s_n^{\text{in}}$ ) will be reversed by  $\pi$ , as shown in Fig. 7.1. The 3D electrical field vector  $\mathbf{E}$  may be derived as follows:

$$\mathbf{E}(\nu) \propto s_n^{\text{out}}(\nu)\mathbf{z} + \eta^{\text{in}} \cdot s_n^{\text{in}}(\nu)\mathbf{r}^{\text{in}} \quad (7.1)$$

Here,  $\mathbf{r}$  represents the unit in-plane vector (expressed as  $\mathbf{x}$  and  $\mathbf{y}$ ), and  $\eta^{\text{in}}$  denotes the coupling efficiency during in-plane measurements.

#### Setup approach; tilting an AFM tip

I propose further improvements to the experimental setup aimed at enhancing  $\eta^{\text{in}}$ . In Chapter 6, it was observed that the NF is strongly polarized in the direction of the long axis of the AFM tip. Based on this finding, tilting the AFM tip becomes a viable method to optically couple a portion of the NF component polarized along the long axis of the AFM tip with the in-plane component of the host material.

To achieve this, it is imperative to develop a precise tilt-controlling mechanism. Additionally, automating the modification of the optical path for the deflection laser according to the tilting angle will be necessary to realize this concept.

---

<sup>1</sup>Mathematically, the real part of the dielectric function  $\Re[\epsilon] \sim -1$

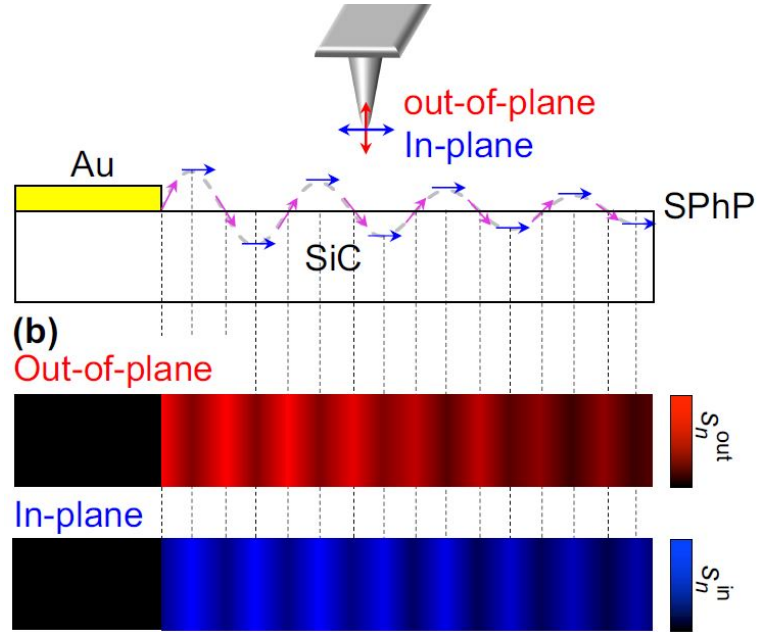


**Figure 7.1:** Illustration of the SPhP and expected results for  $s_n^{\text{out}}$  and  $s_n^{\text{in}}$ .

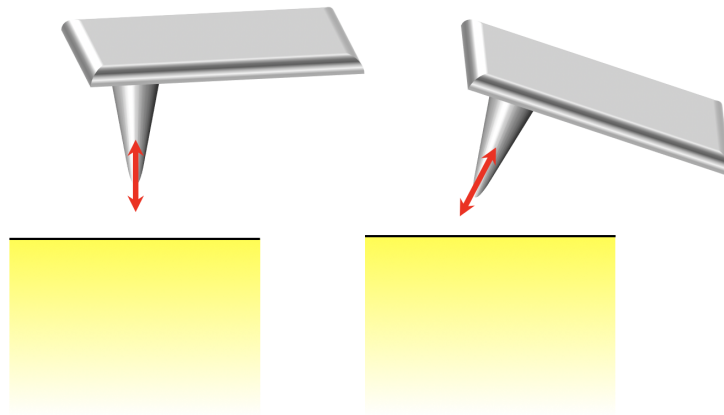


**Figure 7.2:** Schematic of a tilting AFM tip.

### Software approach: low-light imaging

Since the in-plane polarized NF signal primarily originates from weak optical coupling efficiency with the tip, there is a fundamental limit to improving the experimental method, even with high-power lasers and ultra-sensitive sensors. Therefore, I propose an alternative approach to enhance the NF signal through post-processing after data acquisition.

Specifically, this involves improving the SNR using computational methods such as machine learning [95]. This method has recently gained attention in industries like surveillance cameras and low-light photography.

Traditionally, enhancing contrast involves adjusting the dynamic range, a technique also used in this study. However, machine learning enables us to improve both contrast and reduce noise [95]. By applying this method to s-SNOM, I can expect a significant enhancement in SNR.

#### 7.3.2 Nanoscale *Operand* optoelectronic measurements

The key feature of this research lies in its perspective of interpreting NF measurement results within the context of other research fields. Specifically, the bridged optical field vector at the center of the LSA was experimentally demonstrated through electronic measurements. However, it's crucial to note that this was essentially an indirect demonstration due to the independence of these measurement systems. In response to this limitation, I propose a nanoscale-spatially-resolved Operando measurement approach by integrating s-SNOM with other measurements.

A preferred platform that I propose for this integration is the de-trapping processes from the donor level, as phenomenologically demonstrated in Chapter 4. Recent advancements in doping methods have enabled the precise implantation of single donors at a high order. Additionally, the use of donor levels with deeper potential energy than the thermal energy at room temperature has been reported, which is advantageous for s-SNOM used in room temperature environments.

In particular, a transistor structure, as shown in the figure, is believed to be capable of mapping the current value to the tip's position as a variable. By vibrating the tip at its resonant frequency  $\Omega_{\text{tip}}$ , the higher-order photocurrent Fourier components  $|I_n|$  can be obtained through lock-in detection, given that the NF exhibits integer multiples of non-linear frequencies (as modeled in Chapter 2). Such photocurrent has been demonstrated via photothermal electric current in graphene [96].

For example, as illustrated in Figure 7.3(b), aligned donor atoms do not merge with each other, resulting in a completely isolated donor band (Figure 7.4(a)). This geometric arrangement allows the electrons trapped in a single atom to efficiently interact with "tiny light" (NF), leading to an efficient detrapping process despite the angstrom-scale size. The



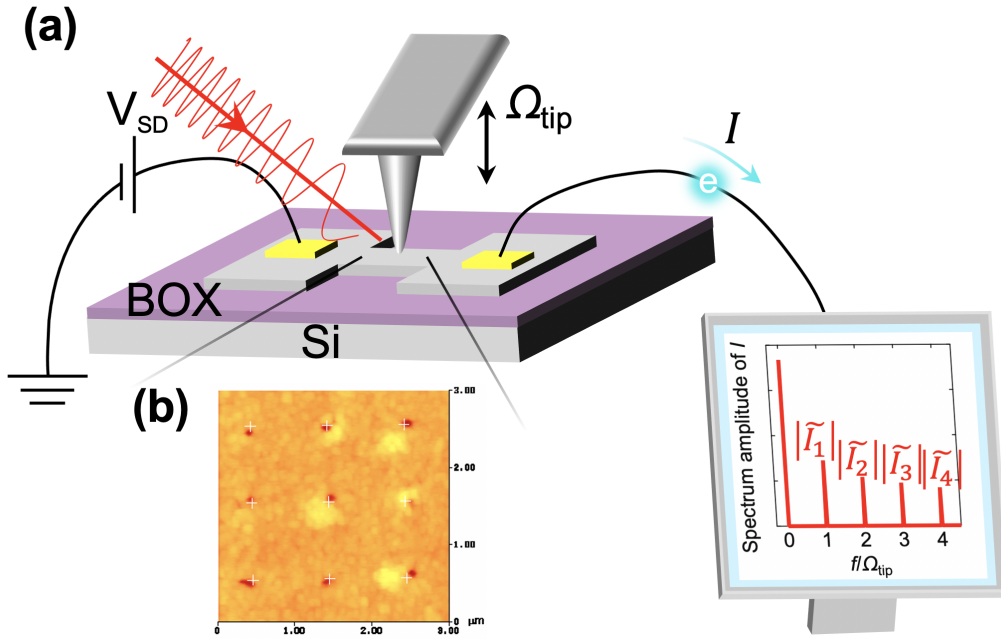


**Figure 7.3:** (a) Experimental setup for NF optoelectronic measurements. (b) Arrayed donor implanted in a Si substrate. Reprinted figures with permission from Ref. [97]. Copyright2005 by Springer Nature.

anticipated experimental results are depicted in Figures 7.4(b) and (c): NF absorption due to detrapping is observed as in Figure 7.4(b), and the localized appearance of photocurrent is evident in the  $|I_n|$  distribution in Figure 7.4(c).

This proposal not only establishes a new research domain, "near-field nanoscale optoelectronics," but also opens up the possibility of single-atom photonics.

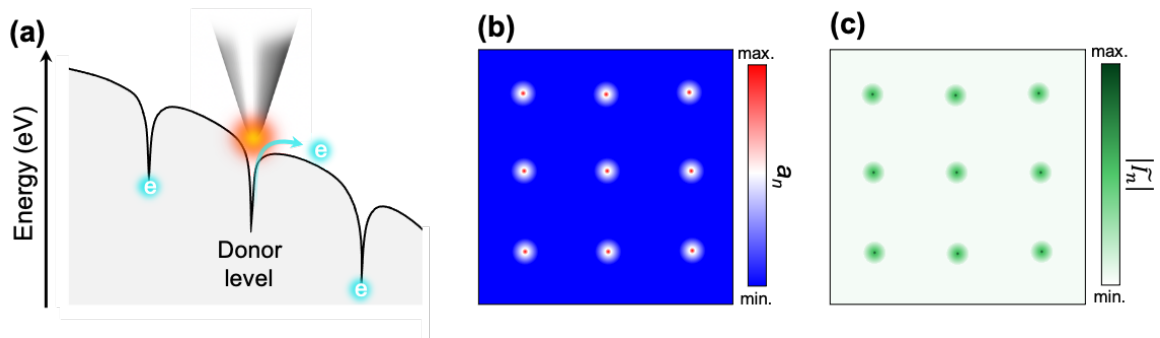


**Figure 7.4:** Expected results. (a) Schematic of detrapping processes by the NF. (b) NF absorbance image. (c) Nanoscale spatially-resolved photocurrents image.

# Publications and Presentations

## Journal paper

### Original paper

#### Presented in this thesis:

1. **T. Okamoto**, N. Fujimura, L. Crespi, T. Koder, Y. Kawano. “Terahertz detection with an antenna-coupled highly-doped silicon quantum dot”. *Scientific Reports* **9**, 18574 (2019). [**Chapter4**]
2. **T. Okamoto**, T. Sugaya, N. Fujimura, K. Ishikawa, Y. Kawano. “Near-field infrared investigations of an arm-terminated spiral structure with bow-tie probe”, *Journal of Physics Communications*, **2(10)**, 105004, (2018). [**Chapter3**]
3. **T. Okamoto**, M. Ryu, T. Yoshida, J. Morikawa, Y. Kawano. “Utilisation of the Vectorial Nature of Near Fields for Optically Accessing Multiscale Structures”, *submitted to Nat. Nanotech..* [**Chapter5**]

#### Other publications:

4. D. Suzuki<sup>†</sup>, **T. Okamoto**<sup>†</sup>, J. Li<sup>†</sup>, Y. Ito, T. Fujita, Y. Kawano. “Terahertz and Infrared Response Assisted by Heat Localization in Nanoporous Graphene” , submitted to CARBON (<sup>†</sup> **contributed equally first author**)
5. **T. Okamoto**, Y. Ito, N. Nagamura, K. Akada, T. Fujita, Y. Kawano. “Topological effects of three-dimensional porous graphene on Dirac quasiparticles”. arXiv:2002.00795 [cond-mat.mtrl-sci], (2020).

## Proceedings

1. **T. Okamoto**, N. Fujimura, L. Crespi, T. Koder, Y. Kawano. “ Dopant-Induced Terahertz Resonance of a Dopant-Rich Silicon Quantum Dot”, *Silicon Nanoelectronics Workshop 2019* p1-2, (2019).

2. **T. Okamoto**, Akira Sasagawa, Yota Harada, Satsuki Nakano, Wataru Norimatsu, Michiko Kusunoki, Yukio Kawano. Visualization of Zero-Dimensional Plasmons in Graphene Quantum Dots with Near-Field Infrared Microscopy, *43rd International Conference on Infrared, Millimeter, and Terahertz Waves 2018 (IRMMW-THz 2018)*, pp. 1-2, (2018).
3. R. Yuasa, **T. Okamoto**, A. Sasagawa, Y. Kawano, “Nanoscale observation of real-space mid-infrared field distribution in a stamp-type plasmonic structure”, *43rd International Conference on Infrared, Millimeter, and Terahertz Waves 2018 (IRMMW-THz 2018)*, pp. 1-2, (2018).
4. **T. Okamoto**, D. Suzuki, Y. Ito, T. Fujita, Y. Kawano, “Analyzing Nanoscale Optical and Thermal Properties in Nanoporous Graphene by Near-Field Infrared Microscopy”, *42nd International Conference on Infrared, Millimeter, and Terahertz Waves 2018 (IRMMW-THz 2018)*, pp. 1-2, (2017).

## Presentations

### Invited talks

1. **T. Okamoto** & Y. Kawano “Nanoscale measurement of surface optical field vector using near-field infrared light - Utilizing lattice vibration resonance-”, *26th meeting of the Japan Optical Society Nano-Optics Research Group*, Tokyo, Japan, Dec. 2019.
2. **T. Okamoto** & Y. Kawano “Nanoscale observation of confined mid-infrared field distribution in a spiral antenna with scanning near-field optical microscopy”, *Recent advances in spectroscopic imaging and related modern techniques 3*, Tokyo, Japan, Dec. 2019.
3. **T. Okamoto** “Topological effects of transforming two-dimensional graphene into three-dimensional graphene”, *Graphene Technology-2020*, Lisbon, Portugal, Feb. 2020.

### International conferences

1. **T. Okamoto**, N Fujimura, T Koderu, Y Kawano. “Dopant-Induced Terahertz Resonance of a Dopant-Rich Silicon Quantum Dot”, *Silicon Nanoelectronics Workshop 2019*, Kyoto, Japan, Jun. 2019.
2. **T. Okamoto**, Y. Ito, N. Nagamura, T. Fujita, Y. Kawano. “Three-Dimensional Spatial-Topology Effects, Magnetoresistance in Three-Dimensional Porous Graphene”,

*The 10th annual Recent Progress in Graphene and Two-dimensional Materials Research Conference (RPGR2018)*, Guilin, China, Oct. 2018.

3. A. Sasagawa, **T. Okamoto**, Y. Harada, S. Nakano, W. Norimatsu, M. Kusunoki, Y. Kawano, "Direct observation of plasmons in graphene quantum dots with scanning near-field optical microscopy", *The 10th annual Recent Progress in Graphene and Two-dimensional Materials Research Conference (RPGR2018)*, Guilin, China, Oct. 2018.
4. **T. Okamoto**, A. Sasagawa, Y. Harada, S. Nakano, W. Norimatsu, M. Kusunoki, Y. Kawano, "Visualization of Zero-Dimensional Plasmons in Graphene Quantum Dots with Near-Field Infrared Microscopy", *43rd International Conference on Infrared, Millimeter, and Terahertz Waves 2018 (IRMMW-THz 2018)*, Aichi, Tokyo, Sep. 2018.
5. R. Yuasa, **T. Okamoto**, A. Sasagawa, Y. Kawano, "Nanoscale observation of real-space mid-infrared field distribution in a stamp-type plasmonic structure", *43rd International Conference on Infrared, Millimeter, and Terahertz Waves 2018 (IRMMW-THz 2018)*, Aichi, Tokyo, Sep. 2018.
6. **T. Okamoto**, Y. Ito, T. Fujita, Y. Kawano. Photothermoelectric Terahertz Detection with p-n Junction Nanoporous Graphene, *Graphene2018*, Graphene 2018 Abstract BookDresden, Germany, Jun. 2018.
7. **T. Okamoto**, N. Fujimura, W. Gao. J. Kono, Y. Kawano, "Response of localized carriers to terahertz radiation in a carbon nanotube film", *The 54th Fullerenes-Nanotubes-Graphene Symposium*, Tokyo, Japan, July 2017.
8. **T. Okamoto**, Y. Ito, T. Fujita, Y. Kawano, "Optical Control of Weak Localization in Nanoporous Graphene", *The 53rd Fullerenes-Nanotubes-Graphene Symposium*, Kyoto, Japan, July 2017.
9. **T. Okamoto**, D. Suzuki, Y. Ito, T. Fujita, Y. Kawano, "Analyzing Nanoscale Optical and Thermal Properties in Nanoporous Graphene by Near-Field Infrared Microscopy", *42nd International Conference on Infrared, Millimeter, and Terahertz Waves 2017(IRMMW-THz)*, Cancun, Mexico, Oct. 2017.

### Domestic Conference

1. **T. Okamoto**, Y. Takuya, R. Meguya, M. Junko, Y. Kawano, "Nanoscale spatially-resolved vibrational spectroscopy of lamellar structure by using scanning near-field optical microscopy", *69th SPSJ Annual Meeting*, Fukuoka, Japan, May 2020 (cancelled due to COVID-19, for announcement)

2. **T. Okamoto**, N. Fujimura, K. Ishikawa, L. Crespi, T. Koderu, Y. Kawano, "Directly nanoscale observation of optictical-field vector in logarithm spiral antenna for the infrared band using scanning near-field optical microscopy and its application", *80th Japan Society of Applied Physics*, Hokkaido, Japan, Sep. 2019.
3. T. Yoshida, **T. Okamoto**, M. Ryu, J. Morikawa, Y. Kawano, "Nanoscale infrared-spectroscopy for orientaion of higher-order struc cture in polyhydroxybutyrate spherulites using neas-field optical microscopy", *80th Japan Society of Applied Physics*, Hokkaido, Japan, Sep. 2019.
4. **T. Okamoto**, Y. Ito, T. Fujita, Y. Kawano, "Topological effects on Dirac electror curved graphene", *79th Japan Society of Applied Physics*, Aichi, Japan, Sep. 2018.
5. A. Sasagawa, **T. Okamoto**, Y. Harada, S. Nakano, W. Norimatsu, M. Kusunoki, Y. Kawano, "Visualization of Zero-Dimensio Near-Field Infrared sional Plasmons in Graphene Quantum Dots with Ne Microscopy", *79th Japan Society of Applied Physics*, Aichi, Japan, Sep. 2018.
6. R. Yuasa, **T. Okamoto**, A. Sasagawa, Y. Kawano, "Nanoscale Observation of Mid-Infrared Field Distribution in a Stamp-Type Plasmonic Structure", *79th Japan Society of Applied Physics*, Aichi, Japan, Sep. 2018.
7. **T. Okamoto**, Y. Ito, T. Fujita, Y. Kawano, "Geomtric control of weak localization with nanoporous graphene", *73th Japan Society of Physics (JSP)*, Tokyo Univerity of Science, Chiba, Japan, Mar. 2018.
8. **T. Okamoto**, D. Suzuki, Y. Ito, T. Fujita, Y. Kawano, "Observation of heat localization in nanoporous graphene by near-field optical microscopy", *78th Japan Society of Applied Physics*, Fukuoka, Japan, Mar. 2017.
9. A. Sasagawa, **T. Okamoto**, Y. Kawano, "Evaluation of layer of graphene by near-field mid-infrared microscopy", *78th Japan Society of Applied Physics*, Fukuoka, Japan, Mar. 2017.

# List of Figures

1.1	Electromagnetic spectrum. . . . .	14
1.2	Schematic diagram of the diffraction limit. . . . .	16
1.3	Comparison of the spatial resolution using three wavelengths in the FIR region. The left pictures are visible light images, and the right ones are FIR images. Reprinted figures with permission from Ref. [28]. Copyright 2016 by Springer Nature. . . . .	16
1.4	(a) schematic illustration of EELS and CL. (b) optical-field maps of an Ag nanoparticle. Reprinted figures with permission from Ref. [36]. Copyright 2018 American Chemical Society. . . . .	17
1.5	Illustration of an s-SNOM (left) and a-SNOM (right.) . . . . .	18
1.6	Outline of this dissertation. . . . .	21
2.1	Numerically calculated distribution of electric field. . . . .	24
2.2	SEM image of a Pr/Ir-coated AFM tip typically used in this thesis. . . . .	26
2.3	Optical setup of the s-SNOM. . . . .	28
2.4	NF phase image of SiO <sub>2</sub> and Si. . . . .	30
2.5	Histogram of $s_3$ for SiO <sub>2</sub> and Si. . . . .	31
2.6	Approach curves with and without reference light. . . . .	32
2.7	Comparison of the raw model and the discretized model meshed with three different element sizes. . . . .	32
2.8	The process of discretizing the wavefunction. . . . .	33
2.9	Calculation flow of the FEM simulation. . . . .	34
2.10	Meshed geometry of an AFM-tip . . . . .	35
2.11	Static approach curve for Au substrate. . . . .	36
2.12	Time-domain behavior of $E_{\text{NF}}$ for an Au substrate. . . . .	37
2.13	Spectrum amplitude of Fourier-transformed $E_{\text{NF}}$ using Fig. 2.12. . . . .	37
2.14	Dynamic approach curve for an Au substrate. . . . .	38
2.15	Experimental approach curve for an Au substrate. . . . .	38
2.16	(a) Electrical distribution of an AFM-tip apex for several tip-sample distances. (b) Static approach curve for three substrates. . . . .	39
2.17	Time-domain behavior of $E_{\text{NF}}$ for three substrates. . . . .	39

2.18	Dynamic approach curve for three substrates. . . . .	40
2.19	Experimental approach curve for three substrates. For a $\text{CaF}_2$ substrate, the 4th-order demodulated result is not shown because it is almost noise level. . . . .	40
2.20	Comparison of the spatial resolution between the experimental and simulated results. . . . .	41
3.1	Designed LSA characterized by (3.8). . . . .	46
3.2	Designed non-arm-terminated LSA characterized by (3.8) . . . . .	47
3.3	(a) $S_{11}$ parameter. (b) Complex impedance in radial coordinates. Adapted from the Ref. [34, 68]. ©2018 The Author(s). Distributed under a Creative Commons Attribution 3.0 and 4.0 International license (CC BY 3.0 and 4.0), respectively . . . . .	48
3.4	Optical image of a fabricated LSA. . . . .	49
3.5	Schematic illustration of s-SNOM setup for LSA measurements. Adapted from the Ref. [34]. ©2018 The authors. Distributed under a Creative Commons Attribution 3.0 International license (CC BY 3.0). . . . .	49
3.6	Wavenumber dependence of the NF images of the LSA. . . . .	50
3.7	incident-angle dependence of NF images of the electric fields on the LSA at $\theta = 0, \pi/4, \pi/2$ , and $\pi/2$ . The dashed circles are guides to the eye. Adapted from the Ref. [34]. ©2018 The authors. Distributed under a Creative Commons Attribution 3.0 International license (CC BY 3.0). . . .	51
3.8	(a) Experimental result. (b) Calculated data for $ E_{\text{norm}} $ , $ E_{\text{out}} $ , and $ E_{\text{in}} $ .	52
3.9	NF phase at the center of the LSA. . . . .	53
3.10	Comparison experiment of bow-tie antenna without a spiral structure. . .	54
3.11	Illustration of the predicted light field. . . . .	55
4.1	Left; Potential profile of dopant-rich system in Si. Right; modification of observable current with de-trapped/trapped condition. Reprinted figures with permission from Ref. [21]. Copyright 2011 WILEY-VCH Verlag GmbH & Co. KGaA, Weinheim . . . . .	58
4.2	<b>a.</b> Schematic channel structure for probing trapping dynamics on defect state. <b>b.</b> Illustration of modification of percolation pathway by changing electrostatic potential. Reprinted figures with permission from Ref. [76]. Copyright 2005 by Springer Nature. . . . .	59
4.3	(a) Optical image of the LSA integrated with Si QD. (b) SEM image of the bow-tie part located in the center of the LSA. (c) SEM image of the Si QD. Adapted from the Ref. [68]. ©2019 The authors. Distributed under a Creative Commons Attribution 4.0 International license (CC BY 4.0). . .	59

4.4	Optical and cryogenic setup. . . . .	60
4.5	The $V_G$ dependence of the dark current $I_{\text{dark}}$ (the dark curve) and the FIR photocurrent $I_{\text{FIR}}(\nu)$ (the other colored curves) was recorded at a source-drain voltage of 5 mV under the FIR irradiation with six frequencies. . . .	62
4.6	Frequency dependence of the responsivity at the various $V_G$ . Adapted from the Ref. [68]. ©2019 The authors. Distributed under a Creative Commons Attribution 4.0 International license (CC BY 4.0). . . . .	63
4.7	left: schematic of the photon-assisted tunneling process. right: Satellite peaks observed in the Coulomb blockade. The inset shows the peak position of the satellite peak versus the photon energy of irradiation. Reprinted figures with permission from Ref. [23]. Copyright 2008 AIP Publishing. . .	63
4.8	Schematic view of the FIR responses in the Coulomb blockade region in dark conditions (a) and under FIR irradiation (b). (I) detrapping process of the localized electron in donor levels. (II) FIR-assisted single-electron tunneling between the donor levels. These processes provide the modification of the polarization field as shown in the bottom plains. Reproduced from the Ref. [68]. ©2019 The authors. Distributed under a Creative Commons Attribution 4.0 International license (CC BY 4.0). . . . .	64
4.9	Optical and SEM images of non-LSA-integrated QD. Reproduced from the Ref. [68]. ©2019 The authors. Distributed under a Creative Commons Attribution 4.0 International license (CC BY 4.0). . . . .	68
4.10	Comparison of the responsivities of the coupled/non-coupled QD with the LSA. . . . .	69
4.11	SEM images of the connected bow-tie antenna. . . . .	70
4.12	(a,b) NF phase images (a) and line profile (b) for connected bow-tie antenna (shown in Fig. 4.11). . . . .	71
5.1	The concept of this part. (a) Comparison of the feature for investigating the vectorial nature of the NFs. (b) Illustration of the concept for clarifying the vectorial nature of the NFs. . . . .	75
5.2	Hierarchical structures formed in banded PHB spherulites. . . . .	76
5.3	(a)FF spectrum of the PHB spherulite. (b)Bonding assignment of the PHB spherulite in the IR region. Reprinted table with permission from Ref. [11]. Copyright 2013, American Chemical Society. . . . .	78
5.5	Visible light images of the non-banded PHB spherulite used in this work. (a) Unpolarized-optical image of the whole region. (b) Closed image in the center. (c) Polarised-optical microscopy image, where the polarization of irradiation is indicated by a black arrow. . . . .	80



5.6	Monochromatic NF IR measurements. (a) Schematic diagram of the s-SNOM measurements. (b) Topography of the banded PHB spherulite. (c) NF absorbance images at the C-C backbone stretch mode at $981\text{ cm}^{-1}$ , $\nu(\text{C-O})$ mode at $1054\text{ cm}^{-1}$ , and off-resonance at $945\text{ cm}^{-1}$ . The black arrow indicates the polarisation of the IR irradiation. These images were taken at $128 \times 128$ pixels. (d) Comparison of topography and NF images extracted from the region marked by the yellow dotted box in (b). (e) The line profiles shown below were taken from the yellow dotted arrows in (d), where solid lines are sinusoidal fitting results. (f) polar plot of $\overline{a_2(\nu)}$ . . . . .	82
5.7	(a)Topography of the non-banded PHB spherulite. (b) NF absorbance image of the non-banded PHB spherulite at $981\text{ cm}^{-1}$ . . . . .	83
5.8	Far-field IR images. (a,b) Maps of $A_t(\nu)$ recorded while exciting the C-C backbone stretch mode at $981\text{ cm}^{-1}$ (a) and $\nu(\text{C-O})$ mode at $1054\text{ cm}^{-1}$ (b). (c) Polar plot of $\theta$ dependence of $\overline{A_t(\nu)}$ . (d) $r$ dependence of $A_t(\nu)$ at $\theta = 45^\circ$ , which is extracted by the line profile of the yellow dashed arrow described in the inset image. The red trace guides your eyes. . . . .	84
5.9	Mesoscale NF IR images of the banded PHB spherulite (corresponding to the scale of (III) in Fig. 5.2). (a) NF IR images at the region indicated by the red star in Fig. 3(d). The acquired pixels are $64 \times 64$ pixels. (b) The line profiles were extracted from the black arrow with a 5-pixel thickness in (a). The solid trace serves as a guide. . . . .	85
5.10	SEM images of the selectively-etched banded PHB spherulite. . . . .	86
6.1	Illustration of the objective in this chapter. . . . .	88
6.2	Simulation model for three-dimensional FEM simulations. . . . .	90
6.3	(a) Illustration of the measurement for the polarization dependence of the scattering coefficient. (b) $s_3$ versus $\theta_{\text{in}}$ . . . . .	91
6.4	FEM results of the electromagnetic field distribution around a tip and its dependence on the polarisation of the irradiated light under IR irradiation at $1075\text{ cm}^{-1}$ . The white arrows indicate the direction of the vector field, revealing the existence of $z$ -polarised NF on the tip apex. . . . .	92
6.5	(a) Illustration of the measurement for the polarization dependence of the scattered light. (b) Polarization-resolved measurements of scattered light at $\theta_{\text{in}} = 0$ and $90\text{ deg.}$ . . . . .	92
6.6	(a) Illustration of the measurement for the polarization dependence of the scattered light. (b) Polarization-resolved measurements of scattered light at $\theta_{\text{in}} = 0$ and $90\text{ deg.}$ . . . . .	94
6.7	Topography of an Au disk for in-plane visualization. . . . .	95

6.8	(a) Illustration of the measurement for the polarization dependence of the scattered light. (b) Polarization-resolved measurements of scattered light at $\theta_{\text{in}} = 0$ and 90 deg. . . . .	95
6.9	(a) Illustration of the measurement for the polarization dependence of the scattered light. (b) Polarization-resolved measurements of scattered light at $\theta_{\text{in}} = 0$ and 90 deg. . . . .	96
6.10	Illustration of the nanofocusing using tapered transmission lines. Reprinted figures with permission from Ref. [94]. Copyright 2011 by Springer Nature.	97
6.11	The SEM images of the FIB-patterned AFM tip for plasmonic nanofocusing.	97
6.12	(a) Geometry of tapered transmission lines. (b) FEM simulation results for the FIB-patterned AFM tip. Inset; enclose image of the apex. . . . .	98
6.13	(a) Illustration of the measurement for the polarization dependence of the scattered light. (b) Polarization-resolved measurements of scattered light at $\theta_{\text{in}} = 0$ and 90 deg. . . . .	98
7.1	Illustration of the SPhP and expected results for $s_n^{\text{out}}$ and $s_n^{\text{in}}$ . . . . .	104
7.2	Schematic of a tilting AFM tip. . . . .	104
7.3	(a) Experimental setup for NF optoelectronic measurements. (b) Arrayed donor implanted in a Si substrate. Reprinted figures with permission from Ref. [97]. Copyright 2005 by Springer Nature. . . . .	106
7.4	Expected results. (a) Schematic of detrapping processes by the NF. (b) NF absorbance image. (c) Nanoscale spatially-resolved photocurrents image. .	106

# List of Tables

1.1	Comparison of an a-SNOM and an s-SNOM. . . . .	19
2.1	Wavelength and power of the tunable CO <sub>2</sub> gas laser. . . . .	27
2.2	Noise value of the topographic and NF signal . . . . .	30
2.3	The hardware condition for the FEM calculation. . . . .	34
2.4	The mesh condition for the FEM calculation. . . . .	36
3.1	The parameter value of the designed LSA (arm-terminated). . . . .	47
3.2	The parameter value of the non-arm terminated LSA. . . . .	47
4.1	frequency of FIR modulator versus gas. The wavenumber described in bold font is used in this experiment. . . . .	61
5.1	Comparison of the period of the twisted structure $T_{\text{vis,NF,FF}}(\nu)$ and spatial phase $\beta_{\text{NF}}(\nu) - \beta_{\text{topo}}$ . . . . .	81
6.1	The mesh condition for the FEM calculation. . . . .	89
6.2	The summary of the optical setup (Fig. 6.6). . . . .	93

# References

- <sup>1</sup>B. Shen, V. Linko, K. Tapio, S. Pikker, T. Lemma, A. Gopinath, K. V. Gothelf, M. A. Kostiainen, and J. J. Toppari, “Plasmonic nanostructures through dna-assisted lithography”, *Science advances* **4**, eaap8978 (2018).
- <sup>2</sup>Y. Mushiake, “Self-complementary antennas”, *IEEE Antennas and Propagation Magazine* **34**, 23–29 (1992).
- <sup>3</sup>N. I. Zheludev and Y. S. Kivshar, “From metamaterials to metadevices”, *Nature materials* **11**, 917–924 (2012).
- <sup>4</sup>N. Engheta and R. W. Ziolkowski, Metamaterials: physics and engineering explorations (John Wiley & Sons, 2006).
- <sup>5</sup>D. R. Smith, J. B. Pendry, and M. C. Wiltshire, “Metamaterials and negative refractive index”, *science* **305**, 788–792 (2004).
- <sup>6</sup>V. M. Shalaev, “Optical negative-index metamaterials”, *Nature photonics* **1**, 41–48 (2007).
- <sup>7</sup>J. D. Joannopoulos, P. R. Villeneuve, and S. Fan, “Photonic crystals: putting a new twist on light”, *Nature* **386**, 143–149 (1997).
- <sup>8</sup>T. Ando, Y. Matsumoto, and Y. Uemura, “Theory of hall effect in a two-dimensional electron system”, *Journal of the Physical Society of Japan* **39**, 279–288 (1975).
- <sup>9</sup>K. v. Klitzing, G. Dorda, and M. Pepper, “New method for high-accuracy determination of the fine-structure constant based on quantized hall resistance”, *Physical Review Letters* **45**, 494 (1980).
- <sup>10</sup>K. Takata and M. Notomi, “Photonic topological insulating phase induced solely by gain and loss”, *Physical review letters* **121**, 213902 (2018).
- <sup>11</sup>Y. Hikima, J. Morikawa, and T. Hashimoto, “Wavenumber dependence of ft-ir image of molecular orientation in banded spherulites of poly (3-hydroxybutyrate) and poly (l-lactic acid)”, *Macromolecules* **46**, 1582–1590 (2013).
- <sup>12</sup>P. W. Anderson, “Absence of diffusion in certain random lattices”, *Physical review* **109**, 1492 (1958).

- <sup>13</sup>T. Schwartz, G. Bartal, S. Fishman, and M. Segev, “Transport and anderson localization in disordered two-dimensional photonic lattices”, *Nature* **446**, 52–55 (2007).
- <sup>14</sup>M. Sakai, Y. Inose, K. Ema, T. Ohtsuki, H. Sekiguchi, A. Kikuchi, and K. Kishino, “Random laser action in gan nanocolumns”, *Applied Physics Letters* **97**, 151109 (2010).
- <sup>15</sup>S. H. Choi, S.-W. Kim, Z. Ku, M. A. Visbal-Onufrak, S.-R. Kim, K.-H. Choi, H. Ko, W. Choi, A. M. Urbas, T.-W. Goo, et al., “Anderson light localization in biological nanostructures of native silk”, *Nature communications* **9**, 1–14 (2018).
- <sup>16</sup>B. H. Stuart, *Infrared spectroscopy: fundamentals and applications* (John Wiley & Sons, 2004).
- <sup>17</sup>M. Tonouchi, “Cutting-edge terahertz technology”, *Nature photonics* **1**, 97–105 (2007).
- <sup>18</sup>Y. Kawano, T. Uchida, and K. Ishibashi, “Terahertz sensing with a carbon nanotube/two-dimensional electron gas hybrid transistor”, *Applied Physics Letters* **95**, 083123 (2009).
- <sup>19</sup>Y. Kawano, “Terahertz waves: a tool for condensed matter, the life sciences and astronomy”, *Contemporary Physics* **54**, 143–165 (2013).
- <sup>20</sup>M. Tabe, D. Moraru, M. Ligowski, M. Anwar, R. Jablonski, Y. Ono, and T. Mizuno, “Single-electron transport through single dopants in a dopant-rich environment”, *Physical review letters* **105**, 016803 (2010).
- <sup>21</sup>M. Tabe, A. Udhiarto, D. Moraru, and T. Mizuno, “Single-photon detection by si single-electron fets”, *physica status solidi (a)* **208**, 646–651 (2011).
- <sup>22</sup>L. Ozyuzer, A. E. Koshelev, C. Kurter, N. Gopalsami, Q. Li, M. Tachiki, K. Kadowaki, T. Yamamoto, H. Minami, H. Yamaguchi, et al., “Emission of coherent thz radiation from superconductors”, *Science* **318**, 1291–1293 (2007).
- <sup>23</sup>Y. Kawano, T. Fuse, S. Toyokawa, T. Uchida, and K. Ishibashi, “Terahertz photon-assisted tunneling in carbon nanotube quantum dots”, *Journal of Applied Physics* **103**, 034307 (2008).
- <sup>24</sup>K. Shibata, A. Umeno, K. Cha, and K. Hirakawa, “Photon-assisted tunneling through self-assembled inas quantum dots in the terahertz frequency range”, *Physical Review Letters* **109**, 077401 (2012).
- <sup>25</sup>Y. Kawano, “Wide-band frequency-tunable terahertz and infrared detection with graphene”, *Nanotechnology* **24**, 214004 (2013).
- <sup>26</sup>F. Wendler and E. Malic, “Towards a tunable graphene-based landau level laser in the terahertz regime”, *Scientific Reports* **5**, 12646 (2015).
- <sup>27</sup>W. Zhang, P. Maldonado, Z. Jin, T. S. Seifert, J. Arabski, G. Schmerber, E. Beaurepaire, M. Bonn, T. Kampfrath, P. M. Oppeneer, et al., “Ultrafast terahertz magnetometry”, *Nature communications* **11**, 1–9 (2020).

- <sup>28</sup>D. Suzuki, S. Oda, and Y. Kawano, “A flexible and wearable terahertz scanner”, *Nature Photonics* **10**, 809–813 (2016).
- <sup>29</sup>M. Ono, M. Hata, M. Tsunekawa, K. Nozaki, H. Sumikura, H. Chiba, and M. Notomi, “Ultrafast and energy-efficient all-optical switching with graphene-loaded deep-subwavelength plasmonic waveguides”, *Nature Photonics* **14**, 37–43 (2020).
- <sup>30</sup>T. Iguchi, T. Sugaya, and Y. Kawano, “Silicon-immersed terahertz plasmonic structures”, *Applied Physics Letters* **110**, 151105 (2017).
- <sup>31</sup>A. E. Nel, L. Mädler, D. Velegol, T. Xia, E. M. Hoek, P. Somasundaran, F. Klaessig, V. Castranova, and M. Thompson, “Understanding biophysicochemical interactions at the nano–bio interface”, *Nature materials* **8**, 543–557 (2009).
- <sup>32</sup>X. Deng, L. Li, M. Enomoto, and Y. Kawano, “Continuously frequency-tuneable plasmonic structures for terahertz bio-sensing and spectroscopy”, *Scientific reports* **9**, 1–9 (2019).
- <sup>33</sup>W. L. Barnes, A. Dereux, and T. W. Ebbesen, “Surface plasmon subwavelength optics”, *nature* **424**, 824–830 (2003).
- <sup>34</sup>T. Okamoto, T. Sugaya, N. Fujimura, K. Ishikawa, and Y. Kawano, “Near-field infrared investigations of an arm-terminated spiral structure with bow-tie probe”, *Journal of Physics Communications* **2**, 105004 (2018).
- <sup>35</sup>L. Rayleigh, “Xv. on the theory of optical images, with special reference to the microscope”, *The London, Edinburgh, and Dublin Philosophical Magazine and Journal of Science* **42**, 167–195 (1896).
- <sup>36</sup>Z. Thollar, C. Wadell, T. Matsukata, N. Yamamoto, and T. Sannomiya, “Three-dimensional multipole rotation in spherical silver nanoparticles observed by cathodoluminescence”, *ACS Photonics* **5**, 2555–2560 (2017).
- <sup>37</sup>T. Matsukata, C. Wadell, N. Matthaiakakis, N. Yamamoto, and T. Sannomiya, “Selected mode mixing and interference visualized within a single optical nanoantenna”, *ACS Photonics* **5**, 4986–4992 (2018).
- <sup>38</sup>T. Matsukata, N. Matthaiakakis, T.-a. Yano, M. Hada, T. Tanaka, N. Yamamoto, and T. Sannomiya, “Selection and visualization of degenerate magnetic and electric multipoles up to radial higher orders by cathodoluminescence”, *ACS Photonics* **6**, 2320–2326 (2019).
- <sup>39</sup>E. Betzig, J. K. Trautman, T. Harris, J. Weiner, and R. Kostelak, “Breaking the diffraction barrier: optical microscopy on a nanometric scale”, *Science* **251**, 1468–1470 (1991).

- <sup>40</sup>P. Grabiec, J. Radojewski, M. Zaborowski, K. Domanski, T. Schenkel, and I. Rangelow, “Batch fabricated scanning near field optical microscope/atomic force microscopy microprobe integrated with piezoresistive cantilever beam with highly reproducible focused ion beam micromachined aperture”, *Journal of Vacuum Science & Technology B: Microelectronics and Nanometer Structures Processing, Measurement, and Phenomena* **22**, 16–21 (2004).
- <sup>41</sup>R. Hillenbrand, B. Knoll, and F. Keilmann, “Pure optical contrast in scattering-type scanning near-field microscopy”, *Journal of microscopy* **202**, 77–83 (2001).
- <sup>42</sup>A. Lahrech, R. Bachelot, P. Gleyzes, and A. Boccard, “Infrared-reflection-mode near-field microscopy using an apertureless probe with a resolution of  $\lambda/600$ ”, *Optics letters* **21**, 1315–1317 (1996).
- <sup>43</sup>B. Knoll and F. Keilmann, “Scanning microscopy by mid-infrared near-field scattering.”, *Applied Physics A: Materials Science & Processing* **66** (1998).
- <sup>44</sup>C. Maissen, S. Chen, E. Nikulina, A. Govyadinov, and R. Hillenbrand, “Probes for ultrasensitive thz nanoscopy”, *Acs Photonics* **6**, 1279–1288 (2019).
- <sup>45</sup>J. Lee, K. T. Crampton, N. Tallarida, and V. A. Apkarian, “Visualizing vibrational normal modes of a single molecule with atomically confined light”, *Nature* **568**, 78–82 (2019).
- <sup>46</sup>H.-R. Park, Y.-M. Bahk, K. J. Ahn, Q.-H. Park, D.-S. Kim, L. Martin-Moreno, F. J. Garcia-Vidal, and J. Bravo-Abad, “Controlling terahertz radiation with nanoscale metal barriers embedded in nano slot antennas”, *Acs Nano* **5**, 8340–8345 (2011).
- <sup>47</sup>A. S. McLeod, P. Kelly, M. Goldflam, Z. Gainsforth, A. J. Westphal, G. Dominguez, M. H. Thiemens, M. M. Fogler, and D. Basov, “Model for quantitative tip-enhanced spectroscopy and the extraction of nanoscale-resolved optical constants”, *Physical Review B* **90**, 085136 (2014).
- <sup>48</sup>B. Knoll and F. Keilmann, “Near-field probing of vibrational absorption for chemical microscopy”, *Nature* **399**, 134–137 (1999).
- <sup>49</sup>B. Knoll and F. Keilmann, “Enhanced dielectric contrast in scattering-type scanning near-field optical microscopy”, *Optics communications* **182**, 321–328 (2000).
- <sup>50</sup>I. S. Averbukh, B. Chernobrod, O. Sedletsy, and Y. Prior, “Coherent near field optical microscopy”, *Optics communications* **174**, 33–41 (2000).
- <sup>51</sup>A. Cvitkovic, N. Ocelic, and R. Hillenbrand, “Analytical model for quantitative prediction of material contrasts in scattering-type near-field optical microscopy”, *Optics express* **15**, 8550–8565 (2007).

- <sup>52</sup>J. L. Bohn, D. J. Nesbitt, and A. Gallagher, “Field enhancement in apertureless near-field scanning optical microscopy”, *JOSA A* **18**, 2998–3006 (2001).
- <sup>53</sup>K. Kurihara, A. Otomo, A. Syouji, J. Takahara, K. Suzuki, and S. Yokoyama, “Superfocusing modes of surface plasmon polaritons in conical geometry based on the quasi-separation of variables approach”, *Journal of Physics A: Mathematical and Theoretical* **40**, 12479 (2007).
- <sup>54</sup>K. Zhang, S.-i. Taniguchi, and T. Tachizaki, “Generation of broadband near-field optical spots using a thin-film silicon waveguide with gradually changing thickness”, *Optics Letters* **43**, 5937–5940 (2018).
- <sup>55</sup>T. Umakoshi, Y. Saito, and P. Verma, “Highly efficient plasmonic tip design for plasmon nanofocusing in near-field optical microscopy”, *Nanoscale* **8**, 5634–5640 (2016).
- <sup>56</sup>M. J. Turner, R. W. Clough, H. C. Martin, and L. Topp, “Stiffness and deflection analysis of complex structures”, *Journal of the Aeronautical Sciences* **23**, 805–823 (1956).
- <sup>57</sup>J. E. Jones, “On the determination of molecular fields.—ii. from the equation of state of a gas”, *Proceedings of the Royal Society of London. Series A, Containing Papers of a Mathematical and Physical Character* **106**, 463–477 (1924).
- <sup>58</sup>G. Lu, R. Zhao, H. Yin, Z. Xiao, and J. Zhang, “Improved point dipole model for subwavelength resolution scattering near-field optical microscopy (snom)”, *International Journal of Antennas and Propagation* **2020** (2020).
- <sup>59</sup>I. Morichika, K. Murata, A. Sakurai, K. Ishii, and S. Ashihara, “Molecular ground-state dissociation in the condensed phase employing plasmonic field enhancement of chirped mid-infrared pulses”, *Nature communications* **10**, 1–8 (2019).
- <sup>60</sup>S. Du, K. Yoshida, Y. Zhang, I. Hamada, and K. Hirakawa, “Terahertz dynamics of electron–vibron coupling in single molecules with tunable electrostatic potential”, *Nature Photonics* **12**, 608–612 (2018).
- <sup>61</sup>Y. Zhang, K. Shibata, N. Nagai, C. Ndebeka-Bandou, G. Bastard, and K. Hirakawa, “Probing many-body quantum states in single inas quantum dots: terahertz and tunneling spectroscopy”, *Physical Review B* **91**, 241301 (2015).
- <sup>62</sup>E. Riccardi, S. Massabeau, F. Valmorra, S. Messelot, M. Rosticher, J. Tignon, K. Watanabe, T. Taniguchi, M. Delbecq, S. Dhillon, et al., “Ultra-sensitive photoresponse of graphene quantum dot in coulomb blockade regime to thz radiation”, *Nano Letters* (2020).
- <sup>63</sup>K. G. Lee, H. Kihm, J. Kihm, W. Choi, H. Kim, C. Ropers, D. Park, Y. Yoon, S. Choi, D. Woo, et al., “Vector field microscopic imaging of light”, *Nature Photonics* **1**, 53–56 (2007).



- <sup>64</sup>J. Dyson and P. Mayes, “New circular-polarized frequency-independent antennas with conical beam or omnidirectional patterns”, *IRE Transactions on Antennas and Propagation* **9**, 334–342 (1961).
- <sup>65</sup>C. A. Balanis, *Antenna theory: analysis and design* (John Wiley & Sons, 2016).
- <sup>66</sup>Y. Kawano and S. Komiyama, “Spatial distribution of nonequilibrium electrons in quantum hall devices: imaging via cyclotron emission”, *Physical Review B* **68**, 085328 (2003).
- <sup>67</sup>E. D. Palik, *Handbook of optical constants of solids*, Vol. 3 (Academic Press, 1998).
- <sup>68</sup>T. Okamoto, N. Fujimura, L. Crespi, T. Kodaera, and Y. Kawano, “Terahertz detection with an antenna-coupled highly-doped silicon quantum dot”, *Scientific reports* **9**, 1–6 (2019).
- <sup>69</sup>M. Schnell, A. Garcia-Etxarri, A. J. Huber, K. B. Crozier, A. Borisov, J. Aizpurua, and R. Hillenbrand, “Amplitude- and phase-resolved near-field mapping of infrared antenna modes by transmission-mode scattering-type near-field microscopy”, *The Journal of Physical Chemistry C* **114**, 7341–7345 (2010).
- <sup>70</sup>S. E. Grefe, D. Leiva, S. Mastel, S. D. Dhuey, S. Cabrini, P. J. Schuck, and Y. Abate, “Near-field spatial mapping of strongly interacting multiple plasmonic infrared antennas”, *Physical Chemistry Chemical Physics* **15**, 18944–18950 (2013).
- <sup>71</sup>Y. Xiang, S. Amarie, W. Cai, W. Luo, W. Wu, M. Ren, X. Zhang, and J. Xu, “Real-space mapping of mid-infrared near-field of yagi-uda antenna in the emission mode”, *Optics Express* **27**, 5884–5892 (2019).
- <sup>72</sup>S. Mastel, S. Grefe, G. Cross, A. Taber, S. Dhuey, S. Cabrini, P. Schuck, and Y. Abate, “Real-space mapping of nanoplasmonic hotspots via optical antenna-gap loading”, *Applied Physics Letters* **101**, 131102 (2012).
- <sup>73</sup>S. Usui, S. Kitade, I. Morichika, K. Kohmura, F. Kusa, and S. Ashihara, “Near-field imaging of infrared nanoantenna modes under oblique illumination”, *The Journal of Physical Chemistry C* **121**, 26000–26006 (2017).
- <sup>74</sup>A. Apuzzo, M. Février, R. Salas-Montiel, A. Bruyant, A. Chelnokov, G. Léron del, B. Dagens, and S. Blaize, “Observation of near-field dipolar interactions involved in a metal nanoparticle chain waveguide”, *Nano letters* **13**, 1000–1006 (2013).
- <sup>75</sup>Z. H. Kim and S. R. Leone, “Polarization-selective mapping of near-field intensity and phase around gold nanoparticles using apertureless near-field microscopy”, *Optics Express* **16**, 1733–1741 (2008).
- <sup>76</sup>J. Tenorio-Pearl, E. Herbschleb, S. Fleming, C. Creatore, S. Oda, W. Milne, and A. Chin, “Observation and coherent control of interface-induced electronic resonances in a field-effect transistor”, *Nature materials* **16**, 208–213 (2017).

- <sup>77</sup>Y. Taur and T. H. Ning, Fundamentals of modern vlsi devices (Cambridge university press, 2013).
- <sup>78</sup>D. Mocatta, G. Cohen, J. Schattner, O. Millo, E. Rabani, and U. Banin, “Heavily doped semiconductor nanocrystal quantum dots”, *Science* **332**, 77–81 (2011).
- <sup>79</sup>L. Creswell, D. Hasko, and D. Williams, “Microwave excitation of localized electrons in phosphorus-doped silicon single electron transistors”, *Journal of Applied Physics* **105**, 104508 (2009).
- <sup>80</sup>A. Rossi and D. Hasko, “Microwave-assisted transport via localized states in degenerately doped si single electron transistors”, *Journal of Applied Physics* **108**, 034509 (2010).
- <sup>81</sup>M. Rinzan, G. Jenkins, H. Drew, S. Shafranjuk, and P. Barbara, “Carbon nanotube quantum dots as highly sensitive terahertz-cooled spectrometers.”, *Nano letters* **12**, 3097–3100 (2012).
- <sup>82</sup>L. Kouwenhoven, S. Jauhar, J. Orenstein, P. McEuen, Y. Nagamune, J. Motohisa, and H. Sakaki, “Observation of photon-assisted tunneling through a quantum dot”, *Physical review letters* **73**, 3443 (1994).
- <sup>83</sup>L. Kouwenhoven, S. Jauhar, K. McCormick, D. Dixon, P. McEuen, Y. V. Nazarov, N. Van Der Vaart, and C. Foxon, “Photon-assisted tunneling through a quantum dot”, *Physical Review B* **50**, 2019 (1994).
- <sup>84</sup>Y. Taur, “T. h, ning, “”, *Fundamentals of Modern VLSI Devices* (1998).
- <sup>85</sup>T. Atay, J.-H. Song, and A. V. Nurmikko, “Strongly interacting plasmon nanoparticle pairs: from dipole- dipole interaction to conductively coupled regime”, *Nano letters* **4**, 1627–1631 (2004).
- <sup>86</sup>I. Romero, J. Aizpurua, G. W. Bryant, and F. J. G. De Abajo, “Plasmons in nearly touching metallic nanoparticles: singular response in the limit of touching dimers”, *Optics express* **14**, 9988–9999 (2006).
- <sup>87</sup>J. B. Lassiter, J. Aizpurua, L. I. Hernandez, D. W. Brandl, I. Romero, S. Lal, J. H. Hafner, P. Nordlander, and N. J. Halas, “Close encounters between two nanoshells”, *Nano letters* **8**, 1212–1218 (2008).
- <sup>88</sup>J. S. Trent, J. I. Scheinbeim, and P. R. Couchman, “Ruthenium tetraoxide staining of polymers for electron microscopy”, *Macromolecules* **16**, 589–598 (1983).
- <sup>89</sup>Y. Saito, N. Hayazawa, H. Kataura, T. Murakami, K. Tsukagoshi, Y. Inouye, and S. Kawata, “Polarization measurements in tip-enhanced raman spectroscopy applied to single-walled carbon nanotubes”, *Chemical Physics Letters* **410**, 136–141 (2005).

- <sup>90</sup>Y. Saito, M. Kobayashi, D. Hiraga, K. Fujita, S. Kawano, N. Smith, Y. Inouye, and S. Kawata, “Z-polarization sensitive detection in micro-raman spectroscopy by radially polarized incident light”, *Journal of Raman Spectroscopy: An International Journal for Original Work in all Aspects of Raman Spectroscopy, Including Higher Order Processes, and also Brillouin and Rayleigh Scattering* **39**, 1643–1648 (2008).
- <sup>91</sup>T. Okamoto, R. Meguya, T. Yoshida, J. Morikawa, and Y. Kawano, “Utilising the vectorial nature of near fields for optically accessing multiscale structures”, submitted to *Nature photonics* (2021).
- <sup>92</sup>J. Veerman, M. Garcia-Parajo, L. Kuipers, and N. Van Hulst, “Single molecule mapping of the optical field distribution of probes for near-field microscopy”, *Journal of microscopy* **194**, 477–482 (1999).
- <sup>93</sup>M. Burrese, R. Engelen, A. Opheij, D. van Oosten, D. Mori, T. Baba, and L. Kuipers, “Observation of polarization singularities at the nanoscale”, *Physical review letters* **102**, 033902 (2009).
- <sup>94</sup>M. Schnell, P. Alonso-Gonzalez, L. Arzubiaga, F. Casanova, L. E. Hueso, A. Chuvilin, and R. Hillenbrand, “Nanofocusing of mid-infrared energy with tapered transmission lines”, *Nature photonics* **5**, 283 (2011).
- <sup>95</sup>C. Chen, Q. Chen, J. Xu, and V. Koltun, “Learning to see in the dark”, in *Proceedings of the IEEE conference on computer vision and pattern recognition* (2018), pp. 3291–3300.
- <sup>96</sup>P. Alonso-González, A. Y. Nikitin, Y. Gao, A. Woessner, M. B. Lundeberg, A. Principi, N. Forcellini, W. Yan, S. Vélez, A. J. Huber, et al., “Acoustic terahertz graphene plasmons revealed by photocurrent nanoscopy”, *Nature nanotechnology* **12**, 31–35 (2017).
- <sup>97</sup>T. Shinada, S. Okamoto, T. Kobayashi, and I. Ohdomari, “Enhancing semiconductor device performance using ordered dopant arrays”, *Nature* **437**, 1128–1131 (2005).